UNIVERSITÀ DEGLI STUDI DI PADOVA

Sede Amministrativa: Università degli Studi di Padova

Dipartimento di Astronomia

SCUOLA DI DOTTORATO DI RICERCA IN ASTRONOMIA
CICLO XXI

ASTRONOMICAL APPLICATIONS OF OPTICAL VORTICES

Direttore della Scuola: Prof. Giampaolo Piotto
Supervisori: Prof. Antonio Bianchini
Dr. Fabrizio Tamburini

Dottorando: Gabriele Anzolin

DATA CONSEGNA TESI
31 gennaio 2009

Acknowledgments

There are many people who helped me during this research experience. Firstly, I would like to thank my supervisors Prof. Antonio Bianchini and Dr. Fabrizio Tamburini for giving me the possibility to carry out an investigation in a non-conventional field of astronomy and for hosting me in their office during these three years. I will never forget the innumerable discussions we had about physics, politics and many other (less serious) things.

I am also grateful to the external advisor Prof. Bo Thidé (IRFU, Uppsala, Sweeden) for his invaluable contribution in promoting and improving this work, in particular during his visit in Padova.

I would like to thank also Prof. Cesare Barbieri (University of Padova), Gabriele Umbriaco (University of Padova), Elettra Mari (University of Padova), Prof. Sergio Ortolani (University of Padova), Dr. Enrico Giro (Astronomical Observatory of Padova), Dr. Claudio Pernechele (Astronomical Observatory of Padova), Prof. Filippo Romanato (University of Padova) and the director of the Department of Astronomy Prof. Piero Rafanelli (University of Padova) for their help and support.

Part of the experiments presented in this Thesis were carried out using fork holograms kindly provided by the Zeilinger-Gruppe at the Institut für Experimentalphysik (University of Vienna, Austria). For this reason, I am grateful to all the members of the group and, especially, to Dr. Thomas Jennewein.

Special thanks go to Dr. Domitilla de Martino (Astronomical Observatory of Capodimonte, Napoli) and Dr. Marina Orio (Astronomical Observatory of Padova) for giving me the possibility to start a parallel research in the field of high-energy astrophysics. I am very grateful also for the financial support that they provided to me during the last two years.

My grateful acknowledgments go also to Dr. Gabriel Molina-Terriza, Prof. Juan P. Torres and Prof. Morgan Mitchell for hosting me at ICFO (Barcelona, Spain).

I am grateful to all the guys (Gabriele, Cesare, Federico, Antonino, Yuri, Claudio, Rodolfo and many others) with whom I shared unforgettable moments in Padova starting from the very beginning of my undergraduate studies.

I would like to thank my family, in particular my father who had a decisive role in convincing me to accept the PhD position at the Department of Astronomy in spite of my initial perplexity.

Finally, I am very grateful to Marta, whose presence by my side throughout these last years has been of fundamental importance.

The research work presented in this thesis has been partially supported by the University of Padova, by the Ministry of University and Research and by the CARIPARO Foundation inside the 2006 Program of Excellence.

Abstract

Optical vortices represent a particular class of wavefront dislocations characterized by a topological charge ℓ. The surface of constant phase of an electromagnetic wave carrying an optical vortex has a helical structure and presents a singularity along the axis of the helicoid, where the phase is undefined. As a consequence, the intensity distribution of a vortex light beam contains a central dark region, where the intensity is zero due to destructive interference. Optical vortices can be produced by using phase modifying devices, i.e. particular optical elements possessing an optical singularity generally located at their center. The most efficient of them are fork holograms and spiral phase plates.

In the last decade, the properties of optical vortices have found interesting applications in optical physics. Among these, the most promising are those in optical communications, nanotechnologies and biology. Optical vortices are attracting increasing attention also in astronomy, where the properties of such features of the electromagnetic radiation could provide a new approach to the study of astrophysical phenomena.

The purpose of this Thesis is to present some possible applications of optical vortices to instrumental astronomy. In particular, this work is focused on the development and testing of new techniques to improve the performances of optical systems. Firstly, a method is proposed to improve the resolving power of a diffraction-limited telescope by means of an $\ell = 1$ fork hologram. Both the experiments and numerical simulations reveal that the superposition of the optical vortices produced by two light beams characterized by equal Airy intensity distributions present a detectable asymmetry even for separations that are one order of magnitude below the limit of the Rayleigh criterion. It is shown that this result can be achieved both with monochromatic and white light beams.

We then present the first astronomical experiment in which we produced optical vortices in starlight beams with an $\ell = 1$ FH placed at the focal plane of the Galileo 122 cm telescope in Asiago. By using the Lucky Imaging approach to reduce the effects of mediocre seeing conditions, we were able to observe the images of the optical vortices produced by the two main components of the multiple system α Her, in non-monochromatic light, and by the single star α Boo, using a narrow bandpass. In both cases, the intensity profiles of the observed optical vortices are in agreement with numerical simulations.

Detailed analytical models and numerical simulations confirm that the spatial structure of an optical vortex produced by a phase modifying device is extremely sensitive to off-axis displacements of the input beam, especially when high values of the topological charge ℓ are used. This property could be used to perform ground-based astrometric measurements with a precision competitive to standard PSF-fitting astrometry. The sensitivity to small off-axis displacements might also help to improve the tip/tilt correction of the wavefront for a small field of view.

We discuss also the possible application of the nulling property of even-charged optical vortices to perform high-contrast coronagraphy. In this case, the nulling of the light of an on-axis star is achieved by using a spiral phase plate and a circular diaphragm as Lyot stop. In principle, this coronagraphic design is one of the very few that might allow direct imaging of extrasolar terrestrial planets. However, such remarkable performance is still strongly limited by the current techniques used to manufacture spiral phase plates. In the framework of projecting an $\ell = 2$ optical vortex coronagraph for visible wavelengths, we present the results of numerical simulations obtained considering a spiral phase plate with a surface subdivided in N discrete levels. A description of the experimental procedures used to test spiral phase plates manufactured with PMMA (polymethyl methacrylate) material is also given.

Sommario

I vortici ottici rappresentano una particolare classe di dislocazioni dei fronti d'onda caratterizzate da una carica topologica ℓ. La superficie di fase costante di un'onda elettromagnetica che trasporta un vortice ottico ha una struttura elicoidale. Lungo l'asse di questa elica è presente una singolarità in cui la fase non può essere definita. Di conseguenza, la distribuzione d'intensità di un fascio di luce contenente un vortice ottico presenta una zona centrale dove l'intensità è nulla per effetto dell'interferenza distruttiva. I vortici ottici possono essere prodotti utilizzando particolari elementi ottici detti *phase modifying devices* che modificano la fase di un'onda incidente. I più efficienti tra questi sono i *fork holograms* (ologrammi) e le *spiral phase plates* (maschere di fase).

Negli ultimi anni, le proprietà dei vortici ottici hanno trovato interessanti applicazioni nei campi della fisica e dell'ottica. Tra queste, le più promettenti sono quelle in comunicazioni ottiche, nelle nanotecnologie ed in biologia. Recentemente, i vortici ottici stanno suscitando un crescente interesse anche nella cumunità astronomica. Infatti, queste particolari proprietà della radiazione elettromagnetica potrebbero permettere di studiare diversi fenomeni astrofisici da un punto di vista completamente nuovo.

In questa Tesi vengono presentate alcune possibili applicazioni dei vortici ottici in strumentazione astronomica. In particolare, lo scopo principale di questo lavoro è lo sviluppo di nuove tecniche che permetteranno di migliorare le prestazioni di sistemi ottici. In primo luogo, viene proposto un metodo per aumentare il potere risolutivo di un telescopio limitato dalla diffrazione che prevede l'utilizzo di un *fork hologram* con una singola dislocazione. I risultati di esperimenti e simulazioni numeriche rivelano che la sovrapposizione dei vortici ottici prodotti da

due fasci di luce con una distribuzione d'intensità di Airy mostra già un'evidente asimmetria quando la separazione è di un ordine di grandezza inferiore rispetto al limite posto dal criterio di Rayleigh. Questo risultato è stato ottenuto sia in luce monocromatica, sia in luce bianca.

Viene poi presentato il primo esperimento astronomico in cui sono stati prodotti vortici ottici con un *fork hologram* avente una singola dislocazione posto al piano focale del telescopio Galileo da 122 cm di Asiago. Utilizzando i principi del *Lucky Imaging* per ridurre gli effetti provocati da condizioni di seeing mediocre, sono state osservate le immagini dei vortici ottici prodotti dalle due componenti principali del sistema multiplo α Her, in luce non monocromatica, e dalla stella singola α Boo, utilizzando un filtro spaziale a banda stretta. In entrambi i casi, i profili d'intensità dei vortici ottici osservati sono riproducibili con simulazioni numeriche.

La sensibilità dell'immagine di un vortice ottico prodotto con un *phase modifying device* rispetto a spostamenti fuori asse del fascio entrante è confermata da modelli analitici dettagliati e anche da simulazioni numeriche, specialmente nel caso in cui vengano utilizzati elevati valori della cariche topologica ℓ. Questa proprietà potrebbe essere utilizzata per fare misure astrometriche da terra con una precisione che potrebbe competere con quella fornita dalle tecniche standard di astrometria di PSF. La sensibilità rispetto a piccoli spostamenti fuori asse potrebbe anche essere sfruttata per migliorare la correzione dell'aberrazione di tip/tilt del fronte d'onda in un piccolo campo di vista.

Viene poi discussa la possibile applicazione di vortici ottici con carica topologica pari nella coronografia ad alto contrasto. In questo caso, l'azione combinata di una *spiral phase plate* e di un diaframma circolare utilizzato come stop di Lyot permette di annullare totalmente la luce di una stella in asse. Studi teorici indicano che il coronografo a vortici ottici è uno dei pochi che potrebbe realmente permettere l'osservazione diretta di pianeti extrasolari di tipo terrestre. Purtroppo, questa notevole proprietà è fortemente limitata dalle attuali tecniche usate per produrre le *spiral phase plate*. Nell'ambito di un progetto di costruzione di un coronografo a vortici ottici con $\ell = 2$ ottimizzato per lunghezze d'onda visibili, vengono presentati i risultati di simulazioni numeriche ottenuti considerando una *spiral phase plate* la cui superficie è suddivisa in N livelli discreti. Infine, vengono discusse le procedure sperimentali utilizzate per testare *spiral phase plates* in PMMA (polimetil-metacrilato).

Contents

List of Figures

List of Tables

Chapter 1

Introduction to optical vortices

1.1 Wavefront dislocations

In the early Seventies, attempts made in order to better understand the echoes of radio pulses sent towards the ice cap in Antarctica led to the discovery of peculiar features present in the phase fronts of those radio signals. Nye and Berry [1] called these phase defects *wavefront dislocations*, thanks to the similarity to those found within a crystal structure (see e.g. [2]). The concept of a wavefront dislocation was then readily recognized as a general property of a wave field.

Wavefront dislocations are mathematical singularities that appear in the phase term $\Phi(\vec{r},t)$ of any physical field represented by a wave function of the kind

$$\psi(\vec{r},t) = A(\vec{r},t)\exp\left[\mathrm{i}\,\Phi(\vec{r},t)\right] \ . \tag{1.1}$$

The amplitude term $A(\vec{r},t)$ has to be zero in correspondence of the position of a wavefront dislocation, where the phase is not defined [3]. This condition is required in order to avoid physical inconsistencies related to the presence of the singularities and can be interpreted as the result of destructive interference occurring at any singular point. According to the terminology used to describe dislocations in crystal lattices, wavefront dislocations are subdivided in three main classes:

1. edge dislocation;

2. screw dislocations;

3. mixed screw-edge dislocation.

An edge dislocation produces a constant shift of a section of the wavefront, so that the phase is undefined along a line lying on a plane perpendicular to the direction of propagation. For example, the dark rings of an Airy pattern produced by the diffraction of a plane wave beyond a circular aperture are produced by closed edge dislocations [4]. Screw dislocations, instead, are point phase defects, while the latter type of dislocations are, as the name suggests, mixtures of screw and edge dislocations.

In this Thesis, I will discuss the properties and applications of screw dislocations, which are now better known with the name *optical vortices* (OVs). This terminology was firstly introduced by Coullet *et al.* [5] to classify laser modes represented by spiral waves rotating around the points where the amplitude of the electric field is zero. More generally, electromagnetic (EM) waves harboring OVs can be obtained as particular solutions of the scalar wave equation in vacuum

$$\Box\psi = 0 \, , \tag{1.2}$$

where the D'Alambert operator acting on the wave function ψ is defined as $\Box = \nabla^2 - (1/c^2)(\partial^2/\partial t^2)$. In the following, we will neglect the dependence on time of ψ as we are interested only in its spatial dependence [1]. It is also convenient to use a cylindrical coordinate system (r, θ, z), where z is the propagation axis of the wave field. In this way, the simplest expressions of the complex field of a steady singular wave containing an OV along the z axis are [6]:

$$\psi(r,\theta,z) \propto \begin{cases} r^{|\ell|} \exp\left[\mathrm{i}(\ell\,\theta + k z)\right] \\ r^{-|\ell|} \exp\left[\mathrm{i}(\ell\,\theta + k z)\right] \end{cases} , \tag{1.3}$$

where $k = 2\pi/\lambda$ is the wave vector and λ is wavelength. One can readily recognize the presence of a peculiar phase term $\exp(\mathrm{i}\ell\,\theta)$ which depends on the azimuthal angle θ multiplied by a signed integer number ℓ called *topological charge*. This term is present in the phase of any optical wave containing an OV.

---

[1] This is equivalent to solve the wave equation using the method of separation of variables.

A screw wavefront dislocation is characterized by its own topological charge $\ell \in \mathbb{Z}$ defined as the path integral of the scalar product between the phase gradient $\nabla\Phi$ and the length element vector $\mathrm{d}\vec{l}$:

$$\ell = \frac{1}{2\pi} \oint \nabla\Phi \cdot \mathrm{d}\vec{l} \,. \tag{1.4}$$

The integration is performed along a circuit enclosing the singular point. The topological charge, which is rather a geometrical than a physical characteristic of an OV, indicates the number of 2π phase changes encountered along any closed circuit around the dislocation center.

The surfaces of constant phase of both the wave functions expressed in Eqs. 1.3 are defined by

$$\ell\,\theta + kz = \mathrm{const}\,. \tag{1.5}$$

This equation describes a planar surface if $\ell = 0$, or a helical surface with a pitch angle $\ell\lambda$ if $\ell \neq 0$. In the case $|\ell| > 1$, the wavefront is composed by a number $|\ell|$ of coaxial helicoids separated by a distance equal to the wavelength λ along the z axis. Fig. 1.1 shows some examples of wavefronts of waves containing OVs with different topological charges. As a convention, the helical wavefront is right-handed if the sign of the topological charge is positive, while it is left-handed in the opposite case. The helicity of the vortex is independent of the choice of the coordinate systems [4], as well as of the path used to evaluate the integral in Eq. 1.4.

As a matter of fact, the first of Eqs. 1.3 diverges for $r \to \infty$, while the other one diverges close to the z axis. Therefore, these solutions of the scalar wave equation cannot describe physical wave fields. The unwanted behavior must be then fixed by introducing an additional amplitude term which balances the divergences. For this reason, the general form of an EM carrying an ℓ-charged OV along the z axis takes the form:

$$\psi(r,\theta,z) = A_\ell(r,z)\exp\left[\mathrm{i}\,\Phi_\ell(r,z)\right]\exp(\mathrm{i}\ell\,\theta)\ . \tag{1.6}$$

Here, the amplitude A_ℓ is a real function, possibly depending on ℓ which vanishes both at $r = 0$, where the phase singularity is located, and large radii ($r \to \infty$). The phase term in Eq. 1.6 has been purposely subdivided in two parts, in order to

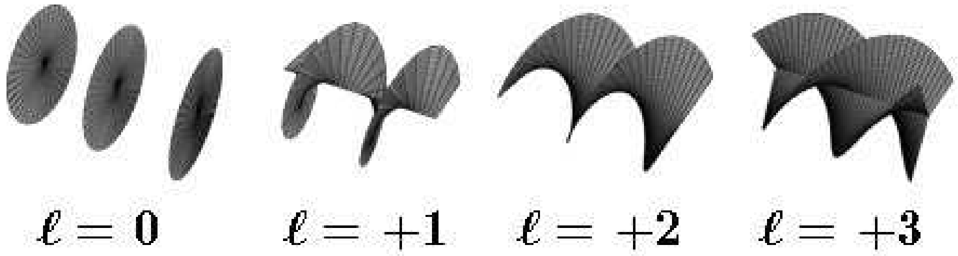

Figure 1.1 – Surfaces of constant phase (wavefronts) of waves containing screw dislocations with $\ell = 0, 1, 2, 3$. Figure adapted from `http://www.physics.gla.ac.uk/Optics/play/photonOAM/`.

separate the vortex term which depends on the azimuthal angle θ from the term Φ_ℓ which depends only on the r and z coordinates. Both the amplitude A_ℓ and the phase term Φ_ℓ may vary while the wave propagates, since they are dependent on the z coordinate. However, the OV remains embedded in the wave field and its position can be always found by solving simultaneously the equations $\Re(\psi) = 0$ and $\Im(\psi) = 0$.

It was also shown theoretically and experimentally, that OVs behaves similarly to charged particles. Optical screw dislocations having topological charges with the same sign may repel each other, whereas those with opposite charges may attract themselves and annihilate in consequence of a collision. OVs having charge ±1 are find to be robust with respect to external perturbations. For example, a single-charged OV can self-reconstructs itself beyond an opaque screen which obstructs part of the host wave [7]. Instead, OVs with topological charges different from unity tend to split into single-charged ones, with conservation of the total net charge [8]. The reflection of a wave carrying a screw dislocation implies the inversion of the sign of the topological charge [9].

1.2 The orbital angular momentum of light

In 1992 Allen *et al.* [10] showed that light beams containing screw dislocations carry also a quantity of orbital angular momentum (OAM). This property is related to the helicoidal shape of the wavefront, which causes the Poynting vector to precess around the direction of propagation [11]. As a result, the Poynting vector associated to this kind of beams possesses an azimuthal component. Laguerre-Gaussian (L-G) modes, a particular class of cylindrically symmetric laser cavity modes, represent the prototype of light beams carrying OAM. For this reason, they have been extensively used in singular optics. A generic L-G mode is characterized by two integer indices: the azimuthal index ℓ, that coincides with the topological charge of the hosted OV, and the radial index p, that defines the number of radial nodes of the mode. The mathematical expression of the field of a generic L-G mode propagating along the z axis is

$$\begin{aligned} u_{p\ell}(r,\theta,z) = {} & \sqrt{\frac{2p!}{\pi(p+|\ell|)!}}\,\frac{1}{w(z)}\left(\frac{r\sqrt{2}}{w(z)}\right)^{|\ell|} \mathrm{L}_p^{|\ell|}\left(\frac{2r^2}{w^2(z)}\right)\exp\left(-\frac{r^2}{w^2(z)}\right) \\ & \times \exp\left(-\frac{\mathrm{i}kr^2}{2R(z)}\right)\exp[-\mathrm{i}(2p+|\ell|+1)\phi(z)]\,\exp(\mathrm{i}\ell\,\theta)\,, \end{aligned} \tag{1.7}$$

where $w^2(z) = (z_R^2 + z^2)/(kz_R)$ is the beam width (the radius at which the amplitude decreases by a factor e^{-1}), z_R is the Rayleigh range, $R(z) = (z_R^2 + z^2)/z$ is the curvature radius, $\phi(z) = \arctan(z/z_R)$ is the Gouy phase and $\mathrm{L}_p^{|\ell|}$ is a generalized Laguerre polynomial [12]. The fact that an L-G beam carries a quantity of OAM has been firstly proved within the paraxial approximation [2]. However, this property was subsequently generalized also in the non-paraxial regime [13].

The EM field of a generic vortex beam can be obtained from a vector potential of the kind

$$\vec{A}(\vec{r},t) = \vec{\sigma}u(\vec{r})\mathrm{e}^{\mathrm{i}(kz-\omega t)}\,, \tag{1.8}$$

where $\vec{\sigma}$ is a complex vector describing the polarization of the field, ω is the frequency and $u(\vec{r})$ is a complex function that contains the vortex phase term:

$$u(r,\theta) = u(r)\exp(\mathrm{i}\ell\,\theta)\,. \tag{1.9}$$

For beams of this kind, the time-averaged linear momentum density [14] is given by [10]

$$\langle\vec{\mathscr{P}}\rangle = \mathrm{i}\omega\frac{\varepsilon_0}{2}\left(u^*\nabla u - u\nabla u^*\right) + \omega k\varepsilon_0|u|^2\hat{z} + \omega\sigma\frac{\varepsilon_0}{2}\frac{\partial\,|u|^2}{\partial r}\hat{\theta}\,. \tag{1.10}$$

---

[2] For an EM field u, the paraxial approximation is achieved by neglecting $\partial^2u/\partial z^2$ compared with $k(\partial u/\partial z)$ and ignoring $|\partial u/\partial z|$ compared with u in the scalar wave equation 1.2. In other words, it is assumed that the wave vector k subtends a small angle with respect to the optical axis.

Here, a cylindrical coordinates system with unit vectors $\hat{r}$, $\hat{z}$ and $\hat{\theta}$ is used. By inserting the expression of $u(\vec{r})$ (Eq. 1.9) into Eq. 1.10, one can obtain the components of the linear momentum density [15]:

$$\begin{aligned}
\mathscr{P}_r &= \varepsilon_0 \frac{\omega k r}{R(z)} |u|^2 \,, && (1.11)\\
\mathscr{P}_z &= \varepsilon_0 \omega k |u|^2 \,, && (1.12)\\
\mathscr{P}_\theta &= \varepsilon_0 \left[\frac{\omega \ell}{r} |u|^2 - \frac{1}{2} \omega \sigma \frac{\partial |u|^2}{\partial r} \right] . && (1.13)
\end{aligned}$$

The transverse component $\mathscr{P}_\theta$ is constituted by two separate terms: one depending only on σ and one depending only on ℓ. The latter is responsible for the transport of OAM. In fact, the total angular momentum density $\vec{\mathscr{J}}$ can be obtained from the evaluation of the cross product between the radius vector $\vec{r}$ and $\vec{\mathscr{P}} = (\mathscr{P}_r, \mathscr{P}_z, \mathscr{P}_\theta)$ [14]:

$$\vec{\mathscr{J}} = \vec{r} \times \vec{\mathscr{P}} \,. \tag{1.14}$$

The z component of the total angular momentum density is thus:

$$\mathscr{J}_z = \varepsilon_0 \left(\omega \ell |u|^2 + \frac{1}{2} \omega \sigma r \frac{\partial |u|^2}{\partial r} \right) . \tag{1.15}$$

The integration of $\mathscr{J}_z$ over the whole cross-section of the beam gives the quantity of total angular momentum per unit length carried by the beam. If the EM field carries an energy W, then the total angular momentum per energy unit is

$$\frac{J_z}{W} = \frac{\ell}{\omega} + \frac{\sigma}{\omega} \,. \tag{1.16}$$

We see that J_z can be decomposed in two separated terms: the OAM, which depends on ℓ, and the spin, which depends on σ. Therefore, a vortex beam with an energy $W = \hbar\omega$ carries a quantity $\ell\hbar$ of OAM per photon [10, 16].

The question of whether OAM is an intrinsic property of photons [3] was debated for a long time [17, 18, 19]. However, the covariant formulation of the photon wave function has been shown to be formally equivalent to quantum electrodynamics. This implies that OAM is not an intrinsic property of single photons, otherwise the correspondent Dirac-like equation would admit an infinite spectrum of intrinsic angular momentum (spin) states [20, 21].

---

[3] The intrinsic properties of a particle are those that do not depend on the choice of the reference frame, like the rest mass, the electric charge and the spin.

1.3 Optical vortices in nature

The spontaneous appearance of OVs was firstly postulated and, then, demonstrated in beams propagating through irregular refracting media or reflected from rough surfaces [1, 22]. OVs were also recognized in the phase fronts of light beams propagating through nonlinear media like high-density vapors [23] or Kerr refractive media [24], as well as in nonlinear optical system [25, 26]. As a consequence, optical speckle fields have been shown to contain a large number of randomly distributed OVs [27, 28]. The appearance of screw wavefront dislocations has been demonstrated also in the simple case of three (or more) interfering plane waves [29].

OVs are known to appear spontaneously in EM waves generated in resonator cavities [30, 31, 32], Fabry-Perot resonator [33] and photorefractive oscillator [34]. In fact, EM fields containing screw dislocations occur as particular modal solutions of the paraxial wave equation expressed in cylindrical coordinates. The paraxial wave equation is a particular form of the scalar Helmholtz equation [35]:

$$\nabla_{\mathrm{t}}^2 \psi - 2ik\frac{\partial \psi}{\partial z} = 0 \,, \tag{1.17}$$

where $\nabla_{\mathrm{t}}^2 = \partial^2/\partial x^2 + \partial^2/\partial y^2$ is the transverse Laplacian operator. By using a cylindrical coordinates system, Eq. 1.17 becomes

$$\frac{1}{r}\frac{\partial}{\partial r}\left(r\frac{\partial \psi}{\partial r}\right) + \frac{1}{r}\frac{\partial^2 \psi}{\partial \phi^2} - 2ik\frac{\partial \psi}{\partial z} = 0 \,. \tag{1.18}$$

It can be demonstrated that vortex solutions of Eq. 1.18 are also cylindrically symmetric around the z axis and possess an amplitude term with a finite transversal extension [36]. For this reason, solutions of this kind formally represent beams. Moreover, it turns out that these beams are hollow, since the EM field has to be zero along the z axis, where the OV is located and the phase can take any value between 0 and a multiple of 2π. Laser cavity modes are examples of solutions of this kind. For instance, the fundamental TEM_{01} mode harbors an OV along its symmetry axis [37]. Other possible singular solutions can be obtained by acting with differential operators on the plane wave representation of the fundamental Gaussian mode used as a seed function [38] and are represented by Bessel beams

[39], Bessel-Gauss beams [40] and L-G beams. All these solutions are very useful in applied physics because they are orthonormal.

1.4 Production of optical vortices

OVs produced with the spontaneous mechanisms described in Sect. 1.3 usually appear at random locations in the cross-section of the host wave field, unless we are dealing with hollow modes possessing peculiar symmetry properties. However, for practical purposes, the generation of OVs with predefined topological charges and located in particular positions is often required. For this reason, several methods to artificially produce OVs in light beams have been developed and are now widely used in laboratory experiments.

One of these methods consists in the astigmatic conversion of an HG$_{mn}$ Hermite-Gaussian laser cavity mode into an ℓ-charged L-G$_{p\ell}$ vortex mode [41]. The mode conversion is achieved by using two cylindrical lenses placed consecutively along the propagation axis z of the HG$_{mn}$ mode. The first cylindrical lens focuses the light along a transverse axis. In the focal plane, the beam undergoes a rotation by 45° around the z axis. This is equivalent of having a superposition of the original HG$_{mn}$ mode with a HG$_{nm}$ mode. The position of the second lens can then be chosen in order to produce a $\pi/2$ difference between the phases of the two modes. The final result is an LG$_{p\ell}$ mode, with $\ell = |m-n|$ and $p = \min(m,n)$.

OVs can be produced also by using phase modifying devices (PMDs), which are optical devices designed to imprint a certain vorticity to the phase front of an incident beam. Among them, the most efficient [42] are computer-generated holograms and spiral phase plates (SPPs).

1.4.1 Computer-generated fork holograms

A hologram represents the synthetic image of an object. Holograms are produced by using particular plates in which the information on the EM field of the objects that one wants to reproduce is recorded. Essentially, a holographic plate records the interference pattern obtained from the superposition of the EM field diffused by the object and a coherent reference beam. For this reason, when the plate is illuminated by a beam having the same characteristics of the reference beam, an image of the object will appear. Holographic plates can be used either in transmission or in reflection. In the following, I will refer only to the former.

Holography was invented in 1948 by Gabor [43]. At that time, however, the production of holographic plates was limited by the absence of coherent sources that are strongly required to obtain stable interferograms. A great improvement of the holographic techniques was made possible only after the development of laser sources in the Sixties. Until now, two distinct types of transmission holographic plates have been developed: the on-axis Gabor holograms [43] and the off-axis Leith-Upatnieks holograms [44]. A Gabor hologram produces both virtual and real images of the object along the same axis. Therefore, an observer will always see a superposition of the two images. Instead, with the Leith-Upatnieks holograms it is possible to separate the two images, since the holographic plate is produced by imposing an offset angle between the reference wave and the light scattered by the object.

In the mid Sixties, the synthesis of holographic plates was further improved with the aid of computers [45]. In fact, computers allow to easily calculate the complex amplitude of the EM field propagated from the object to the hologram plane, which is then encoded as a real non-negative function (a matrix of points with real values). There are many advantages offered by the computer synthesis of an holographic pattern, as it is not affected by problems related to the coherence of the source of the reference beam or to the environmental conditions (vibrations, turbulence, etc.). However, the most important property of computer-generated holograms is the possibility of reproducing optical fields of any kind, also light beams. For this reason, computer-generated holograms have been readily used to produce and study light beams containing screw wavefront dislocations [46, 47, 48, 49].

The holographic pattern obtained by computing the interference of the reference wave with a vortex beam is different if the former is a plane wave or a spherical wave. In the first case, the pattern of the interferogram is similar to that of a grating with a central fork-shaped dislocation [46]. This is the reason why they are usually called fork holograms (FHs). Fig. 1.2a shows an example of a

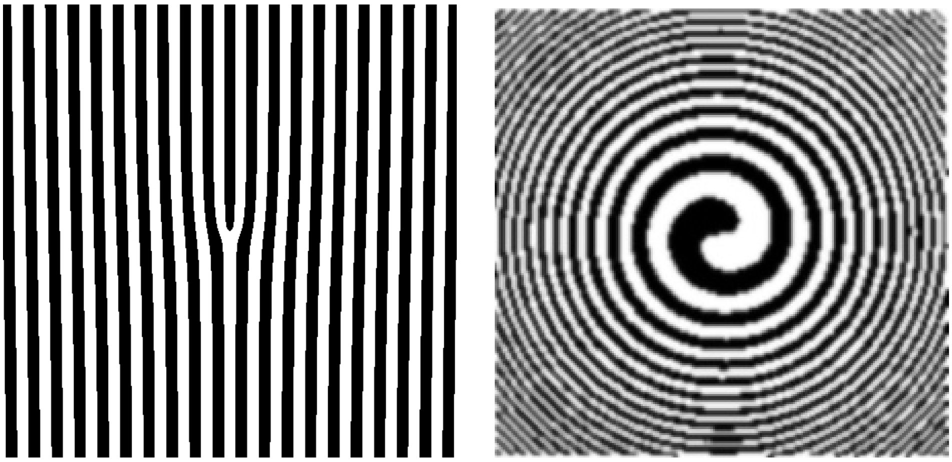

(a) Fork hologram (b) Spiral hologram

Figure 1.2 – Examples of computer-generated hologram designed to produce OVs with $\ell = 1$.

FH with just one central dislocation. When a monochromatic beam with a wavelength λ intersects perpendicularly a FH, the grating structure ideally produces an infinite number of diffraction orders. The angle ϕ_m subtended by the direction of an order m with respect the propagation axis of the input beam is given by the usual grating equation [50]

$$\Lambda \sin \phi_m = m\lambda \ , \tag{1.19}$$

where Λ is the spatial separation of the grooves of the grating far away from the center. Instead, if the reference beam is a spherical wave, then the interferogram pattern will assume a spiral-like shape similar to that of a Fresnel zone plate [47] (see Fig. 1.2b). Such a *spiral hologram* diffracts an incident beam too, but the diffraction orders are found at different positions along the propagation axis. For the purposes of the experiments that will be discussed in Sect. 2 and 3, FHs are more useful than spiral holograms because it is always possible to simultaneously inspect different diffraction orders without changing the position of the observation plane. Therefore, in the following I will present only the properties of FHs.

The object that we want to reproduce is a ℓ-charged vortex beam having a field

$$u_{\mathrm{obj}} = A_{\mathrm{obj}} \exp(\mathrm{i}\ell\,\theta)\,, \tag{1.20}$$

where A_{obj} is a real amplitude factor and $\theta = \arctan(y/x)$ is the azimuthal angle in the (x, y) plane perpendicular to the z axis. The reference beam is represented by a plane wave with a constant amplitude A_0 and a wave vector k lying in the (x,z) plane that subtends an angle ψ with the z axis. The corresponding field distribution is

$$u_{\mathrm{ref}} = A_{\mathrm{ref}} \exp\left(-\mathrm{i}\,k\,x\,\sin\psi\right) = A_{\mathrm{ref}} \exp\left(-\mathrm{i}\frac{2\pi x}{\Lambda}\right)\,, \tag{1.21}$$

where $\Lambda = \lambda/\sin\psi$. Assuming for simplicity $A_{\mathrm{obj}} = A_{\mathrm{ref}} = A$, the interferogram produced by the two fields is:

$$I(x,\theta) = |u_{\mathrm{obj}} + u_{\mathrm{ref}}|^2 = 2A^2\left[1 + \cos\left(\frac{2\pi x}{\Lambda} + \ell\,\theta\right)\right]\,. \tag{1.22}$$

This represents the interference pattern that has to be imprinted in the holographic plate to obtain a FH. Eq. 1.22 may be used also to describe the transmission function of a FH. In this case, Λ has to be identified with the spatial period of the grooves away from the central dislocation. An alternative expression, useful for computational purposes, is obtained by using the Fourier transform [51, 52]:

$$T(r,\theta) = \sum_{k=-\infty}^{+\infty} T_k \exp\left[-\mathrm{i}k\left(\ell\,\theta - \frac{2\pi}{\Lambda} r\cos\theta\right)\right]\,, \tag{1.23}$$

where $r\cos\theta = x$. The beam containing the OV having the wanted topological charge ℓ is produced at the first diffraction order ($m = +1$). More generally, a beam formed at the m-th diffraction order harbors an OV with topological charge equal to $m\,\ell$.

The holographic plate in which a FH is recorded can modify either the amplitude and the phase of an incident light beam. The latter (phase holograms) are preferable for experimental reasons because they have a lower energy absorption and a higher diffraction efficiency. To obtain a phase hologram, the transmission function has to be translated into a variation of the thickness of the hologram material. Furthermore, the spatial resolution must be sufficiently high to resolve the interference fringes of Eq. 1.22. This problem was extensively addressed by Sacks *et al.* [53].

To improve the diffraction efficiency toward the first diffraction order, a FH can be also blazed. In this case, the transmission function can be written, in circular coordinates, as

$$T(r,\theta) = \exp\left[\mathrm{i}\frac{\delta}{2\pi}\,\mathrm{mod}\left(\ell\,\theta - \frac{2\pi}{\Lambda} r\cos\theta,\, 2\pi\right)\right]\ , \tag{1.24}$$

where δ is the amplitude of the phase modulation [4] and $\mathrm{mod}(a,\ b) = a - b\,\mathrm{int}(a/b)$.

1.4.2 Spiral phase plates

OVs can be produced in light beams also by using spiral phase plates (SPPs) [54]. These are helicoidal transmission optical devices that impose an azimuthally dependent phase retard on an incident optical field. An SPP is thus a transparent plate in which the thickness at a given position (r,θ) of its surface is proportional to the azimuthal angle [55]:

$$h(r,\theta) = h_s\,\frac{\theta}{2\pi}\ , \tag{1.25}$$

where h_s is the total thickness variation. This makes an SPP to resemble a smooth spiral ramp (see Fig. 1.3). In the central region the thickness varies suddenly from 0 to h_s. This represents the optical singularity that produces an OV into an incident optical field. SPPs have been successfully used not only in the visible region of the EM spectrum, but also at millimeter wavelength [56] and in the X-rays [57].

Consider a monochromatic light beam with wavelength λ propagating along an axis perpendicular to the (r,θ) plane. When this intersects an SPP exactly on its center, it will obtain an azimuthal phase variation which results in the appearance of a screw wavefront dislocation having a topological charge

$$\ell = \frac{\Delta n(\lambda)\,h_s}{\lambda}\ , \tag{1.26}$$

where Δn is the difference between the refraction indices of the SPP material and the surrounding medium. As a consequence, OVs with different topological charges will be produced at different wavelength, thus making the performances

---

[4] $\delta = 2\pi$ for a fork-hologram blazed at the first diffraction order.

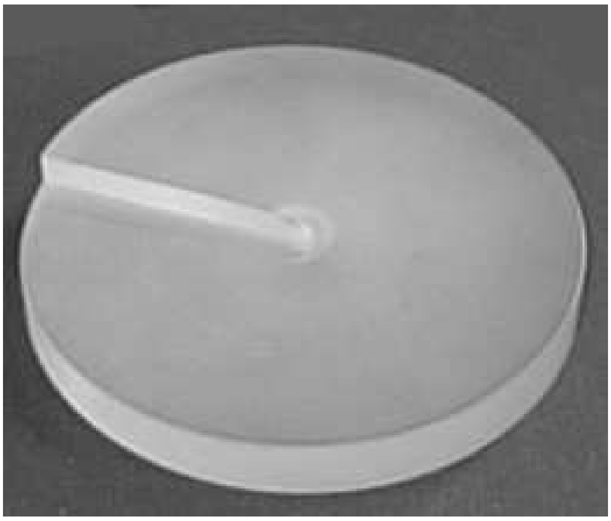

Figure 1.3 – An SPP used for millimeter wavelengths (from `http://www.st-andrews.ac.uk/~www_pa/Scots_Guide/MMWave/`).

of SPPs strongly dependent on the bandwidth of the incident beam. The transmission function of an SPP is a simple function of the azimuthal angle:

$$T(r,\theta) = \exp(\mathrm{i}\ell\,\theta)\ . \tag{1.27}$$

Here, ℓ is determined by the structural properties of the SPP and by the operating wavelength (Eq. 1.26). Differently from a FH, which imprints a vorticity with a topological charge depending on the diffraction order, an SPP has only the zero diffraction order. For this reason, the output beam propagates along the same axis of the incident beam.

1.4.3 Vortex beams produced with phase modifying devices

The action of a PMD on a incident optical field can be described using the scalar diffraction theory [58]. Consider a monochromatic wave field $u(x,y,z)$ propagating along the z axis and a PMD placed in the (x,y) plane. The PMD has a transmission function $T(x,y)$ and the optical singularity coincides with the origin of the coordinate system. Here, we consider PMDs that modulate only the phase of an incident wave. The diffracted field is calculated in another plane, (x',y'), parallel to the (x,y) plane and placed at a distance $z \gg \lambda$ from it. In any point P' in the (x',y') plane close to the z axis the resulting field can be determined by using the Fresnel-Kirchhoff formula [58]:

$$u(P') = \frac{1}{\mathrm{i}\lambda} \iint_{\Sigma} u(x,y,z)\, T(x,y)\, \frac{\exp(\mathrm{i}k\overline{PP'})}{\overline{PP'}}\, \frac{1+\cos\alpha}{2}\, \mathrm{d}x\, \mathrm{d}y \;, \tag{1.28}$$

where $\overline{PP'}$ is the distance between P' and a point P in the (x,y) plane and α is the angle between the z axis and the vector $\overrightarrow{PP'}$. Formally, the integral should be evaluated over the cross-section Σ of the PMD, however the integration is usually extended to infinite distances, for simplicity.

In many experimental situations, like those presented in this Thesis, the wave field $u(x,y,z)$ is represented by a cylindrically symmetric light beam, like a Gaussian beam. However, also in the simplest case in which the symmetry axis coincide with the z axis, the analytical evaluation of the integral in Eq. 1.28 presents many technical difficulties. For this reason, the problem of the diffraction of a light beam passing through a PMD was often tackled by using numerical simulations [59, 60, 55]. The mathematical formulation of the output vortex beam can be also expressed in terms of a superposition of orthogonal L-G modes [48, 56, 61].

Recently, an useful simplification of Eq. 1.28 has been found by Bekshaev & Karamoch [52] in the case of a FH. They showed also that the action of a FH on an incident light beam is similar to that of an SPP. In particular, the actions of these two PMDs are formally equivalent when the angle subtended by the first diffraction order of the FH, where the OV with the wanted ℓ is formed, is small [5], thus making the mathematical description of vortex beams produced with SPPs or FHs exactly the same. The only difference is that the output beam will propagate along the same axis of the input beam in the case of an SPP, or along a different axis, z', in the case of a FH.

Consider a PMD designed to produce an OV with topological charge ℓ (at the desired wavelength, if it is an SPP). To simplify the calculations (and take advantage of the symmetry of the geometry of the problem), it is more convenient to make use of the circular coordinates $r = \sqrt{(x^2+y^2)}$ and $\theta = \arctan(y/x)$. An incident beam $u(r,\theta,z)$ propagating along the z axis intersects the PMD exactly in

---

[5] This condition is usually satisfied, for visible wavelengths, by FHs having Λ in the range $\sim 10^{-2} - 10^{-1}$ mm.

the center ($r = 0$). The double integral in Eq. 1.28 can be analytically calculated only if the input beam and, thus, the output beam are paraxial. Within this approximation, the field of the vortex beam in the observation plane is given by:

$$u(\rho,\beta,z) = \frac{k}{2\pi \mathrm{i} z} \iint u(r,\theta,z)\,\exp(\mathrm{i}\ell\,\theta) \\ \times \exp\left\{\mathrm{i}\frac{k}{2z}\left[r^2+\rho^2-2r\rho\cos(\theta-\beta)\right]\right\} r\,\mathrm{d}r\,\mathrm{d}\theta\ , \quad (1.29)$$

where $\rho = \sqrt{x' + y'}$ and $\beta = \arctan(y'/x')$ are the circular coordinates in the (x', y') plane. We remind that the z axis appearing in this equation has to be replaced with the z' axis in the case of a FH.

The field amplitude of the output beam $u(\rho,\beta,z)$ can be calculated by substituting the appropriate mathematical expression of the input beam $u(r,\theta,z)$. Eq. 1.29 is very useful to study the propagation of the vortex beam from the PMD position to the observation plane. In particular, it allows to predict the amplitude and the phase distributions of the vortex beam at any distance z from the PMD.

1.5 Applications of optical vortices

The OAM associated to light beams carrying OVs represents a new degree of freedom associated to the EM field. The potential applications of OVs in applied physics have only begun to be explored. Molina-Terriza *et al.* [62] reviewed some of the landmark advances in the study and use of the OAM of light. Among these, the most promising seems to be those in optical communications, nanotechnologies and biology.

It has been shown that the OAM carried by a focused vortex beam can be mechanically transferred to small absorbing particles [63], causing them to rotate around the core of the OV nested in the wavefront [64]. This result allowed to readily apply OVs in optical trapping experiments [65]. Optical tweezers and spanners have been then developed to trap and move particles with dimensions ranging from tens of nanometers to tens of micrometers [66].

OAM states can be used to define a discrete Hilbert space with infinite dimensions. For this reason, light beams endowed with OAM carry a larger amount of information. This might be of considerable importance for free-space optical communications [67]. For the same reason, the technique of digital spiral imaging [68, 69] could be used to remotely acquire information about a particular medium.

The fact that individual photons can carry their own OAM has deep implications in quantum applications [62]. For example, photon OAM states could be used as practical realizations of quantum bits having arbitrary dimensions, the so-called qu$N$its. Courtial *et al.* [70] argued that, using the current techniques of production of PMDs, OAM states as high as $\sim 1000\hbar$ can be actually obtained. Such a high number of states encoded in a single photon is also of fundamental importance in the fields of quantum communications and quantum cryptography, as well as in optical data storage. Moreover, couples of photons generated by using the effect of spontaneous parametric down conversion have been demonstrated to be entangled in their OAM states [17]. Therefore, the use of photon OAM in quantum communication channels might help to enhance both the efficiency and the security of the transmission of data.

The presence and stability of wavefront dislocations were also investigated in the case of partially coherent light. By using the coherent-mode representation [71], in which a partially coherent beam is considered as a superposition of coherent modes, several authors showed the possibility of having a partially coherent beam containing OVs [72, 73, 74]. In particular, it has been demonstrated that a stable ring dislocation remains embedded in the cross-correlation function of a partially coherent beam while it propagates, regardless of the size of the transverse coherence length [75]. This property could be used in an optical filter which discriminates a coherent field from an incoherent background [60].

Quite recently, OVs and the related OAM of light attracted also the attention of the astronomical community. In fact, the exploitation of these properties of light could allow, in the future, to study astronomical phenomena in a different way, especially in view of the next generation of extremely large telescopes [76, 77]. For example, the fact that OVs appears in the wavefront of an EM wave passing through irregular media led to the argument that OVs could be naturally generated by some astrophysical environments, possibly related to turbulent interstellar media with density discontinuities on wide scale ranges, or to the distorted geometry around Kerr black holes [78].

The current applications of OVs in optical astronomy mainly concern instrumentations and are focused on developing methods of production and/or measure of optical vorticity in starlight beams. Berkhout & Beijersbergen [79] presented an efficient method based on a multipoint interferometer for probing the vorticity present in light beams coming from astronomical sources. The possibility of making ground- and space-based instruments to measure also the OAM present in the light emitted by astrophysical sources was also explored by Elias [80]. In this work, a generic systems-based calculation of the propagation of photon OAM from the celestial sphere to a detector was presented. In particular, it was demonstrated that the propagation of a vortex light beam through an aberrated telescope modifies the quantity of OAM originally carried. This instrumental OAM must then be calibrated, also including optical aberrations and atmospheric turbulence [81]. A further application proposed by Swartzlander [60] consists in *peering into the darkness* of OVs generated by a PMD inserted in the optical path of a Lyot coronagraph to improve the capability of direct imaging of extrasolar planets.

Optical vorticity was also proposed for application in radio astronomy at low frequencies ($\lesssim 1$ GHz), like those used in multi-array radio telescopes (e.g LOFAR and SKA). In fact, modern digital radio techniques can be used to model coherently the full EM field vectors in a beam. This might open the possibility to observe the solar corona [82] or to perform space plasma diagnostics [83]. It has been shown that plasma vorticity can be also transfered to an electron-neutrino beam [84]. This effect could be of relevant importance in the field of neutrino astrophysics.

In summary, the properties of light beams carrying OVs are attracting an increasing attention in astronomy, especially at visible wavelength. In this Thesis I will present and discuss some new promising instrumental applications of OVs, that could allow to open a novel window of information on the Universe.

Chapter 2

Overcoming the Rayleigh separability limit

2.1 Introduction

In 1879, Lord Rayleigh investigated the resolving power of some diffraction-limited optical instruments, with particular interest in telescopes and spectroscopes. He then formulated a criterion to assess the separability of two equally-luminous point sources observed with those optical instruments. The *Rayleigh separability criterion*, based on the analysis of the superposed diffraction patterns produced by the two sources, is rather arbitrary. However, it has the merit of being extremely simple. Lord Rayleigh himself said that *this rule is convenient on account of its simplicity and it is sufficiently accurate in view of the necessary uncertainty as to what exactly is meant by resolution* [85].

In the following, I will only consider the case of a telescope. As well known [58, 50], the diffraction image produced by a diffraction-limited telescope with a circular aperture of radius a can be mathematically expressed by the Airy distribution

$$I(\theta) = I(0)\left[\frac{2\mathrm{J}_1(ka\sin\theta)}{ka\sin\theta}\right]^2, \tag{2.1}$$

where $k = 2\pi/\lambda$ (λ is the wavelength), θ is the angle between the optical axis of the telescope and a point in the observation plane and J_m is a Bessel function of the first kind [12]. The image of a distant point source appears thus as a bright spot, also called Airy disk, surrounded by an infinite series of concentric rings having decreasing intensities.

The Rayleigh criterion states that the images of two point sources are said to be just resolved when the intensity maximum of one source (the center of the Airy disk) falls on the first intensity minimum of the other source [50]. As a result, the Rayleigh (angular) separability limit is defined by

$$\theta_R = 1.22\frac{\lambda}{D} , \tag{2.2}$$

where $D = 2a$ is the aperture diameter of the telescope. Fig. 2.1 shows how the two superposed Airy diffraction patterns appear for different separations of the sources. Generally, the intensity profile extracted along the direction of separation shows two peaks and a central dip, the intensity of which grows as the separation decreases. For this reason, the Rayleigh limit can be similarly defined by imposing that the first derivative of the intensity distribution at the position of the dip is zero [1]. We also remind that the historical definition of the resolving power of an optical instrument refers to a symmetric double-peaked profile with a central dip 5% lower than the intensity maxima [86].

The separability limit defined by the Rayleigh criterion is, thus, a fundamental physical limit of any optical system. However, techniques to overcome the limit imposed by the phenomenon of diffraction have been developed in certain special cases, especially in the fields of astronomical imaging [87] and microscopy [88]. For example, resolutions below the diffraction limit can be achieved with the use of superlenses made with artificially engineered metamaterials [89, 90] or super-resolving pupils [91], as well as by exploiting evanescent waves produced by very narrow apertures [92].

Swartzlander [60] proposed an alternative method to overcome the diffraction limit based on the analysis of the far-field intensity distributions produced by two vortex beams. Consider two infinitely-distant and incoherent point sources observed with a telescope having an aperture diameter D and a focal length f.

---

[1] A more stringent condition may require that also the second derivative of the intensity distribution is zero at the position of the dip. In this case, one obtain the so-called Sparrow separability criterion.

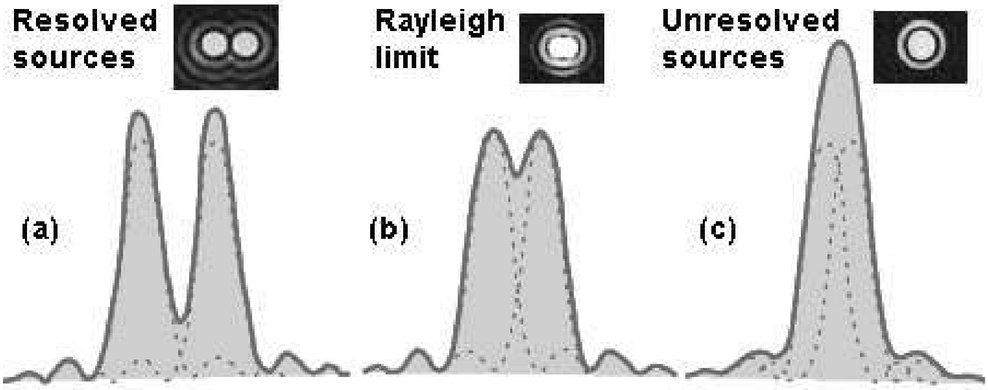

Figure 2.1 – Airy images of the intensity distributions of two point sources as observed with a diffraction-limited telescope, together with the corresponding radial profiles. The three cases corresponds to: *(a)* well resolved sources, *(b)* separation at the Rayleigh limit, *(c)* unresolved sources. Figure adapted from `http://hyperphysics.phy-astr.gsu.edu/Hbase/phyopt/Raylei.html`.

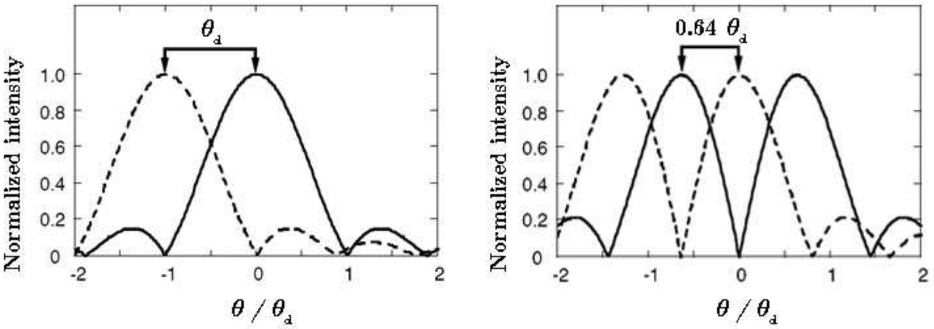

Figure 2.2 – Radial profiles of the superposed far-field intensity distributions produced by two plane waves passing through a finite SPP. In this examples we consider two different values of the topological charge of the produced OV: $\ell = 0$ (Airy patterns, *left panel*) and $\ell = 1$ (*right panel*). Figures adapted from Ref. [93].

The angular separation of the two sources is assumed to be small, i.e. $\alpha \ll 1$, therefore the EM waves entering the telescope aperture are nearly collinear. An SPP is placed just before the aperture, therefore the images formed at the focal plane of the telescope can be obtained from the Fourier transform of the product between the fields of two plane waves and the transmission function of the SPP (see Sect. 1.4.3). If $\ell = 0$, two Airy patterns will be observed. In this case, the two sources are considered to be separated when $\alpha = \theta_R$, that implies a spatial separation $\delta_R = 1.22\lambda f/D$ at the focal plane of the telescope. Instead, if the SPP imposes a topological charge different from 0, the original Rayleigh criterion cannot be applied because the images produced at the focal plane will not be Airy patterns. Instead, both the observed images will have a symmetric annular shape with a central dark spot in correspondence of the OV position. As a result, their radial profiles appears double peaked, as in the example shown in Fig. 2.2. The Rayleigh criterion can be similarly satisfied when one of the two intensity peaks of one source overlaps with the dark core of the other source. By applying this modified version of the Rayleigh criterion, it can be shown that the angular separation of the two sources corresponds to $0.64\,\theta_R$ for $\ell = 1$. By using SPPs with larger values of the topological charge, instead, the separation angles are larger than θ_R, namely $1.03\,\theta_R$ for $\ell = 2$, $1.37\,\theta_R$ for $\ell = 3$, $1.71\,\theta_R$ for $\ell = 4$ and so on.

If this method were used to improve the resolving power of telescopes, large SPPs would be required as they must be placed just before the aperture [2]. However, the production of such SPPs currently poses quite a number of technical problems, making extremely difficult the application of the method. We have however found a different optical solution which still allows to achieve sub-Rayleigh separabilities using OVs. In the following Sections, I will show how the Rayleigh limit may be better overcome by using a combination of integer and non-integer values of the OV topological charge.

---

[2] A similar situation is found in telescopes equipped with objective prisms.

2.2 Decomposition of a light beam in Laguerre-Gaussian modes

The generation of light beams containing OVs proceeds thanks to the insertion in the optical path of a PMD, as described in Sect. 1.4. L-G modes, that are mathematically expressed by Eq. 1.7, can be used to describe the field of the output beam since they represent a set of orthonormal basis [56, 61]. Using a circular coordinate system (r, θ), the intensity distribution of an L-G mode with $p = 0$ is given by

$$I(r,\theta) = \frac{2}{\pi w^2 \ell!}\left(\frac{r\sqrt{2}}{w}\right)^{2\ell} \exp\left(-\frac{2r^2}{w^2}\right) , \tag{2.3}$$

where ℓ is the topological charge of the nested OV and w is the width of the Gaussian envelope. This intensity distribution has a ring-shaped structure, with a central dark region. The maximum of intensity is found at a radial distance

$$r_{\max} = \frac{\sqrt{2}}{2} w \sqrt{\ell} \tag{2.4}$$

from the symmetry axis of an L-G mode and depends on ℓ as

$$I(r_{\max}) = \frac{2}{\pi w^2 \ell!} \ell^{\ell} e^{-\ell} . \tag{2.5}$$

For large values of the topological charge, $I(r_{\max})$ decreases as the inverse of the square root of ℓ [11].

Consider a monochromatic pencil of light propagating along the z direction of a reference frame S and a PMD placed on the (x, y) plane. The PMD has a finite spatial extension and its optical singularity is centered with the origin O. We assume that the transverse intensity distribution produced by the input beam on the PMD plane is described by Eq. 2.1 and, thus, is axially symmetric. This is the situation that is expected to occur when a PMD is placed at the focal plane of an unobstructed telescope. Note that this optical configuration is exactly the opposite of that used in Ref. [60]. When a beam of this kind intersects the active region of the PMD, the resulting diffraction image produced in the far-field is represented by a series of concentric rings produced by a superposition of an infinite number of coaxial L-G modes having different ℓ and p indices. This

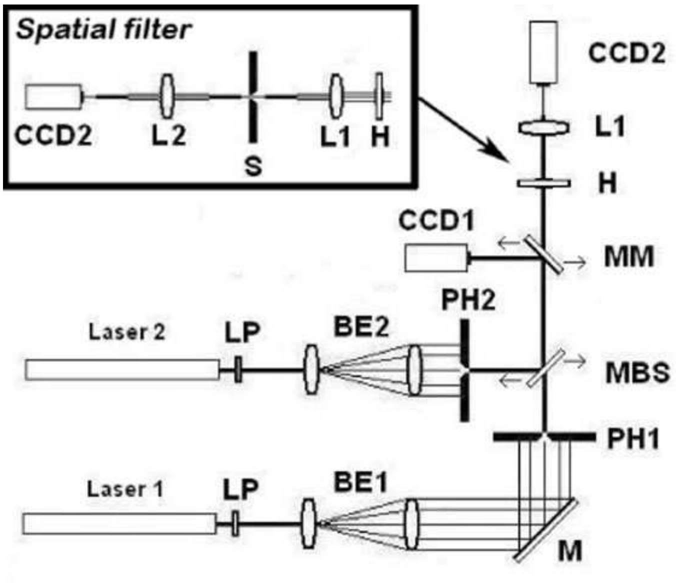

Figure 2.3 – Optical setup: *LPs* are neutral polarizing filters, *BE1* and *BE2* are beam expanders, *M* is a fixed mirror, *MBS* is a moving beam splitter, *MM* is a moving plane mirror, *L1* is a biconvex lens, *H* is the FH, *CCD1* and *CCD2* are two CCD cameras. The inset represents the spatial filter used in the experiment with white light: *L2* is a camera lens and *S* is a narrow slit. The two sources were obtained by using two distinct He-Ne lasers, in the monochromatic case, or a halogen lamp and two optical fibers in white light (not represented here).

occurs also in the case of strongly focused, tilted and off-axis input beams. The wavefront resulting from of such a weighted superposition may possesses an OV with a non-integer value of the topological charge [94, 95, 61, 96, 97].

2.3 Sub-Rayleigh separability with optical vortices

To study the properties of the far-field diffraction pattern previously introduced, we performed some experiments at the Laboratory of Optics of the Department of Astronomy (University of Padova). These experiments were carried out both with monochromatic and white light sources. We used the optical scheme shown in Fig. 2.3, in which the PMD was an $\ell = 1$ FH with 20 grooves mm^{-1}, an active area of 2.6×2.6 mm^2 and a $50\,\mu$m-sized optical singularity. The FH was blazed at the first diffraction order, where its efficiency was measured as

$\sim$ 70% at 630 nm. Two independent 632.8 nm He-Ne lasers were used to simulate the monochromatic sources, while white light sources were provided by a halogen lamp and two optical fibers having different lengths. In the experiment with white light we also corrected the chromatic dispersion of the FH by spatially filtering the first diffraction order with a $\sim$ 1 mm slit placed on the Fourier plane of the achromatic lens *L1* (see the inset in Fig. 2.3).

The Airy diffraction patterns were produced by using two pinholes with equal diameters of 400 μm. These were illuminated by the two independent beams previously collimated with a beam expander. The FH was placed perpendicularly to the optical axis, at a distance $d = 430$ mm from the two pinholes. The derived Fresnel number, $F \simeq 0.15$, was sufficient to satisfy the Fraunhofer diffraction conditions and, thus, obtain Airy diffraction patterns on the FH plane [50]. This was further verified by analyzing the spot images with the *CCD1* camera, after the insertion of a moving mirror inclined by 45° in the optical path (see Fig. 2.4, bottom row). The measured ratio between the distances of the first two maxima of the diffraction pattern with respect to the center of the Airy disk was 1.59, close to the value 1.64 predicted for a perfect Airy pattern.

While carrying out the experiments, the axis of one beam was always centered with the optical singularity of the FH. In this way, it produced a vortex beam containing an OV with an integer topological charge $\ell = 1$. The other beam, instead, could be shifted using a moving beam splitter in different positions of the FH, starting from the center. As a result, the output beam hosted an OV with a non-integer ℓ. The central dark regions of the far-field intensity patterns produced by the two diffracted beams beyond the FH were always superposed, because they were generated by the same optical singularity of the FH. In any case, to prevent modifications of the topological charges of the OVs due to tilts, the two beams were kept parallel with a tolerance of $0.17\,\mu$rad.

The experimental diffraction images obtained in monochromatic light are shown in the central row of Fig. 2.4. The Rayleigh criterion limit calculated for the $400\,\mu$m aperture of the pinholes is $\theta_R = 1.93$ mrad, corresponding to a linear separation $\delta_R = 834\,\mu$m on the FH plane. As a comparison, numerical simulations of the expected far-field diffraction patterns are reported in the upper row

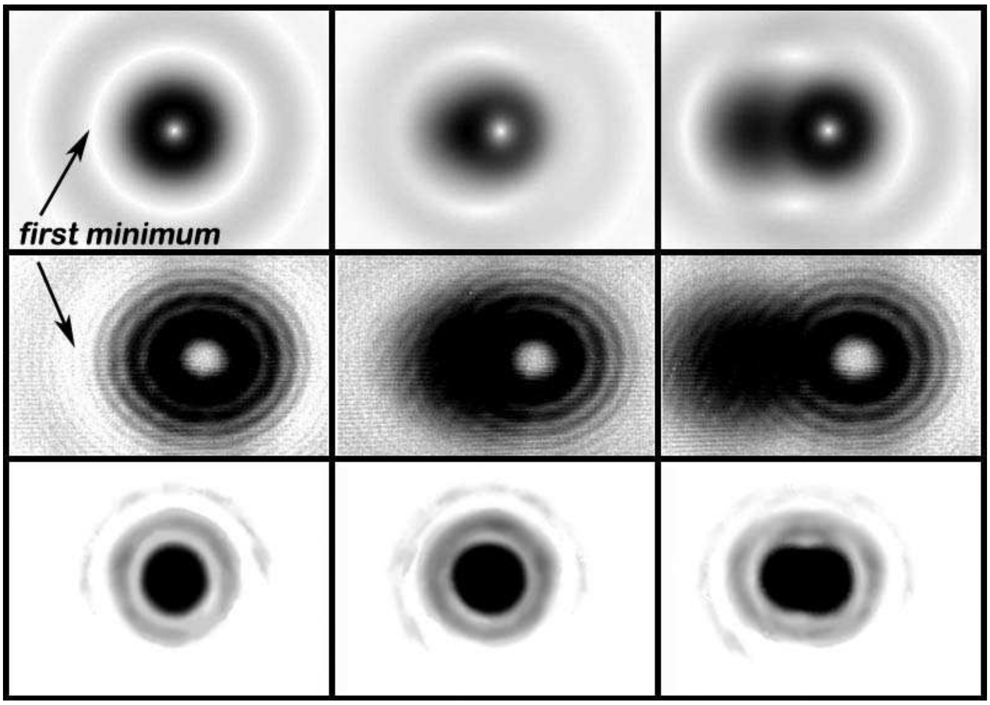

Figure 2.4 – Images of the separation of two close monochromatic sources having the same intensity. *Upper row*: numerical simulations of the far-field diffraction patterns generated with an $\ell = 1$ FH. *Central row*: the corresponding experimental images observed with the *CCD2* camera. *Bottom row*: Airy patterns of the two sources as observed with the *CCD1* camera. *Left column*: superposed sources. *Central column*: sources separated by 0.42 times the Rayleigh criterion limit. *Right column*: sources separated by 0.84 times the Rayleigh criterion limit.

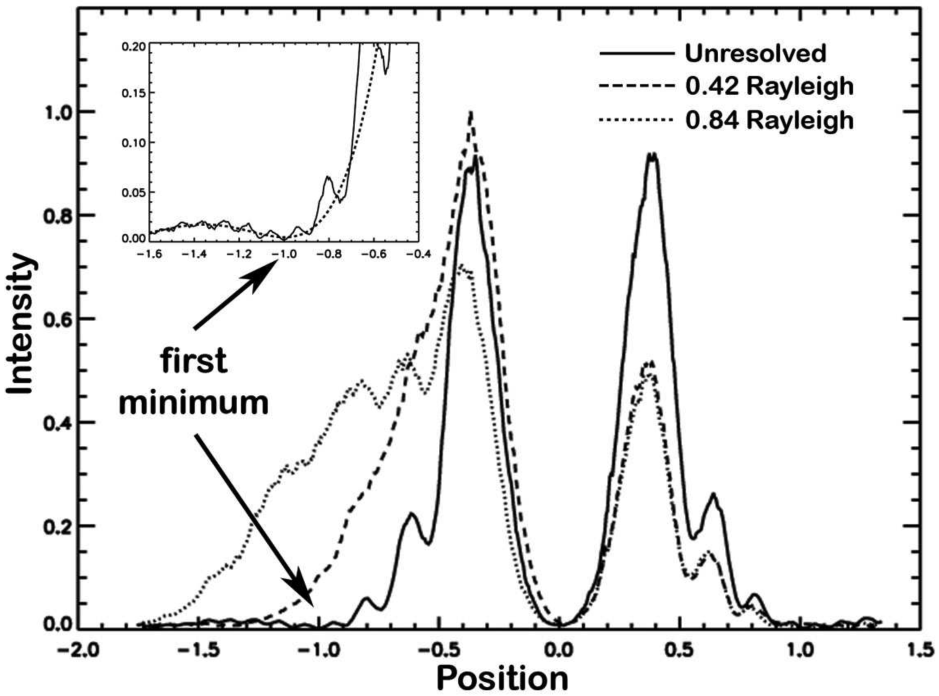

Figure 2.5 – *Main panel*: experimental intensity profiles of the superposed diffraction patterns produced by the two monochromatic sources. The intensity scale is normalized to the value of the peaks produced with unresolved sources. The three cases shown here refer to the same separations of Fig. 2.4. When one of the two sources is shifted to an off-axis position on the FH plane, the combined profile becomes clearly asymmetric. *Inset*: zoom of the position of the first minimum of the diffraction pattern produced by the Airy disk. The dotted curve represents the result of numerical simulations.

of the same Figure. The details of these numerical simulations are explained in Appendix A.1. All the images presented in the first column of Fig. 2.4 correspond to perfectly superposed sources. In the second column the two sources are separated by $0.42\,\delta_R$, while in the third column they are separated by $0.84\,\delta_R$. In all cases, the separation of the two sources is below the diffraction limit, as also shown by the corresponding Airy pattern presented in the bottom row.

The intensity profiles extracted along the direction of separation of the superposed OV diffraction patterns shown in Fig. 2.4 are plotted in Fig. 2.5. As we can see, these profiles always show two peaks. However, they become more and more distorted as the linear separation δ increases. When $\delta = 0$, the profile is symmetric and the two peaks have the same intensity given by the exact superposition of two identical diffraction patterns. When $\delta \neq 0$, the intensity of one of the two peaks decreases much faster than the other one, the latter tending to reach the intensity level of the single source. As the separation increases, the intensity measured at the position of the first external minimum of the combined profile (indicated in Fig. 2.5) monotonically increases, as shown in Fig. 2.7. This behavior can be interpreted as the effect of the contribution of the asymmetric transverse profile produced by the off-axis source [61, 98] containing an OV with a non-integer topological charge. In fact, the OV nested in the on-axis beam has always $\ell = 1$. Instead, the topological charge of the off-axis OV tends progressively to 0 as $\delta \to \infty$.

We tested the separability of the two monochromatic sources in the range $0 \leq \delta \leq 700\,\mu\text{m}$, with steps of 35μm. For each step, we measured the intensity ratio between the two peaks of the observed profile along the direction of separation. The experimental data, shown in Fig. 2.6, are in good agreement with the theoretical curve obtained with our numerical simulations. We find that the intensity ratio reaches a minimum value of 0.48 when the separation is $\sim 0.42\,\delta_R$. By approximating the Airy disk with a Gaussian, we estimate a topological charge $\ell \simeq 0.4$ for the OV produced by the off-axis source at that position. The main panel of Fig. 2.6 reports also the data obtained in white light that, at small separations, seem to decrease more smoothly than the monochromatic data. The lower inset of Fig. 2.6 reports the positions of the main peaks of the simulated

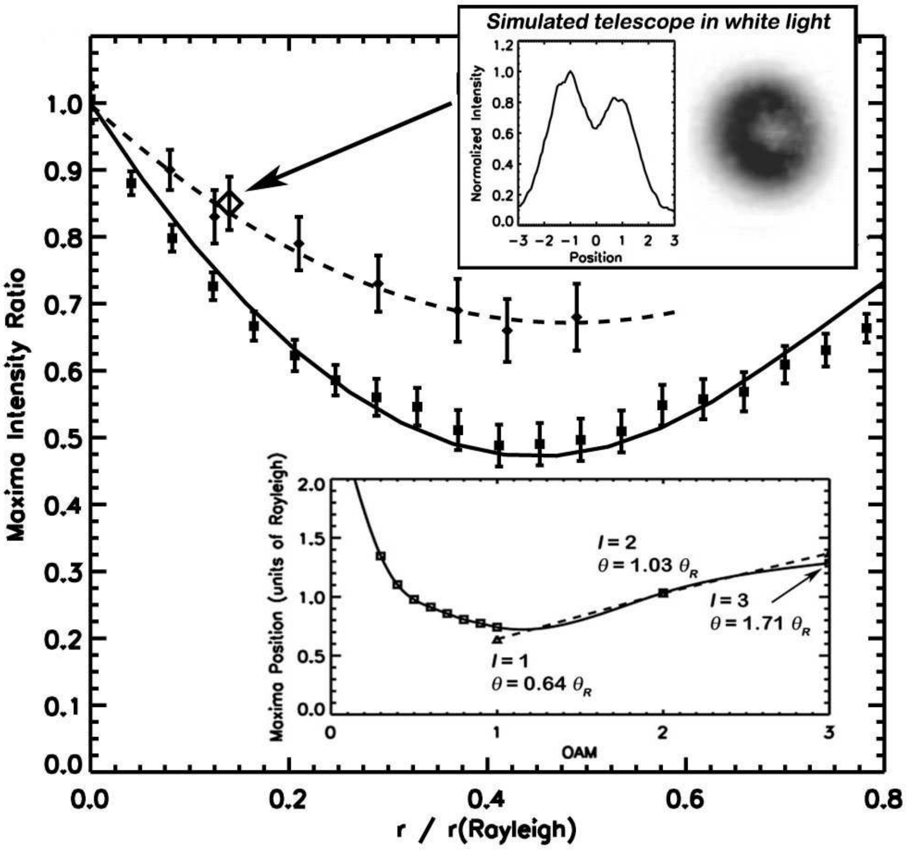

Figure 2.6 – *Main panel*: ratio between the intensities of the peaks of the superposed OV profiles vs. the separation of the sources. The solid line represents the theoretical expectation for monochromatic light, while the superposed dots and errorbars are the experimental data. The dashed line is an interpolation of the experimental data obtained in white light. *Lower inset*: positions of the maxima of the diffraction patterns (in units of the Rayleigh radius) vs. the topological charge ℓ (here indicated with OAM). Triangles show the angular separations between two sources with equally-charged OVs, as calculated in Ref. [60]. *Upper inset*: white light diffraction pattern produced by two equally luminous simulated stars as seen with a diffraction limited telescope (diamond in the main panel).

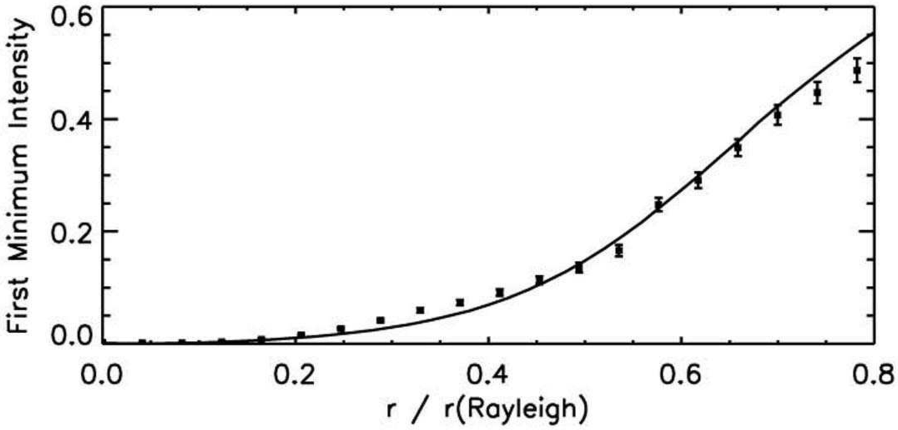

Figure 2.7 – The intensity of the first external minimum (see Fig. 2.5) of the combined profile produced by two equally intense sources plotted in function of the off-axis shift. The solid curve is derived from numerical simulations. Dots and error bars refer to our experimental results. The intensity scale is normalized with respect to that obtained for the two superposed sources.

diffraction patterns (in units of the separation δ_R) as a function of the estimated ℓ values. If we consider only the positions of the intensity peaks with respect to the dark core, sub-Rayleigh separations are achieved only for $0.45 < \ell < 2$, with a minimum at $\sim 0.7\,\delta_R$. The separations obtainable with the method discussed in Ref. [60] by using two OVs with identically charges $\ell = 1, 2, 3$ are also shown.

Our experimental results suggest that sub-Rayleigh separabilities can be achieved by analyzing the relative intensities of the asymmetric peaks produced by the superposed diffraction patterns. We might then mimic the historical definition of the resolution limit [86] and assume that two identical sources are just resolved when the intensities of the asymmetric peaks differ by at least 5%. Obviously, the actual separability depends on the signal-to-noise ratio (SNR) associated to the experimental data. However, with our optical setup, we could reach a theoretical separability 50 times better than the Rayleigh limit in the monochromatic case. Analogously, the results obtained in white light suggest a separability about 10 times better then the Rayleigh limit. This lower resolution is mainly due to the non-perfect spatial filtering and lower degree of coherence of the sources. In the upper inset of Fig. 2.6 we show a successful application of this separability criterion in white light. We experimentally simulated the OV images produced by a double star with an angular separation $\sim$ 10 times below the Rayleigh limit, as observed with an F/16 diffraction-limited telescope having an aperture of 122 cm (like the Galileo telescope in Asiago). The result of this simulation is consistent, within the errors, with the experimental data obtained in white light.

Chapter 3

Optical vortices with starlight

3.1 Introduction

Among the potential applications of OVs in astronomy, the most promising seems to be those in super-resolution and in coronagraphy. The former is better achievable with $\ell = 1$ OVs, as it is shown in Chapter 2, while in the second case only evenly-charged OVs generated by a perfect Airy diffraction pattern ensure the total rejection of the light of the on-axis source [99]. In both cases, OVs are produced by using a PMD placed at the focal plane of a telescope. Indeed, these astronomical applications would give their best performances with instruments placed outside the atmosphere. Ground-based telescopes, instead, will always feel the detrimental effects of the atmospheric turbulence, even with adaptive optics. Therefore, it is important to know how the seeing can affect the pattern of OVs generated by stellar sources. A first investigation in this field has been done by Jenkins [100] in a paper concerning coronagraphy. However, the actual structure of OVs produced in starlight beams observed with ground-based telescopes has never been studied in detail. For this reason, we performed some experiments of production of OVs at the 122 cm Galileo telescope in Asiago.

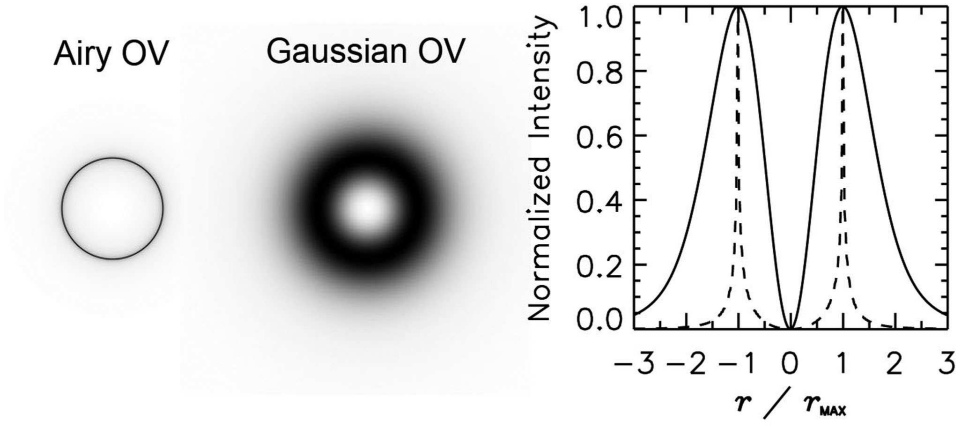

Figure 3.1 – Numerical simulations of the OV images produced in the far-field by $\ell = 1$ monochromatic by beams with an Airy (*left*) and a Gaussian (*center*) amplitude distributions. The transverse sizes of the input beams were chosen in order to produce annular patterns with the same maximum intensity radius $r_{\max}$. *Right panel*: the corresponding radial profiles. The solid line refers to a Gaussian OV, while the dashed line refers to an Airy OV. The intensity scale of the two profiles has been normalized to the corresponding maximum value.

3.2 Optical vortices with ground-based telescopes

The pattern of an OV generated with a PMD placed near the focal plane of a telescope strongly depends on the transverse intensity distribution produced by the stellar beam, i.e. the point spread function (PSF). We remind that, if an axially symmetric and monochromatic beam intersects on-axis a PMD, the observed far-field image presents a circular symmetry with a central dark region (an annular shape). Instead, if the beam is shifted off-axis, the dark region appears displaced off center and the observed pattern loses its circular symmetry.

The PSF generated by a point-like stellar source at the focal plane of a diffraction-limited telescope is described by the an Airy intensity distribution $I_{\mathrm{A}} \propto \left[J_1(r)/r\right]^2$, where $r = ka\sin\theta$ ($k = 2\pi/\lambda$ and a is the aperture radius of the telescope). Instead, for an uncompensated ground-based telescope, the PSF of a stellar source is degraded by the atmospheric turbulence and consists in a central nearly-Gaussian core with a radius determined by the seeing and an exponentially decreasing outer halo [101]. When the centroids of the stellar PSFs produced in these two limiting conditions coincide with the optical singularity of the PMD, OVs with same integer topological charge ℓ are generated. A vortex beam produced by a monochromatic Gaussian beam (*Gaussian OV*), like those produced by the seeing, can be well described in terms of Kummer functions [52]. This is quite different from the OV produced by a diffraction-limited beam (*Airy OV*). In this case, the analytical expression of the resulting beam can be obtained by inserting in Eq. 1.29 an Airy amplitude distribution for $u(r, \theta, z)$ [99]:

$$
\begin{aligned}
u(\rho, \beta) \propto\ & \frac{4\pi}{\mathrm{i}^{\ell}}\, \mathrm{e}^{\mathrm{i}\ell\beta} \\
\times & \begin{cases} \left(\dfrac{\rho}{a}\right)^{\ell} \dfrac{\Gamma(1+\ell/2)}{\Gamma(1+\ell)\,\Gamma(1-\ell/2)}\, {}_2\mathrm{F}_1\left[1+\dfrac{\ell}{2}, \dfrac{\ell}{2}; 1+\ell; \left(\dfrac{\rho}{a}\right)^2\right] & \text{if } 0<\rho<a \\ \left(\dfrac{a}{\rho}\right)^{2} \dfrac{\Gamma(1+\ell/2)}{\Gamma(2)\,\Gamma(\ell/2)}\, {}_2\mathrm{F}_1\left[1+\dfrac{\ell}{2}, 1-\dfrac{\ell}{2}; 2; \left(\dfrac{a}{\rho}\right)^2\right] & \text{if } \rho>a \end{cases},
\end{aligned}
\tag{3.1}
$$

where Γ is the Euler gamma function and ${}_2\mathrm{F}_1$ is a hypergeometric function [12]. As an useful example, Fig. 3.1 shows the numerical simulations of the far-field intensity distributions produced by the two types of monochromatic vortex beams, together with their radial profiles (see Appendix A.2 for details). Here, both the beams contain a single-charged OV in their axis and have the same maximum intensity radius r_{max}. As we can see, the phase singularity produces a null intensity at the center. However, a major difference resides in the shape of the intensity maxima of their radial profile: an Airy OV possesses sharp and narrow peaks, whereas those of a Gaussian OV are smooth and broad. This characteristics can be generalized also for OVs with higher values of the topological charge, with the additional condition that even-valued Airy OVs have zero intensity for any $r < r_{\mathrm{max}} = a$. We recall that the structures of the observed far-field diffraction patterns are not significantly changed even in the case of slightly converging stellar beams like those produced by telescopes with high focal ratios [52].

3.3 Experimental setup

An important task in the cited astronomical applications of OVs consists in keeping a stellar PSF exactly on-axis of the PMD for all the duration of the ob-

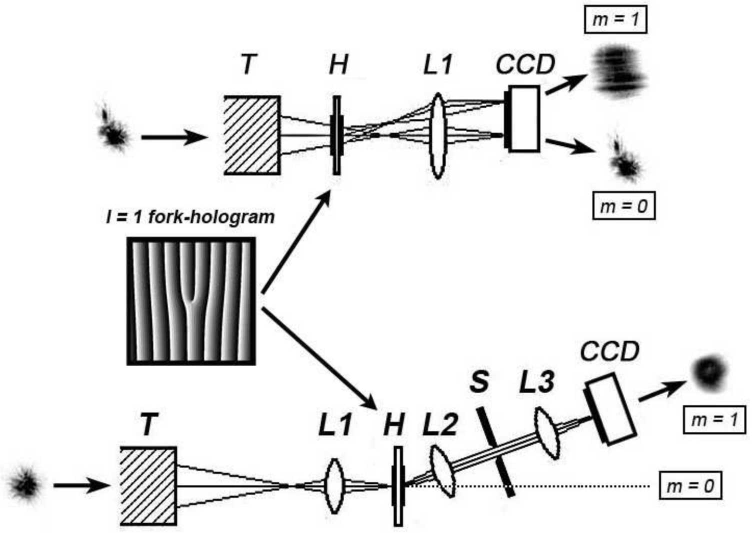

Figure 3.2 – Optical setups, without (*top*) and with (*bottom*) spatial filter. *T* is the telescope; *L1, L2, L3* are lenses; *H* is the $\ell = 1$ FH (its pattern is depicted in the middle of the figure); *S* is the slit. Stellar speckle patterns are sketched on the left of the optical setups, while the output images at the zeroth and first diffraction orders are on the right. All angles and displacements are exaggerated for clarity.

servation. In fact, the atmospheric turbulence causes the stellar beam to wander around the line of sight (see Ref. [102] for a comprehensive review of atmospheric optical effects). Therefore, we need to know the actual position of the stellar image in the focal plane of the telescope where the PMD is placed. In our observations, we tried to solve this problem by using the Lucky Imaging approach [103, 104]. The Lucky Imaging is one of the speckle imaging techniques used as alternative to adaptive optics. It basically consists in collecting a large number of images with exposure times shorter than the turbulence timescale ($\sim 10-100$ ms in the optical/near-infrared). A single nearly diffraction-limited image can occasionally be produced when most of the stellar light falls in a single bright speckle. Such *lucky exposures* [105] can be selected and, then, properly combined to produce a high-quality image. Here, we have adopted the obvious additional criterion of selecting only those exposures where the target was centered with the optical singularity of the PMD.

In our observations we used the two different optical setups sketched in Fig.

3.2. Images were collected with a fast CCD camera with 660 × 494 pixels ($7.4 \times 7.4\,\mu\text{m}^2$), 16 bit dynamical range and spectral response ranging from 4000 to 6700 Å peaked at 5200 Å. This CCD camera allowed us to partially correct the stellar PSF for the seeing effects (see Sect. 3.5).

An $\ell = 1$ FH blazed at the first diffraction order was used to modify the phase structure of the incoming starlight beam and thus produce an OV. The FH was obtained from a quartz plate by means of electron beam lithography. It has 38.5 grooves mm^{-1} (spatial period $\Lambda = 26\ \mu\text{m}$) and an active area of $2.6 \times 2.6\ \text{mm}^2$. Due to technical limitations, the depth of the grooves was subdivided in 8 discrete levels. The FH was blazed at the first diffraction order with a diffraction efficiency of ∼ 80% at 702 nm. With this device, we were able to simultaneously observe both the stellar speckle image, at the zero-th diffraction order, and the OV pattern at the first diffraction order. The choice of $\ell = 1$ avoided some possible experimental complications, as OVs with higher topological charges might become unstable within the instrumental optical path and split in single-charged ones [1].

In Sect. 1.4, I mentioned that the action of a FH is different if the input beam is monochromatic or if it is polychromatic. At a given diffraction order $m \neq 0$, the intensity distribution produced by a monochromatic and axially symmetric beam intersecting the FH exactly on-axis has an annular shape. Instead, if we are not using monochromatic light, which is usually preferable while observing faint stellar objects, the ring-shaped structure will be modified [106]. Each single spectral component will be dispersed at a different angle according to the usual grating equation. However, OVs with the same topological charge will be produced at all wavelengths. Therefore, the intensity pattern produced by a non-monochromatic vortex beam will appear as a ring stretched along the direction of the dispersion with a central dark strip. To correct the effect of spectral dispersion, we could also use a the spatial filter made with a 0.1 mm slit, S, placed in the Fourier plane of the collimating lens $L2$ (see the optical setup sketched in the lower part of Fig. 3.2). The slit essentially acts as a tunable bandpass filter with a flat spectral response. Therefore, by limiting the spectral range to ∼ 300 Å in the visible, we could somehow restore the annular shape of a monochromatic OV [107].

3.4 Observations and data reduction

Our observations were carried out in May 2005 with the Galileo 122 cm telescope in Asiago. This is a Cassegrain telescope with a parabolic primary mirror having an effective diameter of 120 cm and a hyperbolic secondary mirror having an effective diameter of 32.7 cm. The total focal length is $\sim$ 19 m, thus the telescope has an F/16 focal ratio, with a focal plane scale of $10.9'' \text{ mm}^{-1}$. The telescope is equipped with a Boller & Chivens spectrograph that does not allow to directly access the Cassegrain focal plane [1]. For this reason, an additional 45° mirror had to be placed on the optical path.

The targets of our observations were the multiple system Rasalgethi (α Her) and the single star Arcturus (α Boo). α Her is a visual binary composed by two spectroscopic binary systems which are presently separated by $4.7''$: α Her A, formed by an M5 Ib-II semiregular variable ($V = 2.7 - 4.0$) plus a fainter companion separated by $0.19''$ [108], and α Her B, containing a G0 II-III giant ($V = 5.4$) and a secondary which separation was spectroscopically estimated as $0.0035''$ [109]. Instead, α Boo is a single star with visual magnitude $V = 0.04$ and spectral type K1.5 III. For both objects, we collected a large number of frames with a short exposure time. To select the best frames we proceeded as follows:

1. when the zero-th diffraction order was visible, we determined the full width at half maximum (FWHM) of the target PSF, after the subtraction of the mean sky level, and then selected the best 10% frames;

2. we further selected the frames in which the target was also on-axis by analyzing the intensity profiles of the observed OVs at the first diffraction order;

The mechanical design of the lower setup of Fig. 3.2 prevented the observation of the zero-th diffraction order. In this case, we could only select those frames in which the observed images did present a symmetrical structure indicating that the target beam crossed the center of the FH.

---

[1] See `http://www.astro.unipd.it/osservatorio/telescopio.html` for details.

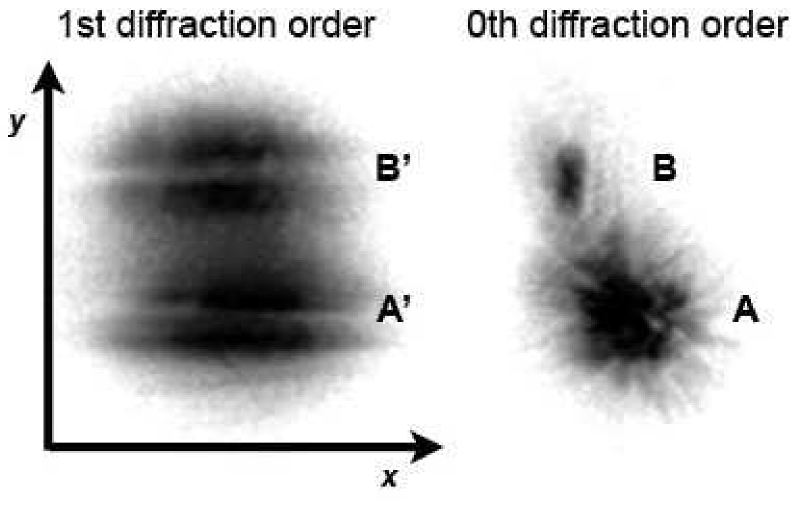

Figure 3.3 – Image (*right*) and dispersed OVs (*left*) of α Her A and B obtained by adding the selected best 10% frames. Intensities are displayed in a squared greyscale. The OV profiles were taken along the y axis, perpendicular to the direction of dispersion x.

3.4.1 First experiment: non-monochromatic optical vortices

We observed α Her in non-monochromatic light using the optical setup shown in the upper part of Fig. 3.2 that allowed us to simultaneously see the zero-th and the first diffraction order. The FH was placed 30 mm before the Cassegrain focal plane of the telescope, as we wished to achieve two conditions:

- to obtain well separated OV patterns on the focal plane of lens *L1* (this was however granted by the angular separation of the stars);
- to have both light beams large enough to cross a significant area of the FH and, in particular, the central singularity.

We set α Her A at the center of the optical system and, then, recorded a sequence of 860 frames at a time step of 70 ms. To select the best exposures, we used the PSF of the unsaturated α Her B component and found that 10% of the frames presented a FWHM below $\sim 1.6''$. The on-axis condition for α Her A was further recognized when the peaks of the corresponding dispersed OV profile had the same intensity within the experimental errors. The images and the chromatically dispersed OVs resulting from the summation of all the selected best frames are

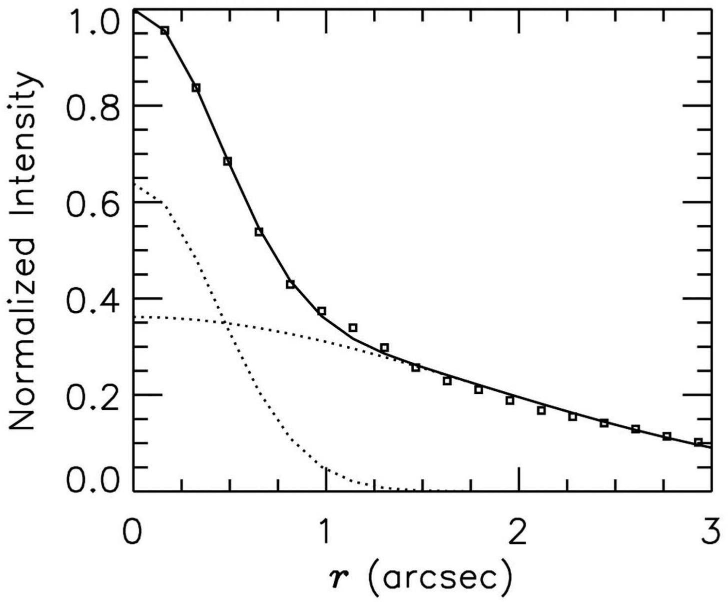

Figure 3.4 – Radially-averaged profile of the PSF of α Her B obtained by adding the selected best 17% frames (open squares). The solid line represents the best-fit model constituted by two superposed coaxial Gaussians. The two Gaussians components are also shown separately (dotted lines), for clarity.

shown in Fig. 3.3. The average radial profile of the PSF of α Her B (see Fig. 3.4) is constituted by a Gaussian core superposed to a halo that we fitted with another coaxial Gaussian, for simplicity. The FWHM of the two Gaussians are $1''$ and $4.2''$ respectively, the latter being roughly consistent with the seeing. Fig. 3.6 shows the mean profiles of the OVs obtained by averaging 10 pixels wide strips extracted perpendicularly to the dispersion.

3.4.2 Second experiment: narrow-band optical vortices

The observations of the single star α Boo were performed using the optical setup shown in the lower part of Fig. 3.2. The FH was placed at the focus of lens *L1*, where the scale of the telescope was magnified by a factor ~ 1.5. Thus, the FWHM of the PSF of the $\sim 3''$ seeing image was 0.5 mm. We introduced the also spatial filter to reduce the bandwidth, still ensuring a reasonable SNR ratio. We obtained a sequence of 890 frames with exposure times of 70 ms. Due to the non observability of the zero-th order, we could only look for the on-axis condition of

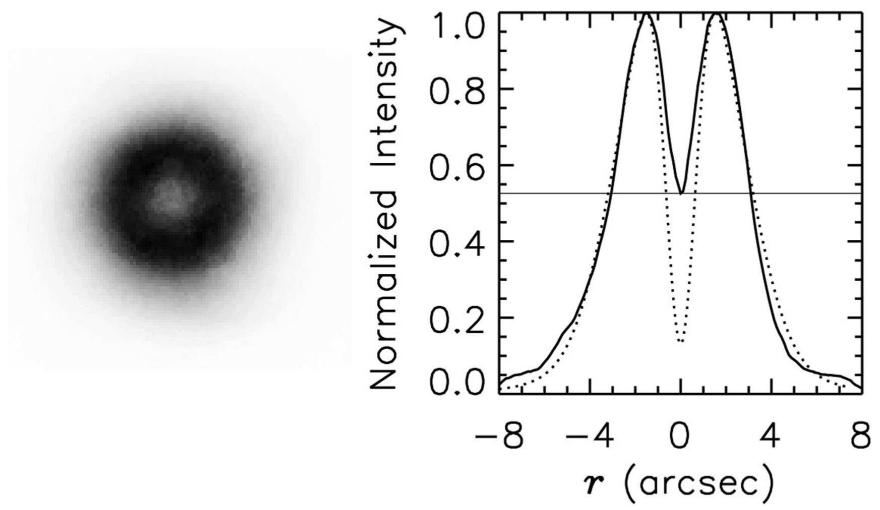

Figure 3.5 – *Left*: the narrow-band OV of α Boo obtained by summing the selected frames. The intensity is displayed in a squared greyscale. *Right*: profile of the OV across the direction perpendicular to the dispersion (solid line). The dotted line represents the numerical simulation of an $\ell = 1$ OV produced by a PSF modeled as described in the text, with a spectral range of 300 Å. The thin solid line indicates the observed intensity in the central dark region.

α Boo by analyzing the intensity profiles of the OV. We then choose those frames in which the ratios of the intensity peaks measured along two perpendicular axis across the OV were close to unity within 1% errors. In this way, we can reveal off-axis displacements along any radial direction. The mean OV pattern obtained by adding all the selected frames is shown in the left part of Fig. 3.5.

3.5 Results and discussion

3.5.1 Non-monochromatic optical vortices

The results of the first experiment were checked with numerical simulations of non-monochromatic OVs produced with an $\ell = 1$ FH (see Appendix A.2 for details). Since we set our FH in an intrafocal position, the image produced by the stellar beam did approximately coincide with that of the pupil. In our simulation we used a simplified image model made of an uniformly illuminated disk with radius a plus a central circular 7% obstruction, like that produced by the secondary

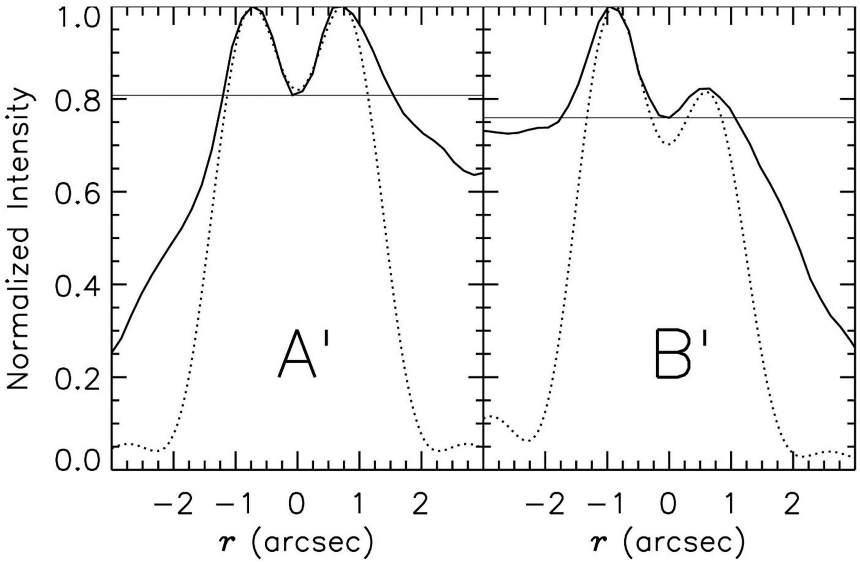

Figure 3.6 – Profiles of the OVs generated by α Her A (A', *left panel*) and α Her B (B', *right panel*) extracted along the y axis of Fig. 3.3. Dotted lines represent the numerical simulations of $\ell = 1$ chromatically dispersed OVs generated by a pupil image with a circular 7% obstruction. Thin solid lines are drawn at the intensity level of the central dips of the observed OV patterns.

mirror of the 122 cm Asiago telescope. To simulate the observed A' profile of Fig. 3.6 we assumed a perfectly on-axis pupil image, while the B' profile was reproduced by imposing an off-axis relative displacement $\rho/a = 0.31$, ρ being the linear separation of the two stars on the FH plane. For the off-axis OV we had also to consider that the displacement vector (the line joining α Her A and B) was rotated by an angle of 30° with respect to the dispersion. The intensity profiles of the simulated OV patterns are shown in Fig. 3.6. Both the observed A' and B' profiles show extended smooth wings not properly reproduced by our simplified simulations. This is probably due to the insufficiently short exposures which did not allow a proper compensation of the seeing effects. However, the most remarkable result concerns the ratio R of the two intensity maxima. By fitting with Gaussians the two peaks of the observed A' and B' profiles, we measured $R_{A'} = 0.995 \pm 0.005$ and $R_{B'} = 0.83 \pm 0.01$, respectively. These values are in good agreement with the values 1.0 and 0.82 predicted by our numerical simulations. We notice that the central dip in A' is 0.81 times the maximum intensity, still in agreement with the predicted value of 0.82. For B', instead, the dip is 0.76, while the numerical simulation predicts 0.70.

3.5.2 Narrow-band optical vortices

In the second experiment we observed the OV pattern produced by a single star focused at the center of the FH. Since in this case the zero-th diffraction order was not visible, we could not perform Lucky Imaging and the best 17% images were selected only on the basis of the circular symmetry of the OV. Using a spatial filter to limit the wavelength range, we were able to obtain a ring-shaped pattern similar to that of the Gaussian OV shown in Fig. 3.1.

Also in this case we simulated the OV pattern by assuming a PSF modeled with two Gaussians. Here we modeled also the effects of the dispersion over a spectral range of 300 Å. We find that the OV which best-fits the observed profile is produced by a stellar PSF composed by a dominant core with a FWHM of $3.6''$ and a fainter halo with $\sim 7''$ FWHM, its peak value being only 2% that of the narrower Gaussian. The simulated OV quite remarkably reproduces the wings of the observed one, but not so well the central dip which should be 13% the intensity of the two maxima, while it is observed at the 52% level (see the right panel of Fig. 3.5). This effect is very likely due to the loss of the starlight coherence produced by the bad seeing conditions plus our exposure times that were not short enough. Additional intensity inhomogeneities barely visible in the observed annular pattern can be ascribed to the presence of dust grains in the optical path and/or construction imperfections of the FH.

3.5.3 The relation between the maxima intensity ratio and the off-axis position

The results of our experiments represent a first test bench to relate the ratio R between the two intensity peaks of the far-field intensity profile to of the off-axis displacement ρ of the input beam on the FH plane. In the case of a monochromatic Gaussian beam, an approximate relation can be analytically derived, as detailed in Appendix A.4. For other types of beams, e.g. non-Gaussian and/or

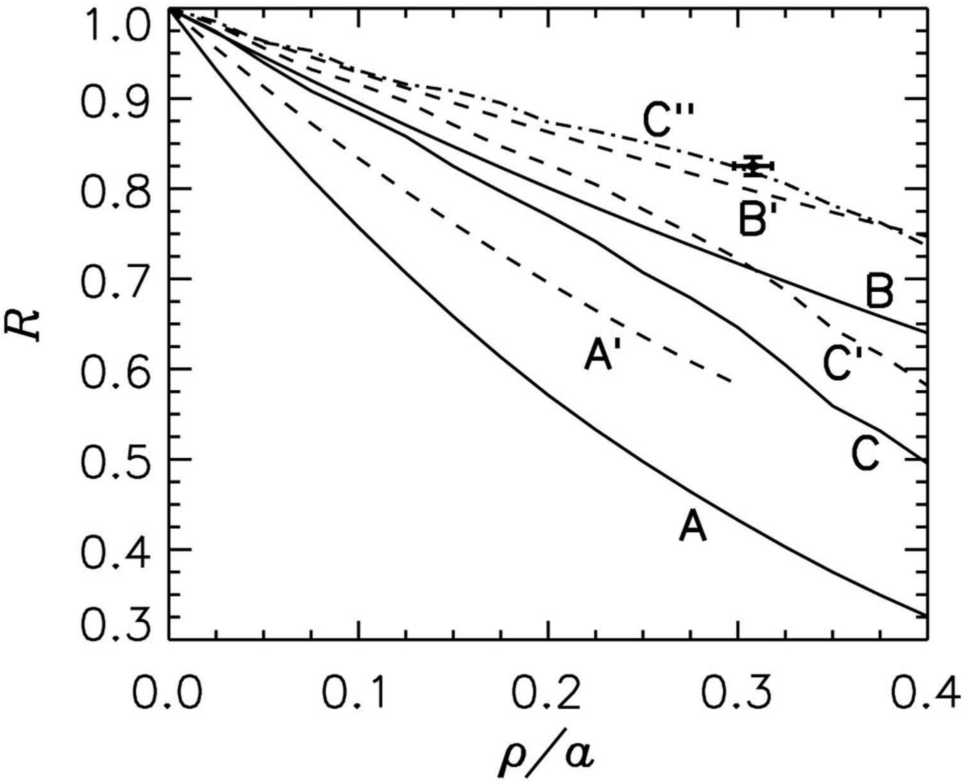

Figure 3.7 – Ratios of the intensity peaks plotted as a function of the off-axis relative position ρ/a for $\ell = 1$ OVs generated by: (*A*) a monochromatic Gaussian beam; (*A'*) a non-monochromatic Gaussian beam; (*B*) two monochromatic coaxial Gaussians; (*B'*) two non-monochromatic coaxial Gaussians; (*C*) a pupil image in monochromatic light; (*C'*) a pupil image in non-monochromatic light; (*C''*) a pupil image in non-monochromatic light where the off-axis displacement is inclined by 30° with respect to the dispersion. The experimental result obtained from the analysis of the OV generated by α Her B is indicated by the black dot (error bars are at the 1σ confidence level).

non-monochromatic, R has to be numerically evaluated.

We have performed numerical simulations of OVs produced by beams having various intensity distributions on the FH plane, namely a Gaussian, two Gaussians (like in our second experiment) and a uniform pupil with a 7% central obstruction (like in our first experiment). We have then calculated R for different values of the off-axis relative position ρ/a, where $2\,a$ is the FWHM of the intensity distribution in case of Gaussian beams or the outer diameter in case of the pupil image. The results of our simulations are shown in Fig. 3.7, for both monochromatic and non-monochromatic light. For a non-monochromatic Gaussian beam, R cannot be evaluated above $\rho/a = 0.3$ because the fainter peak becomes indistinguishable. As we can see, R decreases as the off-axis displacement increases for all the beams considered. This is the result of the off-axis migration of the central dark region. Furthermore, R decreases more rapidly for Gaussian OVs and, in general, for monochromatic light. The experimental result obtained from the analysis of the OV generated by α Her B is also reported in Fig. 3.7. Our measure fits quite well the theoretical curve *C"* obtained for an obstructed pupil displaced off-axis along a direction inclined by 30° with respect to the dispersion of the FH.

The capability of detecting small off-axis displacements depends on the precision of the measure of R. However, the calibration of the relation between ρ/a and R requires the knowledge of the beam structure, i.e. the profile of its intensity distribution. When the star is focused on the FH, a roughly corresponds to the FWHM of the PSF. This means that the maximum sensitivity can be achieved with nearly diffraction limited stellar images. For this reason, Lucky Imaging or adaptive optics would provide the best results. In our experiments with relatively bright stars we typically had SNR $\gtrsim 100$ and an error of $\sim 1\%$ associated to the measure of R. Assuming a PSF composed by two coaxial Gaussians, like that adopted to fit the OV pattern observed in our second experiment, the smallest off-axis relative displacement inferable from Fig. 3.7 is $\rho/a \sim 0.01$. Since the assumed PSF corresponded to $a = 1.8''$, the minimum angular displacement would be $0.02''$. We notice that this value is comparable to the astrometric precision of $0.01''$ obtained by fitting a single Gaussian to the core of the PSF of α Her B. Fig. 3.7 confirms that a higher precision is achievable when the PSF is modeled with a single Gaussian. In that case, still assuming a 1% error on R, the minimum off-axis relative displacement would be $\rho/a = 0.004$, for monochromatic beams, or $\rho/a = 0.006$, for non-monochromatic light.

Chapter 4

A new method to measure off-axis displacements of light beams

4.1 Introduction

Many applications of OVs require the knowledge of the exact amplitude distribution of a vortex beam generated with a PMD. As I have mentioned in Sect. 1.4.3, one of the first approach to this problem consisted in expressing the field of the output beam as a superposition of L-G modes with different radial indices p [48]. However, it was later found that a more precise description of the diffracted beams is provided by hypergeometric (Kummer) functions, for both SPPs [110] and FHs [53, 52]. We remind that these two type of PMDs behave similarly, provided that the angle subtended by the first diffraction order is small. As useful examples, I report the analytical solutions obtained for two particular cases of the input wave field: a plane wave and a Gaussian beam.

4.1.1 Plane waves

Consider a plane wave with unit amplitude propagating along the z axis:

$$u(r,\theta,z) = \exp(\mathrm{i}kz) \ . \tag{4.1}$$

The detailed analysis of the action of an infinitely extended SPP on an incident plane wave was carried out by Berry [110]. In this study, the mathematical form of the output field was obtained, under paraxial conditions, in terms of a superposition of plane waves, also including evanescent waves produced by the optical singularity. For an integer ℓ, the field of the vortex wave in the observation plane (x', y') is:

$$u(\rho, \beta, z) = \sqrt{\frac{\pi}{8}}\,(-\mathrm{i})^{|\ell|/2} \exp[\mathrm{i}(\ell \beta + z)] \\ \times \frac{\rho}{\sqrt{z}} \exp\left(\mathrm{i}\frac{\rho^2}{4z}\right) \left[\mathrm{J}_{\frac{|\ell|-1}{2}}\left(\frac{\rho^2}{4z}\right) - \mathrm{i}\,\mathrm{J}_{\frac{|\ell|+1}{2}}\left(\frac{\rho^2}{4z}\right)\right] , \quad (4.2)$$

where J_m is a Bessel function of the first kind [12]. The phase factor $\exp(\mathrm{i}\ell\beta)$ implies the presence of an OV with topological charge ℓ located all along the z axis, where the field amplitude is zero. If the topological charge induced by the SPP is not integer, the output wave possesses not only the singularity at $\rho = 0$, but also a step phase discontinuity along the positive x' axis ($\beta = 0$).

4.1.2 Gaussian beams

A Gaussian beam centered at $r = 0$, with the waist plane coinciding with the (x, y) plane, represents another useful expression for $u(r, \theta, z)$. In this case, the field amplitude in the (x, y) plane of the PMD is

$$u(r, \theta) = \exp\left(-\frac{r^2}{2b^2}\right) , \quad (4.3)$$

where the parameter b is related to the beam width. The mathematical description of the output beam obtained by calculating the integrals in Eq. 1.29 was found by Bekshaev & Karamoch [52]:

$$u(\rho, \beta, z) = \sqrt{\frac{\pi}{2}} \exp\left(\mathrm{i}\ell\beta\right) (-\mathrm{i})^{|\ell|+1} \exp\left(\mathrm{i}\frac{k\rho^2}{2z}\right) \frac{z_R}{z - \mathrm{i}z_R} \\ \times \sqrt{A} \exp(-A) \left[\mathrm{I}_{\frac{|\ell|-1}{2}}(A) - \mathrm{I}_{(\frac{|\ell|+1}{2}}(A)\right] , \quad (4.4)$$

where I_m is a modified Bessel function of the first kind [12], $z_R = kb^2$ is the Rayleigh range, $k = 2\pi/\lambda$ is the wave vector (λ is wavelength) and

$$A = \left(\frac{k\rho^2}{z}\right)^2 \frac{b^2}{4(1 - \mathrm{i}z_R/z)} . \quad (4.5)$$

(a) $\zeta = 0.01$, $b = 5$ (b) $\zeta = 0.1$, $b = 5$ (c) $\zeta = 1$, $b = 2$

Figure 4.1 – Intensity distribution of a vortex beam obtained at different distances from an $\ell = 2$ SPP. The value of parameter b (the width of the input Gaussian beam) has been reduced in the right panel for graphical reasons.

This expression is valid also in the case of an incident beam with a spherical wavefront, although z_R loses the physical meaning of Rayleigh range. Eq. 4.4 contains the familiar phase factor $\exp(i\ell\beta)$, which indicates that an ℓ-charged OV is located all along the z axis. In addiction, we see that the output beam retains the axial symmetry of the incident Gaussian beam. This property can be extended more generally to any input beam that is axially symmetric around the z axis.

Fig. 4.1 shows the intensity distribution $|u(\rho,\beta,z)|^2$ of the vortex beam described by Eq. 4.4 calculated at three different distances $\zeta = z/z_R$ from an $\ell = 2$ SPP. When ζ is small, the intensity pattern shows multiple rings produced by the interference between the wave regularly diffracted by the PMD and the diverging wave generated by the optical singularity of the PMD. The diffraction pattern assumes a single smooth annular shape as $\zeta \to \infty$.

4.2 Off-axis optical vortices

Consider an input beam with an amplitude distribution symmetric about the propagation axis. When such a beam intersects an SPP or a FH perpendicularly and exactly on-axis, it produces a circularly symmetric beam with a central dark region, where the field amplitude is zero. Any misalignment with respect to the central discontinuity would then produce an asymmetry of the observed intensity distribution [61] and the topological charge of the correspondent off-axis OV may have a non-integer value [98]. This changes also the OAM originally carried by the beam [17], thus producing an OAM spectrum [111, 96].

The experimental methods presented in Chapters 2 and 3 are based on the analysis of the asymmetry degree of the far-field intensity patterns produced by off-axis vortex beams. However, the problem of the diffraction of the light beams beyond the FHs has been tackled by using numerical simulations. Fortunately, the description vortex beam in terms of Kummer functions is valid also in the case of an input beam which axis does not intersects the optical singularity of a PMD [112]. I will use this approach in the following calculations.

4.3 Diffraction of a Gaussian beam intersecting on-axis a spiral phase plate

In this Section the problem of the Fraunhofer diffraction of a monochromatic Gaussian beam intersecting an SPP exactly on-axis is revisited. The geometrical configuration adopted here is sketched in Fig. 4.2. The SPP is placed in the (x, y) plane and the central optical singularity coincides with the origin of the (x, y) coordinate system. To take advantage of the geometrical symmetry of the problem, it is convenient to use a circular coordinates (r, θ), where $x = r\cos\theta$ and $y = r\sin\theta$. Thus, the transmission function of the SPP (Eq. 1.27) is just a complex function of the azimuthal angle θ:

$$T_\ell(\theta) = \mathrm{e}^{\mathrm{i}\ell\,\theta} \ , \tag{4.6}$$

where ℓ represents the strength of the optical singularity. In the following, we assume $\ell > 0$, as we will always operate with its absolute value. Consider, then, a paraxial Gaussian beam propagating along the z axis (that is also its symmetry axis) perpendicular to the SPP plane. This choice is important for practical applications, i.e. laser beams or starlight beams affected by atmospheric turbulence, as briefly discussed in Sect. 3.2. We assume that the field amplitude distribution of such a beam in the SPP plane is

$$A_G(r) = c\,\mathrm{e}^{-r^2/w^2} \ , \tag{4.7}$$

where c is a complex factor, possibly depending on the z coordinate, and w is related to the beam width. The observation plane (x', y') is located at a distance $f \rightarrow \infty$ beyond the SPP or, better, at the focal plane of a lens placed just behind the SPP (in this case, f would coincide with the focal length of the lens). The scalar field of the output beam in the observation plane is the Fourier transform of the product between the amplitude of the input beam and the SPP transmission function:

$$u_\ell(\rho,\beta) = \text{const} \iint A_G(r)\, T_\ell(\theta)\, \mathrm{e}^{-\mathrm{i}kr\rho\cos(\theta-\beta)/f}\, r\,\mathrm{d}r\,\mathrm{d}\theta \;, \tag{4.8}$$

where $k = 2\pi/\lambda$ is the wave vector, λ is the wavelength and (ρ,β) are the circular coordinates in the observation plane. To simplify the calculations, the SPP is considered as infinitely extended in the (x, y) plane. In addition, we use the scaled radial coordinate $r' = kr/f$ and introduce the quantities $w_0 = f/(kw)$ and c_0, the latter containing all the multiplicative constants. In this way, Eq. 4.8 becomes

$$u_\ell(\rho,\beta) = c_0 \int_0^{2\pi} \int_0^{\infty} \mathrm{e}^{-w_0^2 r'^2}\, \mathrm{e}^{\mathrm{i}\left[\ell\,\theta - r'\rho\cos(\theta-\beta)\right]}\, r'\,\mathrm{d}r'\,\mathrm{d}\theta \;. \tag{4.9}$$

The integral involving the angular coordinate θ can be evaluated by using the definition of the Bessel function of the first kind [12]:

$$\int_0^{2\pi} \exp\left[\mathrm{i}\left(\nu\,\theta - z\cos\theta\right)\right]\,\mathrm{d}\theta = 2\pi \mathrm{i}^{|\nu|}\,\mathrm{J}_{|\nu|}(z) \;. \tag{4.10}$$

Thus, the integral involving the spatial coordinate becomes a particular case of the Weber-Sonine formula [12]:

$$\int_0^{\infty} \mathrm{e}^{-a^2t^2}\, t^{\mu-1} \mathrm{J}_\nu(bt)\,\mathrm{d}t = \frac{\Gamma\left(\frac{\nu+\mu}{2}\right)\left(\frac{b}{2a}\right)^{\nu}}{2\,a^{\mu}\,\Gamma(\nu+1)}\; {}_1\mathrm{F}_1\left(\frac{\nu+\mu}{2};\nu+1;-\frac{b^2}{4a^2}\right) \;, \tag{4.11}$$

where ${}_1\mathrm{F}_1$ is a confluent hypergeometric function of the first kind. The final result is:

$$u_\ell(\rho,\beta) = c_0\,\mathrm{i}^{-\ell}\,\frac{\pi}{w_0^2}\,\mathrm{e}^{\mathrm{i}\ell\beta}\,\frac{\Gamma(1+\ell/2)}{\Gamma(\ell+1)}\,\eta^{\ell}\;{}_1\mathrm{F}_1\left(1+\frac{\ell}{2};1+\ell;-\eta^2\right) \;, \tag{4.12}$$

where $\eta = \rho/(2w_0)$. The presence of the phase factor $\mathrm{e}^{\mathrm{i}\ell\beta}$ implies that the output beam has an ℓ-charged OV nested on its wavefront.

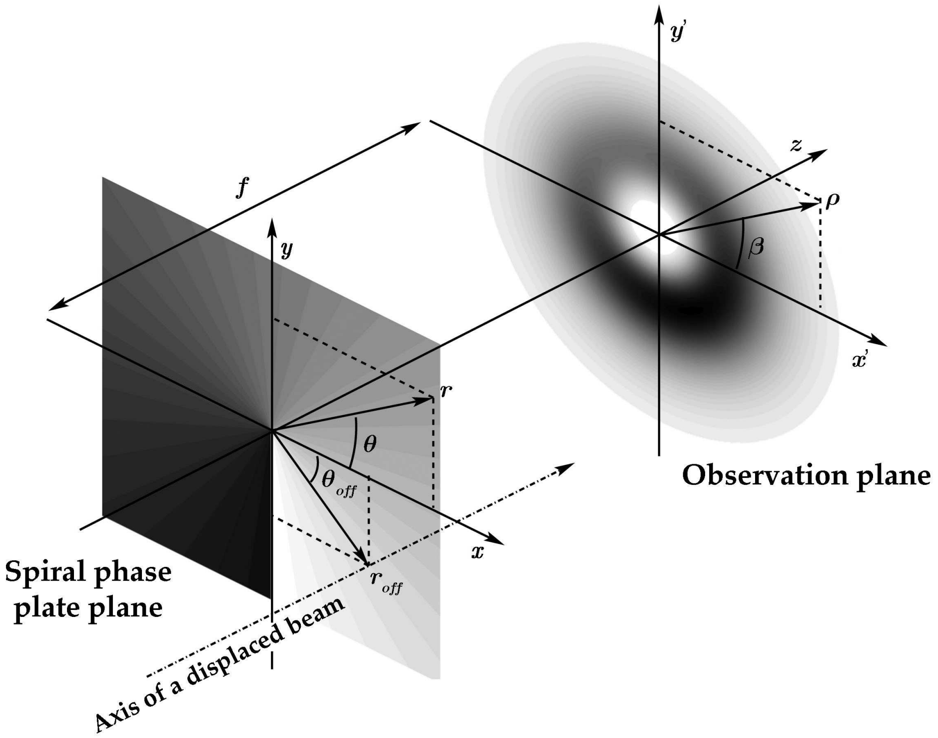

Figure 4.2 – The geometrical configuration adopted to study the Fraunhofer diffraction of a Gaussian beam beyond a spiral phase plate (see text for details).

We notice that the confluent hypergeometric function of the first kind in Eq. 4.12 can be reduced to elementary functions because of the special values assumed by its arguments:

$$
\begin{aligned}
&{}_1\mathrm{F}_1(a;2a-1;z) = \\
&\qquad 2^{2a-3}\Gamma\left(a-\frac{1}{2}\right)\mathrm{e}^{z/2}(-z)^{3/2-a}\left[\mathrm{I}_{a-\frac{3}{2}}\left(-\frac{z}{2}\right)-\mathrm{I}_{a-\frac{1}{2}}\left(-\frac{z}{2}\right)\right] \, . \qquad (4.13)
\end{aligned}
$$

Thus, a more useful expression of the amplitude distribution of the output beam is obtained by using the modified Bessel function of the first kind I_ν [53]:

$$
u_\ell(\rho,\beta) = c_0\,\mathrm{i}^{-\ell}\,\frac{\pi^{3/2}}{2w_0^2}\,\mathrm{e}^{\mathrm{i}\ell\beta}\mathrm{e}^{-\eta^2/2}\eta\left[\mathrm{I}_{\frac{\ell-1}{2}}\left(\frac{\eta^2}{2}\right)-\mathrm{I}_{\frac{\ell+1}{2}}\left(\frac{\eta^2}{2}\right)\right] \, . \qquad (4.14)
$$

Beams of this kind, also known as *Kummer beams* [52], are formally different from the commonly used L-G beams. If $\ell = 0$, the Bessel functions of half-integer index in Eq. 4.14 can be expressed in terms of the hyperbolic functions, according to

$$
\mathrm{I}_{-\frac{1}{2}}(z) = \sqrt{\frac{2}{\pi}}\,\frac{\cosh z}{\sqrt{z}} \qquad (4.15)
$$

$$
\mathrm{I}_{\frac{1}{2}}(z) = \sqrt{\frac{2}{\pi}}\,\frac{\sinh z}{\sqrt{z}} \, , \qquad (4.16)
$$

and combined together to give an exponential. In this case, the amplitude distribution of the output beam is still Gaussian, i.e. $u_0 \sim \mathrm{e}^{-\eta^2}$. If $\ell \neq 0$, we can derive an useful approximation for $\eta \to 0$ by using the series expansion of I_ν [12]:

$$
\mathrm{I}_\nu(z) = \left(\frac{z}{2}\right)^\nu \sum_{m=0}^{\infty} \frac{(z/2)^{2m}}{m!\,\Gamma(\nu+m+1)} \, . \qquad (4.17)
$$

We recognize that, near the z axis, the amplitude of an on-axis Kummer beam carrying an OV with topological charge ℓ could be represented by a superposition of amplitudes of L-G modes with $p = 0$ (see Eq. 1.7):

$$
\begin{aligned}
&u_\ell \sim \mathrm{e}^{-\eta^2/2}\eta^\ell \\
&\quad\times\left[\frac{1}{\Gamma\left(\frac{\ell+1}{2}\right)} - \frac{\eta^2}{2^2\Gamma\left(\frac{\ell+3}{2}\right)} + \frac{\eta^4}{2^4\Gamma\left(\frac{\ell+3}{2}\right)} - \frac{\eta^6}{2^6\Gamma\left(\frac{\ell+5}{2}\right)} + \mathcal{O}(\eta^8)\right] \, . \qquad (4.18)
\end{aligned}
$$

The dominant term is proportional to the amplitude of an L-G mode with index ℓ, while higher order terms are proportional to L-G modes with indices $\ell + 2m$, where $m \in \mathbb{N}$.

4.3.1 Properties of the intensity distribution

The intensity distribution of an on-axis Kummer beam is axially symmetric around the z axis and is described by:

$$I_\ell(\rho,\beta) \approx \left|u_\ell(\rho,\beta)\right|^2 = c_0^2\,\frac{\pi^3}{4w_0^4}\mathrm{e}^{-\eta^2}\eta^2\left[\mathrm{I}_{\frac{\ell-1}{2}}\left(\frac{\eta^2}{2}\right)-\mathrm{I}_{\frac{\ell+1}{2}}\left(\frac{\eta^2}{2}\right)\right]^2 . \tag{4.19}$$

As for L-G modes, the intensity pattern of a Kummer beam has an annular shape, with a central dark region where the intensity is zero. However, there are some fundamental differences between the two analytical descriptions.

For a Kummer beam the behavior of the intensity at large distances from the z axis is $\sim \eta^{-4}$. This can be calculated by using the asymptotic expansion of the modified Bessel function [12]

$$\mathrm{I}_\nu(z) \sim \frac{\mathrm{e}^z}{\sqrt{2\pi z}}\left[1-\frac{4\nu^2-1}{8z}+\frac{(4\nu^2-1)(4\nu^2-9)}{2!\,(8z)^2}+\cdots\right] \tag{4.20}$$

for $z \longrightarrow \infty$. The intensity distribution produced by an L-G mode, instead, decreases exponentially. Moreover, the radius of maximum intensity of an L-G mode is $\rho_{\max} \sim \sqrt{\ell/2}$ (Eq. 2.4), where the intensity attains the value

$$I(\rho_{\max}) \sim \frac{\ell^\ell\,\mathrm{e}^{-\ell}}{\ell!} , \tag{4.21}$$

while for a Kummer beam $\rho_{\max}$ is found by numerically solving the transcendental equation

$$\left(\ell+2\eta^2\right)\mathrm{I}_{\frac{\ell+1}{2}}\left(\frac{\eta^2}{2}\right)+\left(\ell-2\eta^2\right)\mathrm{I}_{\frac{\ell-1}{2}}\left(\frac{\eta^2}{2}\right)=0\,. \tag{4.22}$$

The calculation of the radii of maximum intensity obtained for a set of values of the topological charge $\ell = 0,1,\ldots,10$ (see Fig. 4.3a) suggests that $\rho_{\max}$ is linearly dependent on ℓ:

$$\frac{\rho_{\max}}{2w_0} = (0.37\pm0.01)+(0.470\pm0.002)\ell\,, \tag{4.23}$$

where 1σ errors have been obtained from a linear fit to the calculated values. A similar result was found also for OVs produced by a plane wave intersecting a circular phase mask with finite dimensions [113]. Fig. 4.3b shows the intensity calculated at $\rho_{\max}$ for the same set of topological charges.

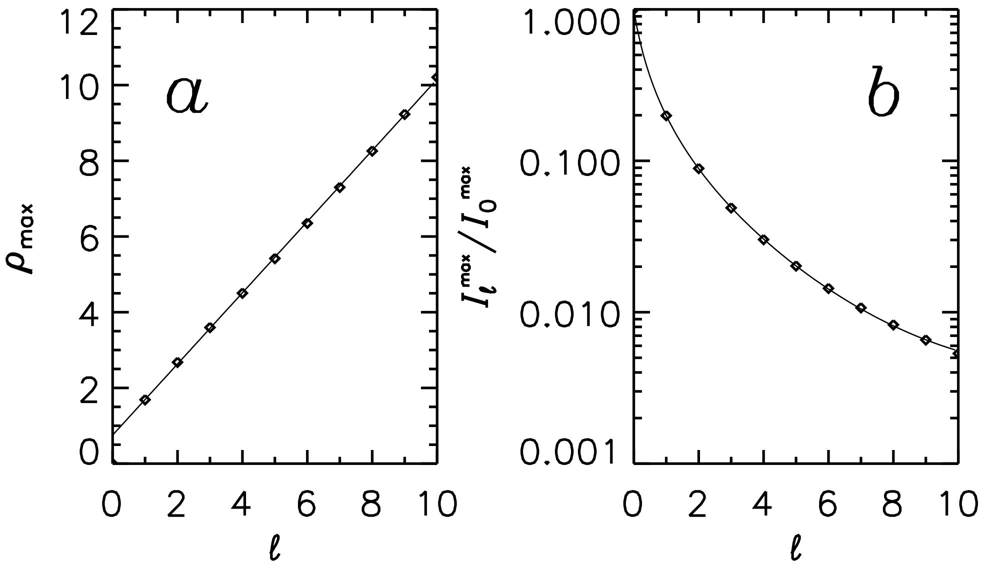

Figure 4.3 – Properties of the intensity distributions of on-axis Kummer beams having $\ell = 0, 1, \ldots, 10$. (*a*) Plot of the radius of maximum intensity $\rho_{\max}$ (in units of w_0) vs. ℓ. (*b*) Plot of the intensity calculated at $\rho_{\max}$ for different values of ℓ. The maximum intensity for $\ell = 0$ has been set to unity.

4.3.2 The effects of off-axis displacements

When the input Gaussian beam is displaced off-axis, so that its symmetry axis does not coincide with the z axis of Fig. 4.2, the intensity pattern produced in the observation plane is modified. The misalignment of the input beam can be decomposed into a translation in the (x, y) plane and an inclination angle ω with respect to the z axis. However, if ω is small, the modifications induced in the intensity pattern of the output beam are negligible [112]. For this reason, in our calculations we will consider only lateral displacements of the incident beam.

Let us assume that the Gaussian beam intersects the SPP in the position $(r_{\text{off}}, \theta_{\text{off}})$, as in the example shown in Fig. 4.2. In this case, the field of this input beam in the SPP plane is

$$A_G(r) = c\, \exp\left[-\frac{r^2 + r_{\text{off}}^2 - 2\, r\, r_{\text{off}} \cos(\theta - \theta_{\text{off}})}{w^2}\right]\,. \tag{4.24}$$

By inserting this expression in Eq. 4.8, we obtain:

$$\begin{aligned} u_\ell(\rho,\beta) &= c_0\,\mathrm{e}^{-w_0^2 {r'_{\mathrm{off}}}^2} \\ &\times \int_0^{2\pi}\int_0^{\infty} \mathrm{e}^{-w_0^2 r'^2}\,\mathrm{e}^{\mathrm{i}\left[\ell\,\theta - r'\rho\cos(\theta-\beta) - \mathrm{i}\,w_0^2 r' r'_{\mathrm{off}}\cos(\theta-\theta_{\mathrm{off}})\right]}\,r'\,\mathrm{d}r'\,\mathrm{d}\theta\ . \end{aligned} \tag{4.25}$$

Here, r'_{off} is the scaled radial coordinate obtained from r_{off}. Eq. 4.25 can be formally expressed as Eq. 4.9 by making the substitution [112]

$$\gamma\cos(\theta-\psi) = \rho\cos(\theta-\beta) + \mathrm{i}\,w_0^2 {r'_{\mathrm{off}}}^2\cos(\theta-\theta_{\mathrm{off}})\ , \tag{4.26}$$

where the quantities γ and ψ are defined as

$$\gamma^2 = \rho^2 + 4\mathrm{i}w_0^2 r'_{\mathrm{off}}\rho\cos(\beta-\theta_{\mathrm{off}}) - 4w_0^4 {r'_{\mathrm{off}}}^2 \tag{4.27}$$

$$\tan\psi = \frac{\rho\sin\beta + 2\mathrm{i}w_0^2 r'_{\mathrm{off}}\sin\theta_{\mathrm{off}}}{\rho\cos\beta + 2\mathrm{i}w_0^2 r'_{\mathrm{off}}\cos\theta_{\mathrm{off}}}\ . \tag{4.28}$$

Therefore, we can follow the same calculation procedure explained in Sect. 4.3. The resulting field of the output beam resembles that of Eq. 4.14 obtained under on-axis conditions:

$$\begin{aligned} u_\ell(\rho,\beta) &= c_0\,\mathrm{i}^{-\ell}\,\frac{\pi^{3/2}}{2w_0^2}\,\mathrm{e}^{\mathrm{i}\ell\psi}\,\mathrm{e}^{-w_0^2 {r'_{\mathrm{off}}}^2} \\ &\times \mathrm{e}^{-\gamma^2/8w_0^2}\,\frac{\gamma}{2w_0}\left[\mathrm{I}_{\frac{\ell-1}{2}}\left(\frac{\gamma^2}{8w_0^2}\right) - \mathrm{I}_{\frac{\ell+1}{2}}\left(\frac{\gamma^2}{8w_0^2}\right)\right]\ . \end{aligned} \tag{4.29}$$

In this case, a new exponential factor $\exp(-w_0^2\,{r'_{\mathrm{off}}}^2)$ appears, while the imaginary part of γ^2 represents an additional phase factor. As a result, the phase singularity is located neither on the beam axis, nor in the origin of the (x',y') plane, but is shifted in a position $(\rho,\beta) = \left(2w_0^2\,r'_{\mathrm{off}}, \theta_{\mathrm{off}} + \pi/2\right)$. This is the reason why the intensity distribution of the output beam becomes asymmetric [114] and shows two different peaks along the direction of the vortex core in the (x',y') plane. Fig. 4.4a shows an example of an off-axis OV produced with an $\ell = 2$ SPP. The lower and the higher peaks are labeled with A and B, respectively.

Now, since it is difficult to analytically study the properties of Eqs. 4.29 for different values of ℓ, we decided to perform numerical simulations (see Appendix A.2). The width w of the input Gaussian beam was parametrized in function of the full width at half of the intensity maximum, $2a$, such that $a = w\sqrt{\ln 2/2}$.

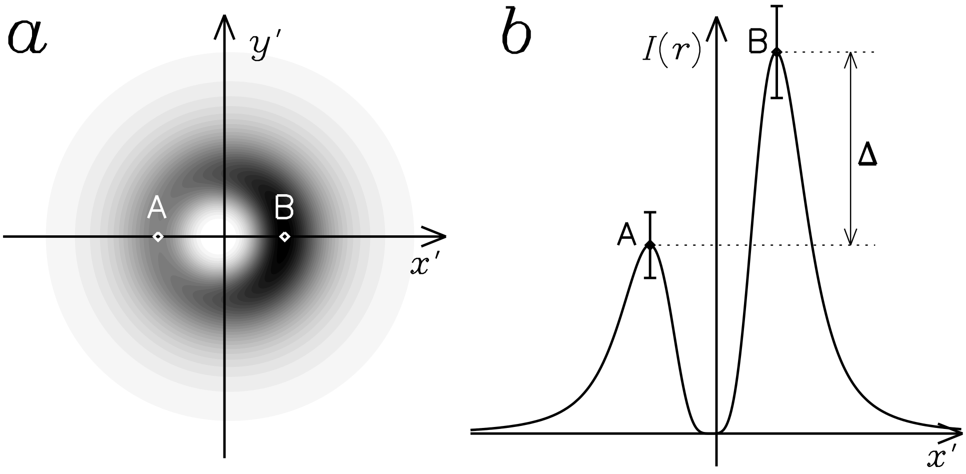

Figure 4.4 – Example of the far-field intensity pattern of a numerically-simulated off-axis vortex beam produced by an $\ell = 2$ SPP. The two diamonds indicate the positions of the two different intensity peaks A and B. (a) Contour plot of the intensity distribution obtained in the observation plane. (b) Intensity profile of the off-axis beam extracted along the x' direction. Δ is the difference between the intensities calculated in B and A. Examples of error bars are reported for both the intensity peaks.

We used values of the topological charge induced by the SPP in the range $\ell = 0, 1, \ldots, 10$, since with higher values we get misleading results using the two-dimensional Fast Fourier Transform algorithm. For each ℓ, we considered a number of off-axis displacements r_{off}/a of the input beam ranging from 0 to 1 with steps of 0.05 and computed the resulting intensity patterns.

We checked the consistency of our numerical simulations by comparing them to the analytical models (Eq. 4.29) for a number of values of ℓ and off-axis positions. To this aim, we previously normalized the intensities of both the simulated and the analytical patterns to the corresponding maximum values. Therefore, the B peak always has a normalized intensity equal to one (obviously, both the peaks A and B will have the same unity intensity if $r_{\text{off}}/a = 0$). The residuals of the subtraction of the theoretical intensity patterns from the simulated ones are typically within 10^{-4} for positions close to peaks A and B. We will then assume this quantity as the intrinsic error of our numerical simulations.

For all the numerically simulated OVs we obtained the intensity values at the

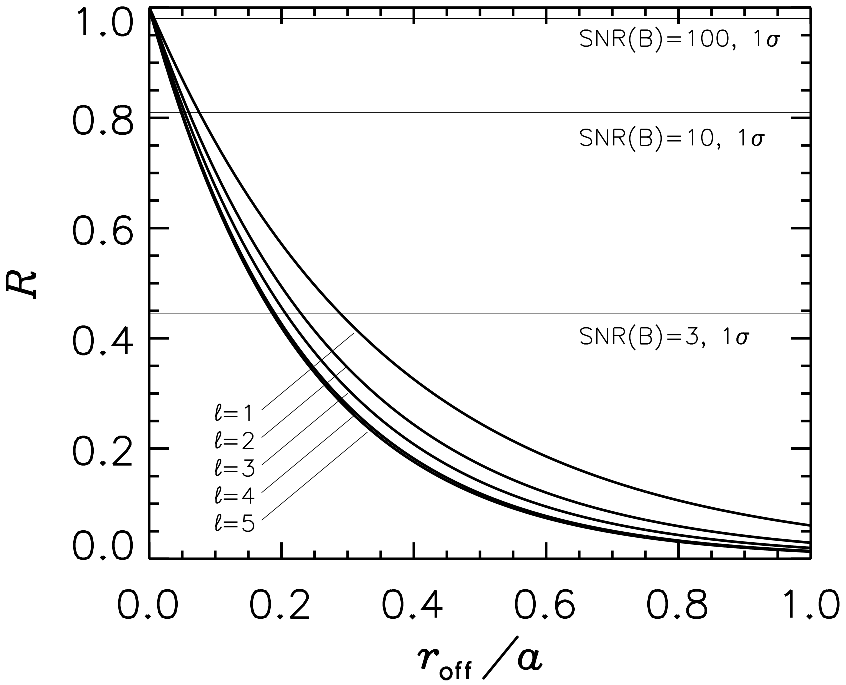

Figure 4.5 – Plot of the peaks intensity ratio R vs. the off-axis displacement of the input Gaussian beam obtained for different values of the topological charge induced by the SPP. Horizontal lines are drawn at the maximum values of R detectable at the 1σ confidence level for 3 values of the SNR ratio of the B peak.

ℓ	k_1	k_2
1	1.002 ± 0.001	2.808 ± 0.006
2	1.0012 ± 0.0007	3.534 ± 0.004
3	1.0004 ± 0.0005	3.928 ± 0.003
4	0.9995 ± 0.0008	4.259 ± 0.005
5	0.9990 ± 0.0009	4.338 ± 0.006
6	0.999 ± 0.001	4.432 ± 0.008
7	0.998 ± 0.001	4.456 ± 0.008
8	0.998 ± 0.001	4.509 ± 0.009
9	0.998 ± 0.001	4.573 ± 0.01
10	0.998 ± 0.002	4.756 ± 0.02

Table 4.1 – Best-fit values of parameters k_1 and k_2 of Eq. 4.30 obtained from least-square fits of the simulated curves of Fig. 4.5. The associated errors are given at the 1σ confidence level.

two peaks and calculated the quantity R defined as the ratio between the intensity I_A of the lower peak and the intensity I_B of the higher peak. We find that R rapidly decreases as the off-axis displacement increases for all the topological charges considered. The graphs showing the dependence of R on r_{off}/a for $\ell = 1,2,3,4,5$ are plotted in Fig. 4.5. All the curves are well represented by a simple exponential function:

$$R = k_1 \mathrm{e}^{-k_2 r_{\text{off}}/a} , \tag{4.30}$$

where parameters k_1 and k_2, obtained by best fitting the simulated curves, are listed in Table 4.1. From these results, it appears that k_2 depends on the topological charge ℓ as

$$k_2 = (4.64 \pm 0.05) - (2.9 \pm 0.2)\mathrm{e}^{-(0.47 \pm 0.05)\ell} , \tag{4.31}$$

while k_1 tends to remain close to unity.

4.4 The sensitivity of the method to reveal off-axis displacements

The off-axis displacement of the input Gaussian beam with respect to the central singularity of an SPP results in an asymmetry of the far-field intensity pattern. Eq. 4.30 reveals that the parameter R represents an extremely sensitive tool to detect such very small displacements, as also pointed out in Sect. 3.5.3. Actually, the sensitivity of a vortex beam to off-axis displacements has been used in a different way as an indicator of nanometric shifts in a speckle pattern [115] or as a non-interferometric method for the correction of small surface deviations on spatial light modulators [116]. Similar results could be obtained from the analysis of the mean square value of the resulting OAM spectrum [117].

Let us suppose to have an input Gaussian beam which symmetry axis is perpendicular to the surface of an SPP and observe the correspondent far-field image with a photoelectric detector like a CCD. In this way, if the beam is displaced off-axis, we can measure the intensity ratio R of the two different peaks, as defined in Sect. 4.3.2. The precision of this measurement is mainly limited by the SNR achieved in the observation, while additional errors might be introduced by construction imperfections of the SPP. The latter issue results in inhomogeneities of the observed intensity distribution. For this reason, efforts are currently made to improve the production quality of SPPs [55, 118, 119]. However, here we assume an ideal SPP so that the only limitations are due to the SNR. The noise of a CCD detector is mainly represented by the photon shot noise [120]. Assuming a pure Poissonian distribution of the collected photons, the uncertainties associated to the intensities I_A and I_B of the two peaks can be approximated by the square root of the signals, i.e. $\sigma_A = \sqrt{I_A}$ and $\sigma_B = \sqrt{I_B}$. We may then recognize $I_A \neq I_B$ at the $n\sigma$ confidence level when $\Delta = I_B - I_A \geq n\sigma_A + n\sigma_B$ (see Fig. 4.4b), that means

$$\Delta \geq n\left(\sqrt{I_A} + \sqrt{I_B}\right) \ . \tag{4.32}$$

If we introduce parameter R, this equation can be rewritten as a function of the only SNR associated to the intensity of the highest peak (SNR(B)). We find that the maximum peaks intensity ratio measurable at the $n\sigma$ confidence level is

$$R \leq \left(1 - \frac{n}{\mathrm{SNR}(B)}\right)^2 . \tag{4.33}$$

As useful examples, in Fig. 4.5 we draw three horizontal lines corresponding to the maximum R values 0.44, 0.81 and 0.98 detectable at the 1σ level for SNR(B) = 3, 10 and 100, respectively. By combining Eq. 4.30 with Eq. 4.33, we finally obtain the expression for the minimum off-axis displacement detectable at the $n\sigma$ confidence level:

$$\frac{r_{\mathrm{off}}}{a} \geq -\frac{1}{k_2} \ln \left[\frac{1}{k_1} \left(1 - \frac{n}{\mathrm{SNR}(B)}\right)^2 \right] . \tag{4.34}$$

One general outcome is that, for a fixed SNR(B), OVs with higher ℓ values allow the detection of smaller off-axis displacements. This effect is more significant at low SNR regimes, when the maximum measurable R is small and the curves in Fig. 4.5 are more spatially separated. As SNR(B) increases, the advantage obtained by using high values of the topological charge becomes negligible. In fact, if we assume SNR(B) above 10, we might reveal off-axis displacements lesser that $0.1a$ for all ℓ values. Instead, considering the lowest acceptable value SNR(B) = 3 for signal detection, we can detect off-axis displacements of $\sim 0.3a$ for $\ell = 1$ at the 1σ confidence level.

Chapter 5

Optical vortex coronagraphy

5.1 Introduction

The invention of coronagraphy dates back to 1939, when the first *coronagraph* was conceived by Lyot [121] with the specific purpose to suppress the light emitted by the disk of the Sun and observe the Solar corona. Nowadays, with the term *coronagraph* we intend a generic optical device which allows to achieve high contrast with a single aperture telescope, regardless of the connection with the original problem of observing the Solar corona. A practical definition that encompasses the current usage of coronagraphs refers to an optical system that rejects the stellar light from a predefined area of the focal plane of a telescope in order to reduce spurious effects produced by the associated speckle and photon shot noises [122].

Coronagraphic devices are currently being used to directly detect faint sources around bright astrophysical objects like stars or active galactic nuclei. However, one of the primary goals of the future generation of coronagraphs is to obtain for the first time images of terrestrial extrasolar planets. The direct imaging of planets around a bright star is, generally, a challenging task because of the very high contrast ratio and the very small angular separation of the sources. In the case of giant extrasolar planets, a typical contrast ratio of $\sim 10^{-7}$ is expected in the near infrared, while Earth-like planets are about 3–4 orders magnitudes fainter, depending on the wavelength range (6×10^{-9} the visible and 7×10^{-6} in the infrared [99]).

The first direct detection of a faint sub-stellar companion around the star GQ Lup was successfully achieved in 2005 with K-band coronagraphic observations carried out using the NACO instrument [123] mounted at the VLT-UT4 telescope [124]. Subsequently, coronagraphic techniques have allowed the direct imaging of a handful of sub-stellar companions, mainly brown dwarfs, around other stars [125, 126, 127, 128]. However, the most striking result is the recent detection of a system of three planets orbiting the star HR 8799 achieved with high-contrast Keck and Gemini observations [129].

5.2 Coronagraphic concepts

The recent years have seen the development of several coronagraphic concepts characterized by different methods of rejection of the stellar light. This can be achieved essentially in two ways:

- by inserting a stop in the image plane;
- by inserting a stop in the exit pupil plane.

The image stop solutions, like the original Lyot coronagraph, are generally one-stage Fourier spatial filters, while those including the pupil stop shares the property of having two (or in some cases more) stages of Fourier spatial filtering, one in the first image plane and one in the exit pupil plane.

The performance of a coronagraphic design can be quantitatively described in terms of the useful throughput, that is the maximum fraction of the companion light collected by the telescope that can be separated from starlight, and the inner working angle (IWA), commonly scaled to λ/D, defined as the minimal angular distance at which the throughput of the faint object is half of the maximal throughput [130].

The optical setups of all the current coronagraphic concepts can be represented using a general model that describes the propagation of the wavefront between four consecutive planes [131]. This general model is sketched in Fig. 5.1, where the four planes are denoted by A, B, C and D. A represents the entrance

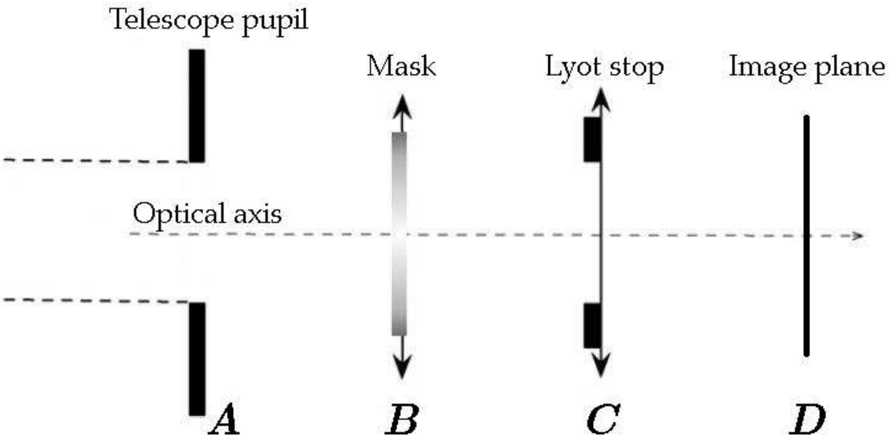

Figure 5.1 – General model of a coronagraph.

pupil, usually identified with the aperture of the telescope, B is the focal plane of the telescope where the coronagraphic mask is inserted, C is the exit pupil where the Lyot stop is located and D is the final focal plane where we observe the coronagraphic image. In each plane we define a complex transfer function of the position vector $\vec{r} = (r, \theta)$ with respect to the optical axis: the aperture function of the telescope $A(\vec{r})$, the coronagraphic mask transmission function $T(\vec{r}) = 1 - M(\vec{r})$ and the the Lyot stop transmission function $L_S(\vec{r})$. The exact mathematical expressions of $A(\vec{r})$, $T(\vec{r})$ and $L_S(\vec{r})$ depends on the specific task required for the corresponding optical element.

Consider an optical wave with a complex amplitude $\Psi(\vec{r})$ just before the aperture plane of the telescope. We assume, for simplicity, that the wavefront is sufficiently close to perfect (unaberrated), as it can be obtained in space instruments or by using a separate wavefront correction system in ground-based telescopes. We make also the usual approximation of paraxial optics and neglect the quadratic phase terms associated with the propagation of the waves. This allows to easily explain the propagation of the wavefront between two consecutive planes in terms of classical Fourier optics [50]. Thus, the wavefront in the planes

A, B, C and D can be calculated as [131]:

$$\Psi_A(\vec{r}) = \Psi(\vec{r})A(\vec{r}) \tag{5.1}$$

$$\Psi_B(\vec{r}) = \hat{\Psi}_A(\vec{r})\,T(\vec{r}) = \hat{\Psi}_A(\vec{r}) - M(\vec{r})\,\hat{\Psi}_A(\vec{r}) \tag{5.2}$$

$$\Psi_C(\vec{r}) = \hat{\Psi}_B(\vec{r})\,L_S(\vec{r}) = \Psi_A(\vec{r}) - \left[\Psi_A(\vec{r}) * \hat{M}(\vec{r})\right]\,L_S(\vec{r}) \tag{5.3}$$

$$\Psi_D(\vec{r}) = \hat{\Psi}_C(\vec{r}) = \hat{\Psi}_A(\vec{r}) - \left[\hat{\Psi}_A(\vec{r})\,M(\vec{r})\right] * \hat{L}_S(\vec{r})\ , \tag{5.4}$$

where $\hat{f}$ is the Fourier transform of a function f and $*$ is the convolution operator defined by

$$(f * g)(x) = \int f(y)\,g(x-y)\,\mathrm{d}y = \int f(x-y)\,g(y)\,\mathrm{d}y\ . \tag{5.5}$$

The action of a coronagraph appears in Eq. 5.3: the first term coincides with the wave entering the telescope pupil, while the second term corresponds to the wave diffracted by the phase mask. To obtain an efficient nulling effect, the second term must be canceled in the C plane by properly choosing the aperture, mask and Lyot stop functions.

A coronagraph correctly designed for imaging faint components around a host star can operate one of these two techniques:

1. concentrate the light of the on-axis star, thus reducing the diffracted light of off-axis sources;
2. reject the light of the on-axis star without altering that of off-axis sources.

The first case corresponds to the *apodization* technique, that can be achieved by using particular models of the aperture function $A(\vec{r})$ (see e.g. [132]). In the second case, instead, the two terms in Eq. 5.3 must balance each other (destructive interference) for the on-axis star, while only the second term must vanish for the off-axis source. This result can be obtained by using coronagraphic masks having specific transmission functions that allow to modulate either the amplitude or the phase of the wavefront. Generally, phase masks are preferable with respect to amplitude masks. In fact, an amplitude mask produces an opaque zone that occults a significant fraction of the central field of view and, thus, all the sources located very close to the on-axis bright object. At the present time, the following coronagraphic solutions containing phase mask have been developed:

- the (original) *phase mask coronagraph* of Roddier & Roddier [133] based on a circular π-shifting focal plane mask;
- the *four quadrant phase mask coronagraph* [134] based on a focal plane mask that shifts two out of four quadrants of the image by π;
- the *phase knife coronagraph* [135] based on a π-shifting screen;
- the *annular groove phase mask coronagraph* [99] based on a circular sub-wavelength grating.
- the *optical vortex coronagraph* (OVC) [136] based on an SPP.

The last two solutions share the property of exploiting the nulling effect provided by the dark core of an OV.

The OVC is one of the two valuable applications of OVs in astronomy mentioned in Sect. 1.5. In the next Sections I will review the high-contrast properties of the OVC and present additional results obtained from our numerical and experimental studies.

5.3 The optical vortex coronagraph

The OVC is one of the very few coronagraphic solutions that might yield performances reasonably close to the limit imposed by fundamental physics on the direct imaging of extrasolar terrestrial planets [130]. The optical setup of an OVC (see Fig. 5.2) includes an SPP designed to produce an ℓ-charged OV at a specific wavelength λ. The light coming from an object (either on-axis, O_1, or off-axis, O_2), is imaged by the telescope, L_1, having an aperture diameter D and a focal length f. The SPP is placed at the focal plane of L_1, corresponding to the B plane of Fig. 5.1. A collimating lens, L_2, re-images the entrance pupil of the telescope beyond the SPP on the Lyot stop plane plane (the exit pupil plane), where a circular diaphragm acts as a Lyot stop. The propagated wavefront is then focused by a camera lens, L_3, on the final image plane. In the framework of the general model described in Sect. 5.2, the aperture function $A(\vec{r})$ is, generally, that of an

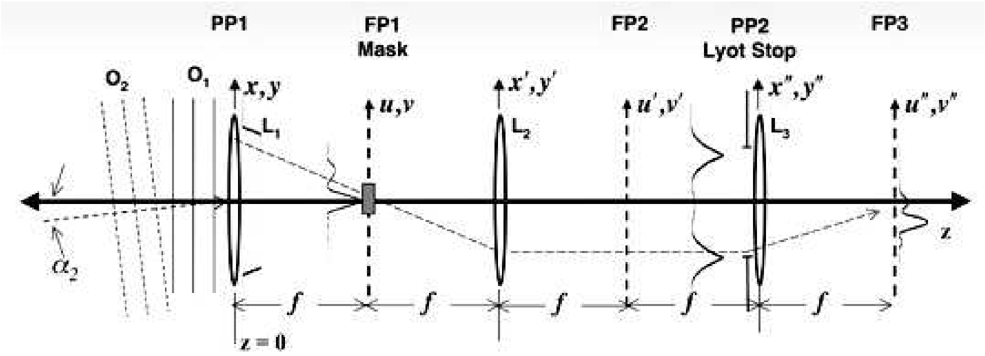

Figure 5.2 – Optical scheme of an OVC. Figure adapted from Ref. [136].

unobstructed telescope. The mask function $T(\vec{r})$ is expressed by Eq. 1.27, while the function $L_S(\vec{r})$ is that of an aperture.

Essentially, the focused light beam coming from a star is directed towards the center of an SPP, thus producing a symmetric annular-shaped diffraction pattern in the Lyot stop plane. Instead, the light beam of a very close source will be focused in a position different form that of the optical singularity of the SPP and, thus, produce an asymmetric diffraction pattern, with a partial filling of the central dark region. As reminded in Sect. 3.2, only OVs produced with Airy patterns possess large central dark regions with null intensity. Therefore, high-contrast OV coronagraphy can be achieved only with a diffraction-limited telescope. An additional requirement is that the topological charge ℓ imposed by the SPP to the on-axis OV must have an even value ($\ell = 2k$, with $k \in \mathbb{N}$). In fact, only in this case the light of the on-axis stellar source will be totally spread outside the exit pupil [99], thus being blocked by the Lyot stop. Fig. 5.3 shows numerically simulated radial profiles of the diffraction images produced at the exit pupil plane by a monochromatic on-axis point source passing through an SPP with $\ell = 1, 2, 3, 4$. In these examples, the radius of the exit pupil has been set to 50 pixels. We can see that only the profiles obtained with even topological charges have zero intensity inside the exit pupil, while the other profiles extends well within it.

The theoretical performances of an OVC were investigated by Palacios & Swartzlander [137]. In this work, they numerically simulated the coronagraphic images produced with a diffraction-limited telescope. The major result is that a

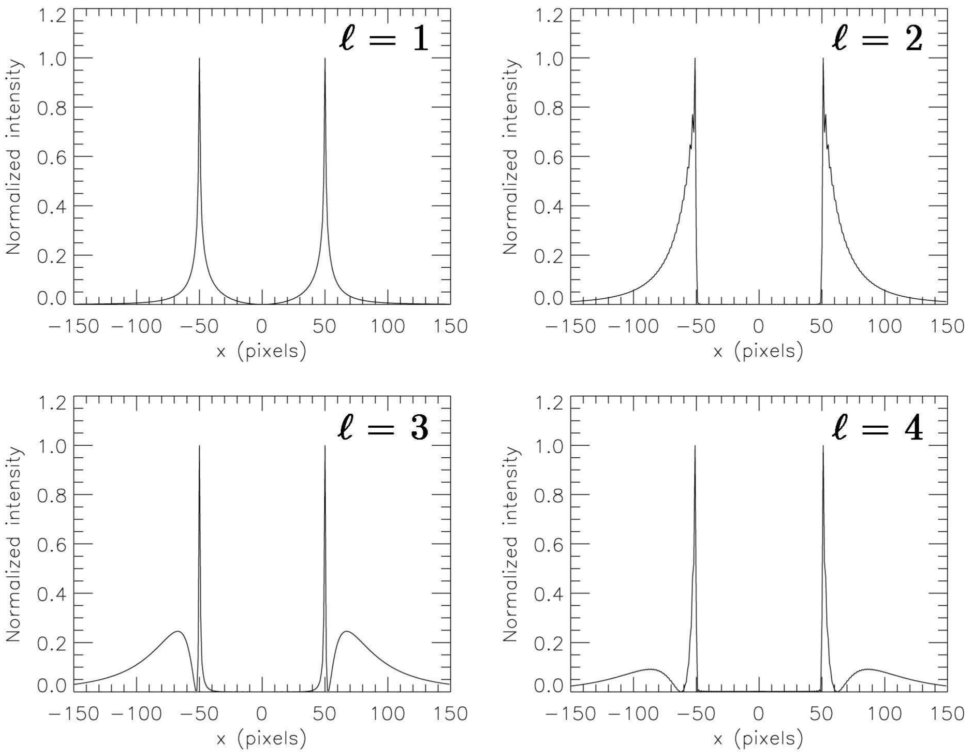

Figure 5.3 – Simulated profiles of the intensity distributions produced at the Lyot stop plane of an OVC for different values of the topological charge.

contrast ratio of 10^{-10} may be generally obtained at an IWA of $4\,\lambda/D$ using an OVC with an even-valued ℓ and reducing the Lyot stop diameter to 0.8 times the diameter of the exit pupil. The same contrast level can be achieved also at an IWA of $2\,\lambda/D$ only in the case $\ell \geq 4$ and assuming the same Lyot stop aperture. A further result is that the throughput of off-axis objects, defined as the quantity of light transmitted through the Lyot stop, decreases as ℓ increases.

The high-contrast performances provided by an OVC exhibit also a very small sensitivity to low-order aberrations. This has been demonstrated assuming a transmission function of the telescope pupil $A(\vec{r}) = P(r)\,\mathrm{e}^{\mathrm{i}\,\Phi(\vec{r})}$ [138], where the amplitude factor depends only on the radial coordinate and $|\Phi(\vec{r})| \ll 1$. The propagated wavefront just before the exit pupil plane is thus:

$$\psi_{\mathrm{EP}}(\vec{r}) \propto \left(-\frac{1}{2\pi}\right)^{\ell} \frac{\partial^{\ell}}{\partial r^{\ell}} \left[P(r)\left(1+\sum_{m=0}^{\infty}\frac{\mathrm{i}^{m}}{m!}\Phi^{m}(\vec{r})\right)\right] . \tag{5.6}$$

The coronagraphic leakage due to the first term ($m = 1$) of this series expansion is proportional to the m-th order derivative of the phase aberration and, thus, vanishes for any phase aberration showing a power-law radial dependence with an exponent lesser than m. Therefore, an OVC presents an m-th order aberration sensitivity in amplitude and a $2m$-th sensitivity in intensity.

The performances expected from an *ideal* OVC are remarkable. However, a *real* OVC suffers of some technical limitations. Firstly, the usable spectral band is severely reduced by the intrinsic monochromaticity of SPPs (see Sect. 1.4). In fact, the output beam produced by an non-monochromatic on-axis source contains a superposition of coaxial monochromatic OVs. According to Eq. 1.26, the topological charges of these OVs will have non-integer values, with the exception of that produced at the operating wavelength of the SPP. Therefore, the intensity distribution produced by the output beam will be the superposition of many asymmetric monochromatic patterns, with the result of a partial filling of the central dark region. To obtain a reasonably high contrast, ℓ has not to vary more than $\sim 10^{-3}$ for an $\ell = 2$ SPP. This means that the available spectral band is ~ 1 nm for visible wavelengths. A solution to this problem was found by Swartzlander [139], who designed an achromatic SPP composed by two adjacent optical elements made with different materials. However, achromaticity was predicted only

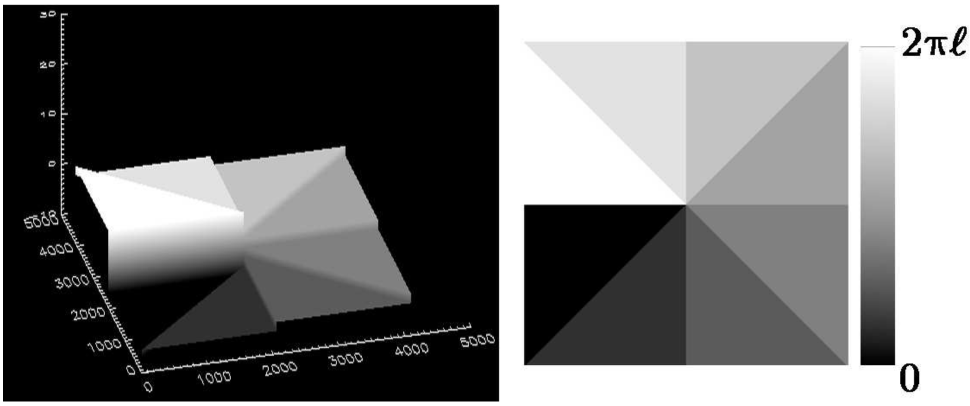

Figure 5.4 – *Left*: simulated 3D image of an stepped SPP with 8 levels. *Right*: the corresponding phase retard.

for a limited bandwidth (∼ 100 nm) in the visible.

Another limitation concerns the techniques used to produce SPPs. With current nanotechnologies, it is very difficult to produce SPPs with smoothly-varying helical surfaces. Therefore, the ideal SPP surface is usually approximated by a spiral staircase pattern composed of N discrete steps. As an example, Fig. 5.4 shows a stepped SPP with 8 levels. The transmission function of a stepped SPP having a central optical singularity with strength ℓ is

$$T(r,\theta) = \exp\left(\mathrm{i}\left\lfloor\frac{N\theta}{2\pi}\right\rfloor\Delta\phi\right) , \tag{5.7}$$

where $\Delta\phi = 2\pi\ell/(N-1)$ is the constant phase jump between two consecutive steps and $\lfloor z\rfloor$ is floor function that maps a real number z to the largest integer not greater than z. A light beam intersecting a stepped SPP exactly on-axis still produces a vortex beam with a screw wavefront. However, additional phase rips will be produced by each step of the SPP. These rips results in visible radial distortions of the far-field diffraction pattern, depending on the number N of steps used to approximate the ideal SPP spiral surface.

To better understand the effect of the discretization, we have numerically simulated the far-field patterns produced by a Gaussian beam intersecting on-axis $\ell = 2$ stepped SPPs with a different number of levels. For small values of N, we find that the SPP causes the expected $\ell = 2$ OV to split into two single-charged OVs. This effect results in the appearance of two dark regions, like those clearly

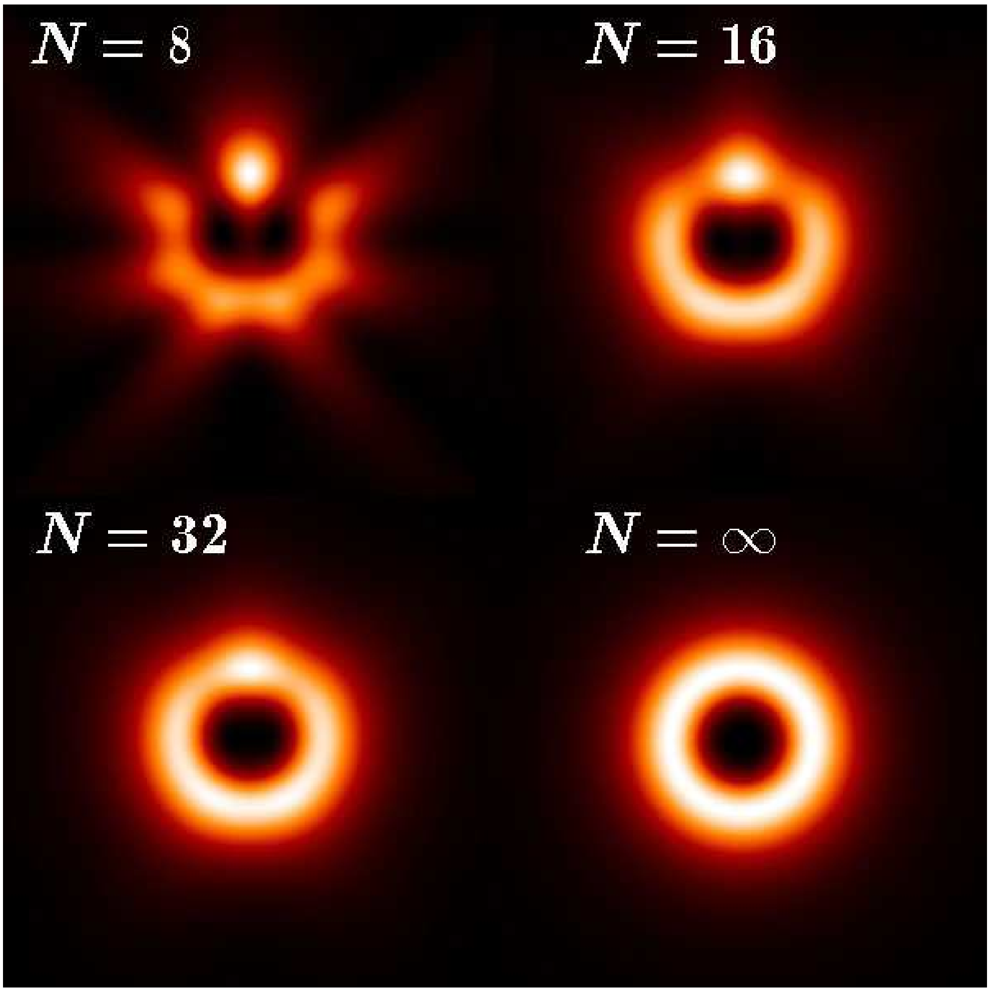

Figure 5.5 – OV patterns produced by a Gaussian beam intersecting on-axis $\ell = 2$ SPPs with $N = 8, 16, 32, \infty$ levels.

visible in the simulated image obtained with an 8-level SPP reported in Fig. 5.5. However, our simulations indicate the intensity distributions of the observed OVs can be reasonably approximated to those obtained with a continuous SPP when $N \geq 64$, at least for Gaussian input beams. Guo *et al.* [140] demonstrated that, in the case of stepped SPPs, the output beam contains also additional vortex components having topological charges $\ell' = \ell + kN$, where $k \in \mathbb{Z}$. The vortex beam can be expanded in Fourier series:

$$u(r,\theta) = \sum_{\ell'=-\infty}^{+\infty} c_{\ell'}\, \mathrm{e}^{\mathrm{i}\ell'\theta} \,, \tag{5.8}$$

where the relative weight of each component is

$$|c_{\ell'}|^2 = \frac{\sin^2(\ell'/N)}{(\ell'/N)^2} \,. \tag{5.9}$$

This result can be intuitively interpreted as the angular version of the conventional diffraction from multiple slits. In this case, the angular discretization of the SPP produces a so-called *angular diffraction* [141].

Despite all these technical limitations, Lee *et al.* [142] succeeded in demonstrating the low-contrast application of an OVC with a laboratory experiment. Indeed, OV coronagraphy would give its best performances with instruments placed outside the atmosphere. However, Jenkins [100] analytically demonstrated that an OVC can give good performances also in ground-based telescopes operating with a partial correction of the atmospheric turbulence. The feasibility of ground-based $\ell = 2$ OV coronagraphy has been subsequently demonstrated by Swartzlander *et al.* [143] using a small telescope equipped with a simple adaptive optics module. In this experiment, the aperture of the telescope was reduced with a diaphragm to 25 mm in order to have only the tip/tilp aberration.

5.4 Studies of the optical vortex coronagraph

On the basis of the results of previous work, we are currently projecting an OVC based on a stepped SPP designed to produce $\ell = 2$ OVs at visible wavelengths. In the next Sections I will show the results of our numerical simulations and present the experimental procedure used to test stepped SPPs.

5.4.1 Numerical simulations

To better define the expected performances of our OVC, we performed numerical simulations following the procedure explained in Appendix A.3. Firstly, we simulated a diffraction-limited observation of two close point-like sources using an $\ell = 2$ OVC. The SPP surface was considered as perfectly helicoidal, i.e. with no discretization, and the Lyot stop diameter was set at 0.8 times the exit pupil diameter. The on-axis sources, A, had unity intensity, while that of the of-axis source, B, was set to 10^{-8}. Such a contrast ratio is essentially that expected in the visible region from a Jovian planet (B source) and its host star (A source). Fig. 5.6 shows the coronagraphic images obtained for different separations of the two sources, namely $0.5\,\lambda/D$, $1\,\lambda/D$ and $2\,\lambda/D$. These plots confirm the high-contrast capability of an OVC assessed by Palacios & Swartzlander [137]. Furthermore, we can see that the intensity of the A source is always fainted by ~ 10 orders of magnitude, thus allowing the clear detection of B source at a separation of just $0.5\,\lambda/D$.

We then investigated how the use of stepped SPPs, like those currently obtainable with conventional nanolithographic techniques (see Sect. 5.3), affects the performances of an OVC. To do this, we numerically evaluated the quantity of light of an on-axis source that is transmitted through the Lyot stop having a diameter equal to 0.8 times the exit pupil diameter. The SPPs, designed to produce $\ell = 2$ at 550 nm, had $N = 8, 16, 32, 64, 128$ discrete levels. The fraction of light transmitted through the Lyot stop has been calculated in the 450–700 nm wavelength range, for all the stepped SPPs considered. The results obtained using SPPs with 8, 16 and 32 levels are shown in Fig. 5.7, together with those obtained with a continuous SPP ($N = \infty$). In all cases, the transmitted fraction of light is lesser than $\sim 10^{-2}$ in the whole wavelength range. However, we find that the minima of the curves shown in Fig. 5.7 increases as N decreases, being zero only in the case of a continuous SPP. Moreover, these minima are not always located at 550 nm. Instead, we see that the *optimal* wavelength λ_N, i.e. the wavelength at which the transmitted fraction of light is minimum, changes with the number

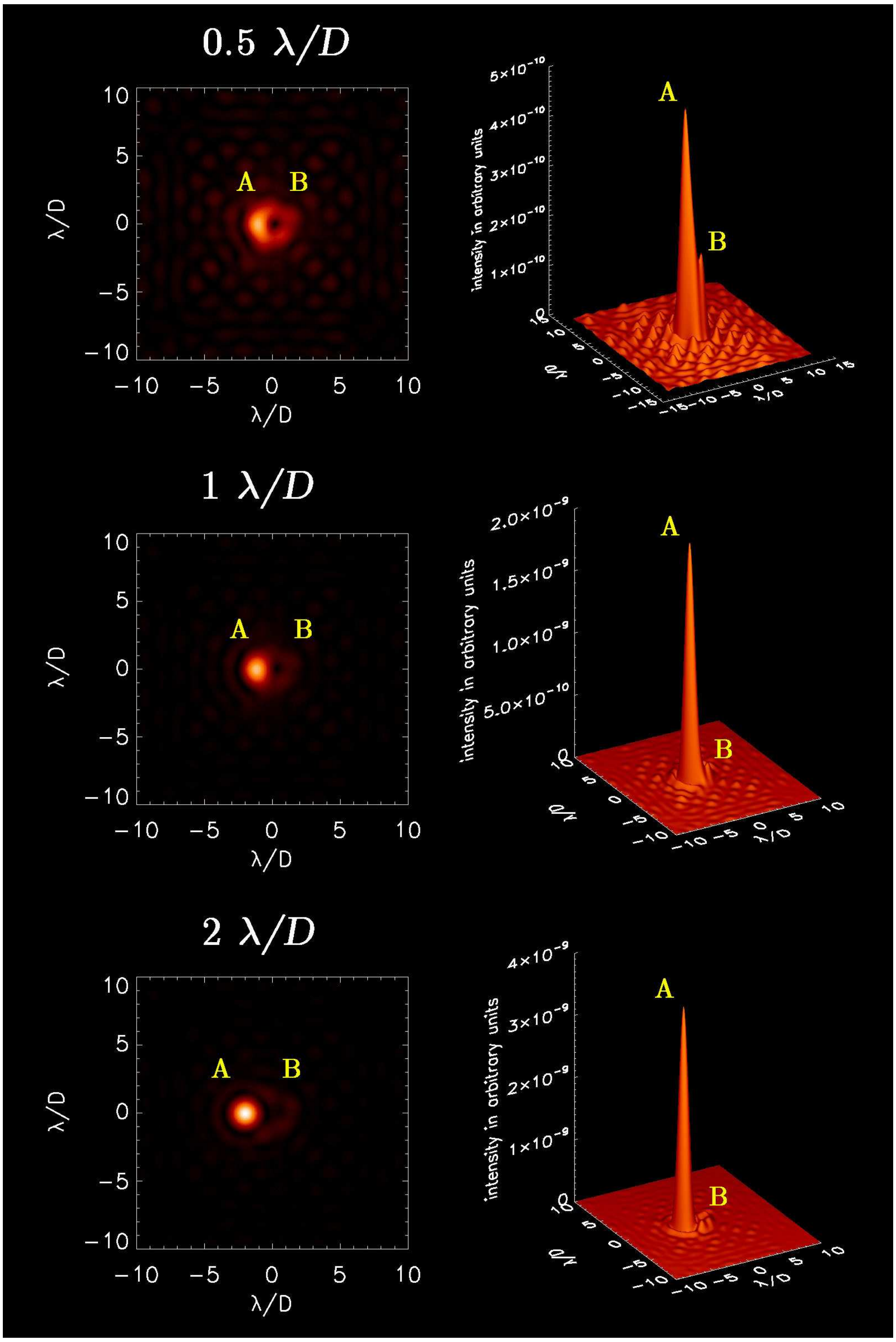

Figure 5.6 – Numerical simulations of coronagraphic images of two close point source obtained with an OVC (*left*), together with the corresponding surface plots (*right*). The contrast ratio between the two sources, indicated by A and B, is 10^{-8}. The A source is always on-axis (origin of the coordinate system), while the fainter B source is shifted off-axis by $0.5\,\lambda/D$ (*top*), $1\,\lambda/D$ (*middle*) and $2\,\lambda/D$ (*bottom*).

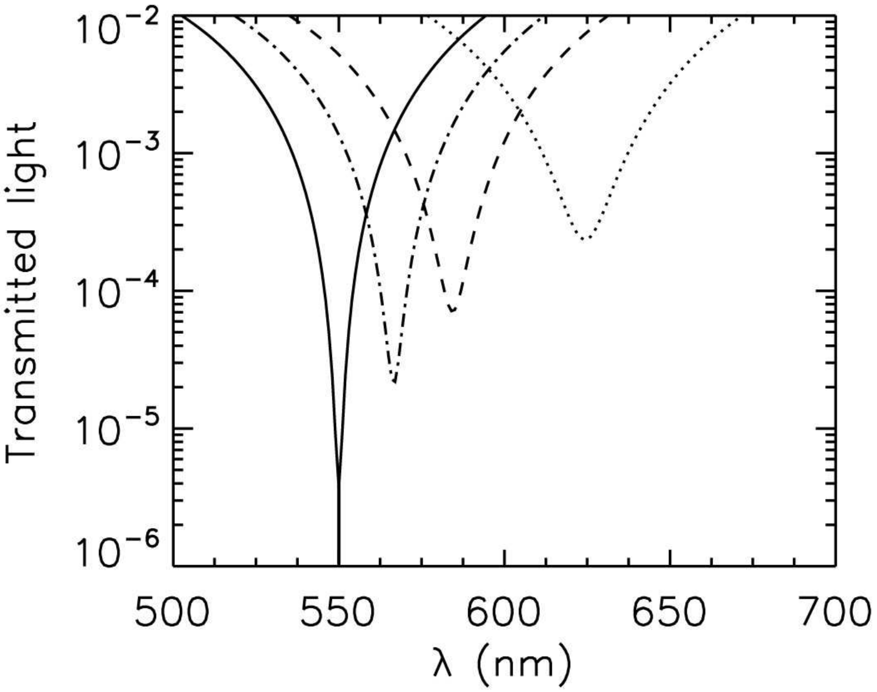

Figure 5.7 – Fraction of the light of an on-axis star transmitted through the Lyot stop of an OVC plotted as a function of the wavelength. The OVC contains an SPP designed to produce an $\ell = 2$ OV at 550 nm. The four curves represent the numerical results obtained with a continuous SPP (solid line), as well as with a stepped SPP having 8 (dotted line), 16 (dashed line) and 32 (dash-dotted line) levels.

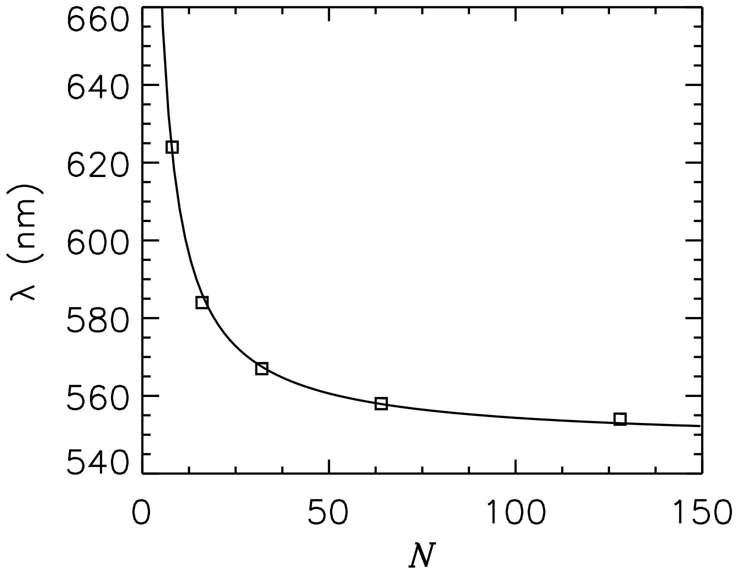

Figure 5.8 – The optimal wavelength of an OVC containing a stepped SPP vs. the number of discrete levels of the SPP. Open squares mark the results of numerical simulations, while the solid line represents the best-fit curve to these data (Eq. 5.10).

of discrete levels of the SPP approximately following a power-law relation:

$$\lambda_N = \lambda_\infty \left(1 + \frac{1}{N^\alpha}\right) , \tag{5.10}$$

where $\lambda_\infty = 550$ nm is the optimal wavelength for the continuous ($N = \infty$) SPP used in our numerical simulations (see Fig. 5.8). A non-linear least square fit to the obtained data gives $\alpha = 0.98 \pm 0.01$, where the uncertainty is at the 1σ confidence level.

These results demonstrate that, using a stepped SPPs, it is always impossible to totally reject the light of an on-axis star outside the exit pupil. Unless the number of steps is high ($N \gtrsim 200$), this implies that part of that light passes through the Lyot stop, with a drastic reduction of the achievable contrast. We can interpret these drawback as the result of the appearance of additional OVs having topological charges different from ℓ [140].

N	h (nm)
8	320
16	149
32	72
64	36
$\vdots$	$\vdots$
512	4.4

Table 5.1 – Calculated heights of the levels of a stepped SPP in PMMA designed to produce an $\ell = 2$ OV at 550 nm. N is the number of discrete levels.

5.4.2 Laboratory tests

The current status of our OVC project concerns the experimental characterization of stepped SPPs nanofabricated at the TASC–LILIT laboratories in Trieste [1].

We decided to use PMMA (polymethyl methacrylate) as the material on which etch our SPPs. PMMA is a versatile polymer that is often used as an alternative to glass because of the similar optical properties, easy handling and processing and low cost. Furthermore, PMMA is most commonly used as a high resolution positive resist for electron beam etching. PMMA is, thus, very suitable for optical applications in the visible region, where it has a transmittivity as high as $\sim 90\%$. The actual transmittivity of our PMMA plates was measured in the range 450–950 nm by using the monochromator of the Laboratory of Optics of the Astronomical Observatory of Padova. The results of our test, shown in Fig. 5.9, confirm the expected high transmittivity in the 450–600 nm wavelength range, with the exception of the 700–900 nm region where it is slightly smaller ($\sim 85\%$).

The manufacturer of our PMMA plates reports an index of refraction $n = 1.491$ at 550 nm. Therefore, according to Eq. 1.27, an SPP in PMMA designed to produce an $\ell = 2$ OV at 550 nm must have a central thickness jump $h_s = 2.245\,\mu$m. In the case of a stepped SPP, this implies that the height h of each step

---

[1] The laboratory for interdisciplinary lithography (LILIT) is devoted to the fabrication of structures with spatial resolution ranging from μm to few nanometers (see `http://www.tasc-infm.it/` for further information).

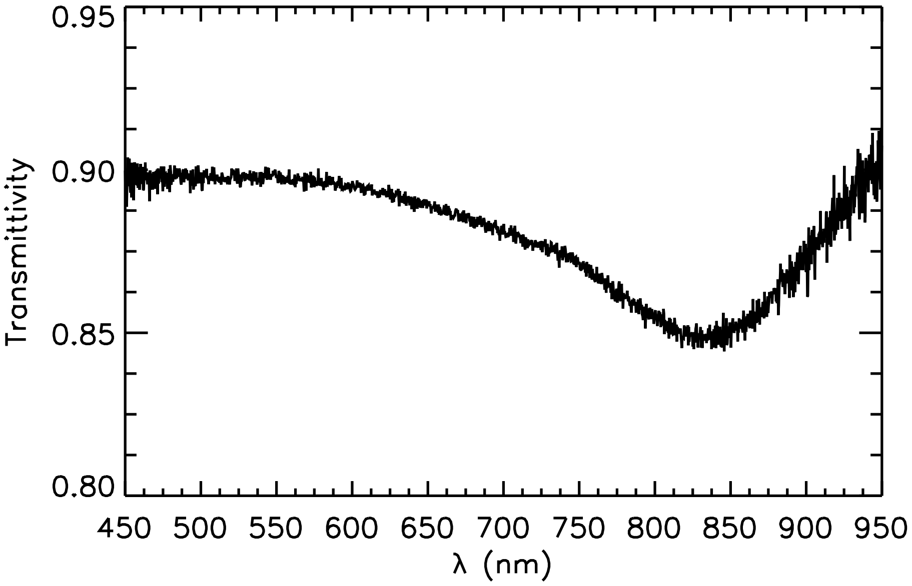

Figure 5.9 – Measured transmittivity of a PMMA plate in the 450–950 nm wavelength range.

must be in the range 10–100 nm (see Table 5.1). In order to obtain SPPs useful for OV coronagraphy, the etching process must also ensure the planarity of the levels with an extremely high precision. In particular, the uncertainty associated to the total thickness must not exceed $\sim 10^{-3} h_s$. This is the reason why we decided to use electron beam nanolithographic techniques to manufacture our SPPs.

We were provided with a number of stepped SPPs having N ranging from 8 to 512. These optical components were etched on PMMA plates with a thickness of 1 mm inside a circular region having a diameter of 1 mm. As an example, Fig. 5.10 shows the SEM image of one of the SPPs with 64 discrete levels. Some of the 512–levels SPPs were also manufactured on a PMMA layer deposited on a BK7 glass substrate, in order to prevent mechanical bending. With the goal of selecting the best SPPs for OV coronagraphy, their quality was tested at the Laboratory of Optics of the Department of Astronomy (University of Padova) using two methods:

1. by analyzing the interferogram produced with a Mach-Zehnder interferometer;

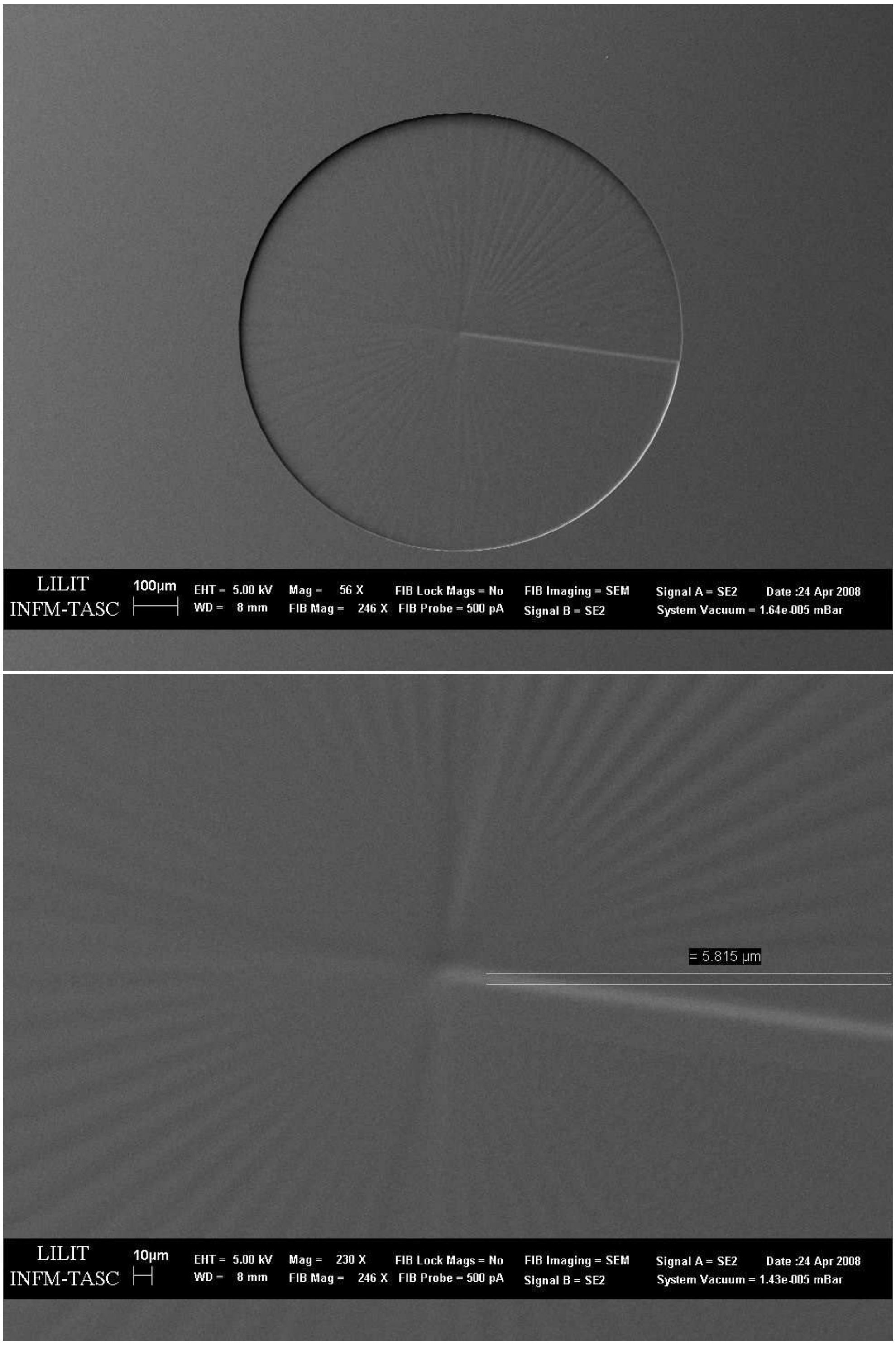

Figure 5.10 – SEM images of one of the stepped SPPs with 64 level. The lower figure is a magnification of the central region of the SPP.

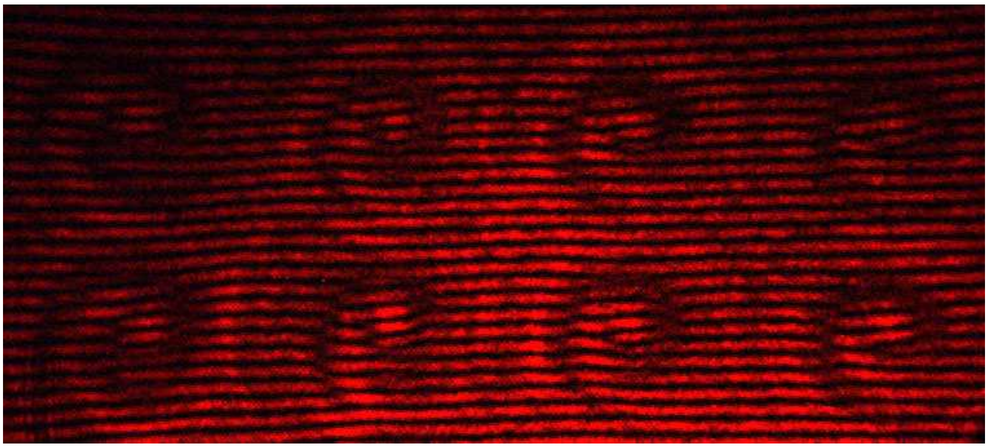

Figure 5.11 – Mach-Zehnder interferogram produced with a PMMA plate containing 8 SPPs with different total thickness variations h_s.

2. by comparing the experimental far-field diffraction pattern with numerical simulations.

In both cases, we used a He-Ne laser at 632.8 nm as the source of coherent light.

In the first case, the PMMA plates containing the SPPs were placed in one arm of a Mach-Zehnder interferometer. The interference pattern produced by a plane wave intersecting the SPP and a reference plane wave is described by Eq. 1.22. Fig. 5.11 shows the interferogram obtained by using 8 SPPs with 512 levels etched in the same PMMA plate. These SPPs have slightly different central thickness jumps h_s, ranging from 1.4 to 3.0 μm. As a result, OVs with ℓ in the range 1.1–2.3 are expected to be produced at the operating wavelength of the laser. We can see that all the 8 SPPs produced their own OV in the incident wave, as revealed by the corresponding fork-like interferograms. Note that the number of central dislocations of each fork-like interferogram is exactly equal to $\lfloor \ell \rfloor$, as expected. The spiral structures visible in Fig. 5.11 are additional interference pattern produced by the non perfectly planar reference wave.

The second more qualitative test consisted in the observation of the far-field diffraction patterns produced by the He-Ne laser intersecting on-axis the SPPs. The laser was spatially filtered to obtain a beam close to a fundamental Gaussian transverse TEM_{00} mode [36]. The OV patterns imaged by using a CCD camera were subsequently compared with those obtained with numerical simulations (see Appendix A.2), assuming a laser beam with a perfect Gaussian profile. Examples of the experimental and simulated patterns are reported in Fig. 5.12 for three different stepped SPPs. All the observed patterns contain spots with zero intensity in correspondence of the position of phase singularities. In general, the experimental images are in quite good agreement with numerical simulations.

These tests indicate that the manufacturing precision achievable by using electron beam lithography is very good. However, at the current stage, the quality of our SPPs would not be enough high for coronagraphy. A development of the nanolithographic techniques is strongly required, in particular to obtain a much more better planarity of the discrete levels.

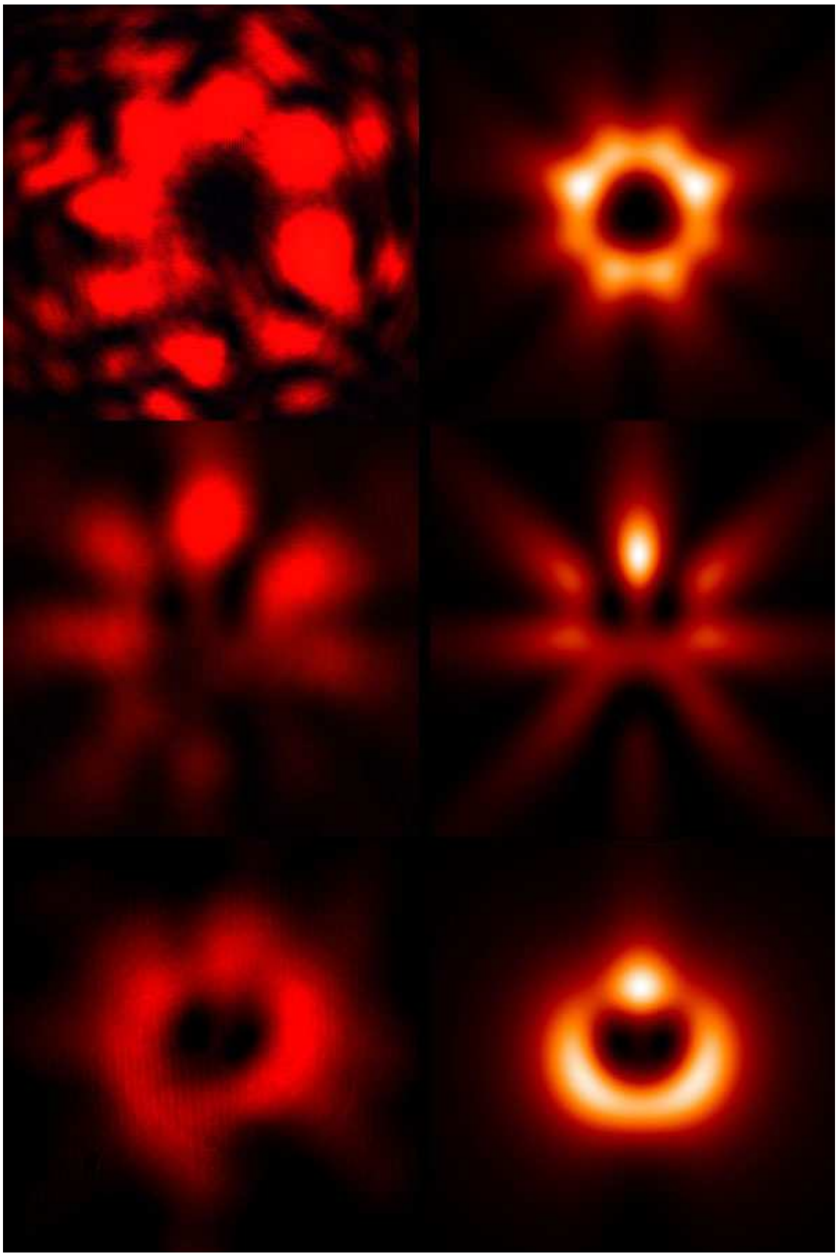

Figure 5.12 – Experimental far-field OV pattern produced by a Gaussian laser beam at $\lambda = 632.8$ nm intersecting different SPPs (*left*), together with the corresponding numerical simulations (*right*). *Top row*: 8 level SPP, $\ell = 2$ at 632.8 nm; *central row*: 8 level SPP, $\ell = 2$ at 550 nm; *bottom row*: 512 level SPP (BK7 substrate), $\ell = 2$ at 550 nm.

Chapter 6

Conclusions

In this Thesis I have presented the results of experimental and theoretical investigations on some properties of OVs that could find promising applications in observational astronomy. In particular, this work is mainly aimed at developing and testing new methods to improve the performances of optical systems by using FHs or SPPs that introduce a phase vorticity in incident light beams.

The possibility of overcoming the Rayleigh separability limit by using an $\ell = 1$ FH was discussed in Chapter 2. The superposed OVs patterns produced beyond a FH by two equally-luminous light beams having an Airy intensity distribution were studied in a laboratory experiment. One of the two beams was kept centered with the optical singularity of the FH, while the second beam could be displaced in off-axis positions. As the second beam was shifted away from the central position, an OV with a non-integer value of the topological charge was produced, with an asymmetric intensity profile. As a result, some asymmetry was observed also in the intensity distribution of the two superposed far-field diffraction patterns. Both our numerical simulations and experiments revealed that the asymmetry of the superposed images becomes significantly detectable also for separations of the two sources well below the classical Rayleigh limit. This result was achieved both with monochromatic and white light beams. For this reason, we proposed a new separability criterion based on the analysis of the profile of the superposed OV patterns to resolve two point sources at angular distances one order of magnitude below the diffraction limit. Our method might have interesting applications in several techniques of applied optics, as well as in observational astronomy where it could be used to improve the resolving power of a diffraction-limited telescope.

In addition to our laboratory tests, we performed the first astronomical experiment in which OVs were generated in starlight beams, as described in Chapter 3. To this aim, we have placed an $\ell = 1$ FH near the F/16 Cassegrain focus of the Asiago 122 cm telescope. We observed the multiple system α Her and the single star α Boo. Since the observations were carried out under mediocre seeing conditions ($3'' - 3.8''$), we used the Lucky Imaging approach which is a low-cost method alternative to adaptive optics. We were able to detect the non-monochromatic OV images produced by the two main components of α Her, as well as the annular-shaped narrow-band OV image produced by α Boo. In the first case, the intensity profile of the non-monochromatic OV produced by the off-axis component α Her B presented two different peaks. Their intensity ratio was consistent, within the errors, with numerical simulations. In the second case, the intensity profile of the narrow-band OV pattern was much better reproduced by numerical simulations, with the exception of a partial filling of the central dark region that was most likely due to some residual chromaticity and the lack of light coherence produced by the atmospheric turbulence. These results provided useful indications on the effects of the atmospheric turbulence in ground-based applications of the OV techniques. Furthermore, our numerical simulations revealed that the far-field OV pattern produced with an $\ell = 1$ PMD is extremely sensitive to off-axis displacements of the input beam, in particular when it has a Gaussian amplitude distribution.

The sensitivity of OVs to misalignments of the input beam is discussed in detail in Chapter 4. As a first step, I have obtained the exact mathematical expression of the intensity distribution of the diffraction pattern produced, under Fraunhofer conditions, by a Gaussian light beam crossing an SPP. The transverse field amplitude of the output beam was analytically expressed in terms of Kummer functions. As a result, an input beam perfectly aligned with the central singularity of the SPP is shown to produce a perfectly symmetric annular intensity distribution. Instead, any off-axis displacement results in an asymmetry of the diffraction pattern. Our numerical simulations revealed that the ratio R between the intensities of the peaks along the direction of maximum asymmetry changes exponentially with the off-axis displacement of the input beam, for any integer value of the topological charge in the range $0, \ldots, 10$. The effects of the SNR associated to the highest peak on the sensitivity of the ratio R to very small misalignments of the input beam were also analyzed. It is demonstrated that higher values of the topological charge ℓ generally provide better resolutions, especially for low SNRs. This result suggests that OVs can be used to perform astrometry of single stars with ground-based telescopes. With good seeing conditions or adaptive optics devices, the astrometric precision achievable with OVs could be competitive to standard PSF astrometry. Moreover, a PMD placed within an adaptive optics system could be used to improve the tip/tilt correction of the wavefront for a small field of view. In fact, it might be possible to correct the isokinetic patch which size, like the isoplanatic field, strongly depends on the seeing and the wavelength.

Finally, Chapter 5 was dedicated to the application of OVs in astronomical coronagraphy, emphasizing the OVC project that we are currently developing. Our numerical simulations confirmed that the nulling property of the dark core of an OV produced with a perfect SPP offers the possibility to perform high-contrast coronagraphy when even-valued topological charges are used. Actually, we predict contrast ratios as high as $\sim 10^{-10}$ also at IWAs below $1\,\lambda/D$. However, we have found that the use of SPPs with a discretized surface prevents the total nulling of the light of the on-axis star within the exit pupil, unless the number of steps of the SPP is larger than about 200. In addition, we demonstrated that the use of these kind of SPPs changes the wavelength at which to the rejection of stellar light is maximum. We conclude that the structural characteristics of these PMDs unavoidably reduce the coronagraphic performances achievable with OVs. The quality of SPPs is then of crucial importance to fully exploit the theoretical properties of OVCs. However, the fabrication of these components requires an extremely precise manufacturing technology that is difficult to be achieved. For this reason, the current status of our OVC project is still restricted to the experimental characterization of stepped SPPs produced at the TASC–LILIT laboratories in Trieste by means of electron beam lithography.

In summary, even if the utilization of the properties of OVs in astronomy have just begun to be explored, especially at visible wavelengths, the instrumental techniques discussed in this Thesis present remarkable applications. Of particular interest could be their use with the next generation of ground- and space-based telescopes. We should also remind that any successful development of the proposed OV techniques will require a parallel development of the nanotechnologies used to produce high-quality PMDs. Nevertheless, the modern technology gives solid hopes to make practical use of new degree of information previously unknown to the astronomical community.

Appendix A

Appendices

A.1 Numerical simulations of vortex beams using Laguerre-Gaussian modes

Consider a beam with a field $u_{\text{in}}(r,\theta)$ that is axially symmetric about its propagation axis z. The field amplitude of the beam transmitted through a FH can be decomposed by using a basis of orthogonal L-G modes, following the procedure explained in Ref. [144]. This implies the projection of the field of the input beam just beyond the FH having a transmission function $T(r,\theta)$,

$$u_{\text{out}}(r,\theta) = T(r,\theta)\,u_{\text{in}}(r,\theta)\ , \tag{A.1}$$

onto a basis of L-G modes u_{PL} (Eq. 1.7) as:

$$u_{\text{out}}(r,\theta) = \sum_{L=-\infty}^{+\infty}\sum_{P=0}^{+\infty} a_{PL}\,u_{PL}(r,\theta)\ , \tag{A.2}$$

where P and L are the azimuthal and radial indices of each L-G mode, respectively.

The decomposition into L-G modes can be done also in the case of an off-axis input beam. Assuming a pure lateral displacement, we can make use of the invariance property of geometrical translations and consider, instead, a displacement of the FH along the opposite direction. This is necessary to simplify the following calculations. By indicating with (r_0,θ_0) the relative position of the optical singularity of the FH with respect to the symmetry axis of input beam, the complex weights a_{PL} in Eq. A.2 are given by the overlap integral

$$a_{PL}(r_0,\theta_0) = \int_0^{2\pi}\int_0^{r_{\mathrm{FH}}}\left[u_{0L}(r,\theta)\exp\left(-\mathrm{i}\ell\frac{2\pi}{\Lambda}r\cos\theta\right)\right]^* \\ \times T(r-r_0,\theta-\theta_0)\,u_{\mathrm{in}}(r,\theta)\,r\,\mathrm{d}r\,\mathrm{d}\theta\ , \quad \text{(A.3)}$$

where r_{FH} is the radius of the active area of the FH and * represents the complex conjugate operator.

In the experiment presented in Chapter 2 the PMD is an $\ell = 1$ FH blazed at the first diffraction order. Therefore, the transmission function $T(r,\theta)$ appearing in Eq. A.3 is that expressed by Eq. 1.24, where $\delta = 2\pi$. Instead, the field of the input beam has an Airy amplitude distribution:

$$u_{\mathrm{in}}(r) \propto \frac{\mathrm{J}_1(kar/d)}{kar/d}\ , \quad \text{(A.4)}$$

where $k = 2\pi/\lambda$ (λ is the wavelength), a is the aperture radius of the pinholes and d is the distance between the pinholes and the FH.

The calculation of the overlap integral (Eq. A.3) was performed by using a numerical code written in MATLAB. Without loss of generality, we assumed $\theta_0 = 0$. For each off-axis displacement r_0 expressed in unit of the Rayleigh limit δ_R (see Sect. 2.3), we obtained a set of a_{PL} with $L \in [-5,5]$ and $P \in [0,5]$. These limits were essentially imposed by the huge amount of time required by the numerical integration process. However, we have found that L-G modes having indices larger than this values contribute negligibly to the superposition in the range of off-axis displacement considered here. Fig. A.1 shows some of the coefficients $|a_{PL}|^2$ obtained for an on-axis beam ($r_0 = 0$), for a beam displaced off-axis at half the Rayleigh limit ($r_0 = 0.5\,\delta_R$) and for a beam displaced off-axis at the Rayleigh limit ($r_0 = \delta_R$). The final step consisted in the numerical calculation of the weighted superposition of the L-G mode amplitudes at the position of the observation plane, as expressed in Eq. A.2. The simulated diffraction pattern is then given by $\left|u_{\mathrm{out}}\right|^2$.

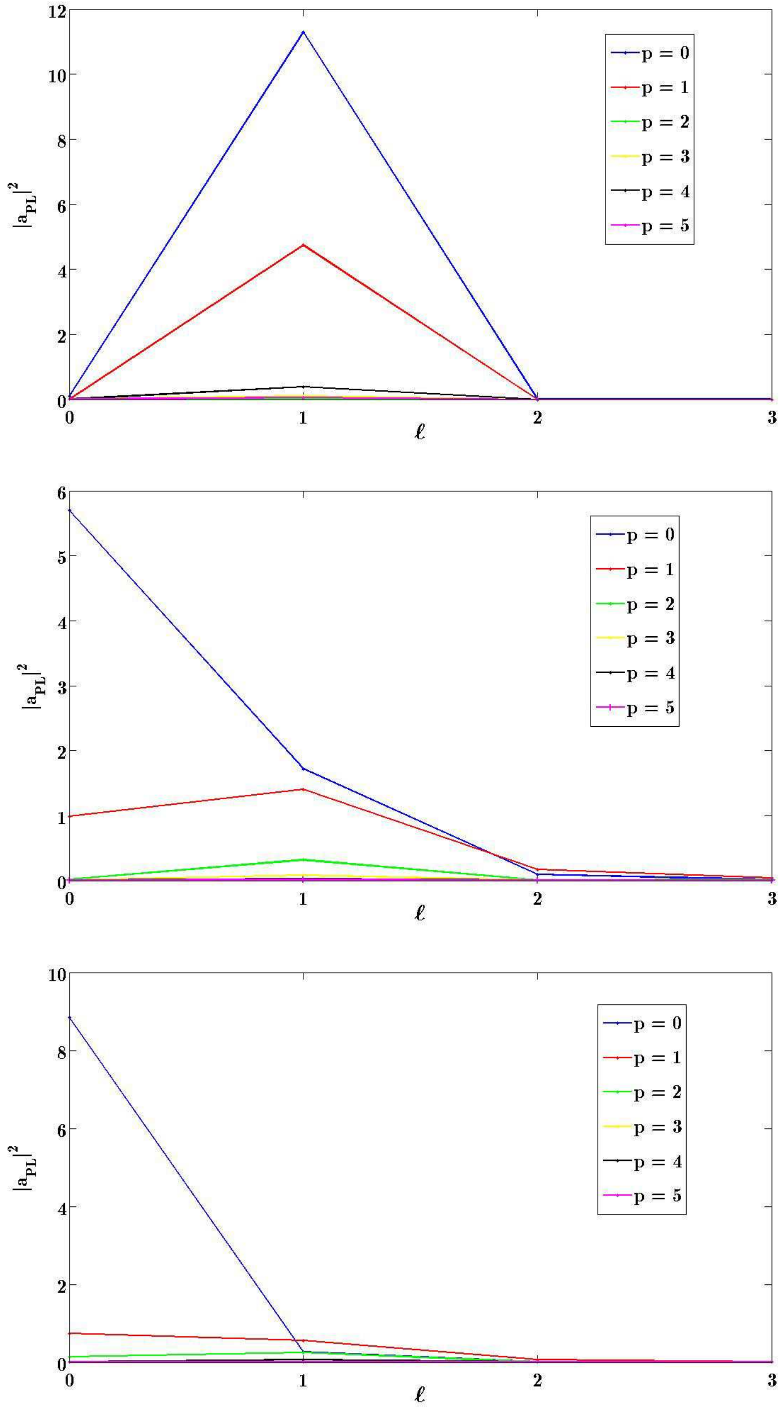

Figure A.1 – Coefficients $|a_{PL}|^2$ of the L-G modes decomposition of an beam with an Airy amplitude distribution intersecting an $\ell = 1$ FH. *Upper panel*: on-axis input beam ($r_0 = 0$). *Central panel*: input beam displaced off-axis by $r_0 = 0.5\,\delta_R$. *Lower panel*: input beam displaced off-axis by $r_0 = \delta_R$.

A.2 Numerical simulations of vortex beams using Fourier optics

The propagation of a beam beyond a PMD can be computed, under paraxial conditions, by using the principle of Fourier optics which well describes the formation of images [50]. In this framework, a PMD is a linear system characterized by a specific transmission function $T(x,y)$ that can modulate both the amplitude and the phase of an incident beam $u(x,y)$. Under Fraunhofer (far-field) diffraction conditions, the field of the output beam $u(x',y')$ is represented by the Fourier transform of the product between the field of the incident beam and $T(x,y)$:

$$u(x',y') = \widehat{u(x,y)\,T(x,y)}\ . \tag{A.5}$$

Here, (x,y) are the coordinates of the PMD plane, while (x',y') are the coordinates of the observation plane placed at a distance $R \gg k(x^2+y^2)/2$ from the PMD.

The principles of Fourier optics can be easily implemented in a numerical algorithm. In fact, the far-field diffraction pattern can be numerically calculated using the 2D Fast Fourier Transform (FFT). The FFT is an efficient algorithm to compute the Discrete Fourier Transform (DFT) of a 1D complex function $f(x)$ which domain is discretized in N elements:

$$\mathrm{DFT}[f(x)] = \frac{1}{N}\sum_{x=0}^{N-1} f(x)\exp\left(-\mathrm{i}\frac{2\pi ux}{N}\right)\ . \tag{A.6}$$

The 2D FFT is obtained by applying the 1D FFT first to one dimension and then to other.

In our numerical simulations, the field of the input beam $u(x,y)$ is translated into a discrete $N\times N$ complex matrix $\mathbf{U}(u,v)$, as well as the transmission function $\mathbf{T}(u,v)$. The far-field amplitude of the produced vortex beam is obtained by evaluating the FFT of the matrix product:

$$\mathbf{U}'(p,q) = \mathrm{FFT}\left[\mathbf{U}(u,v)\mathbf{T}(u,v)\right]\ . \tag{A.7}$$

Therefore, the far-field intensity distribution is simply

$$\mathbf{I}(p,q) = \left|\mathbf{U}'(p,q)\right|^2\ . \tag{A.8}$$

The PMD, either a FH or an SPP, is always considered to be fixed in the (u, v) space, with the corresponding optical singularity placed at the origin of the coordinate system. In the case of an off-axis input beam, the complex matrix $\mathbf{U}(u, v)$ in Eq. A.7 has to be substituted with $\mathbf{U}(u + u_0, v + v_0)$, where (u_0, v_0) are the components of the discrete displacement vector.

All the numerical simulations presented in this Thesis were performed using IDL codes. To avoid artifacts introduced by aliasing, the dimension of the matrices was generally set to 1024×1024 pixels, while the FWHM of the input beams (Gaussian or Airy) was always in the range 10–50 pixels. This choice ensured also a sufficiently high sampling of the final image. In fact, larger beam widths with respect to the FFT window size would produce smaller images in the Fourier space.

A.3 Numerical simulations of an optical vortex coronagraph

The general model of coronagraphs presented in Sect. 5.2 can be efficiently translated into a numerical code. The wave entering the telescope $\psi(x, y)$, the telescope aperture $A(x, y)$, the transmission function of the coronagraphic mask $T(x, y)$ and the Lyot stop aperture $L_S(x, y)$ must be replaced by complex $N \times N$ matrices. In the case of an OVC, the coronagraphic mask is an SPP with transmission function described by Eq. 1.27.

Since the time required to numerically calculate a convolution between two matrices (Eq. 5.3) is substantially larger than that required to calculate an FFT, we decided to calculate the propagation of the wavefront between the planes of the OVC step by step. In order to obtain an high sampling of the coronagraphic images, we used 4096×4096 pixel matrices. In our simulations, performed using IDL codes, we considered a perfectly planar wavefront entering an unobstructed telescope with a circular aperture of diameter $D = 100$ pixels. Therefore, the field of the optical wave just before the SPP is the Fourier transform of the telescope aperture function, i.e. an Airy pattern. Since this amplitude distribution can be evaluated analytically, we decided to perform the numerical simulation of the OVC starting from the SPP plane, to avoid additional aliasing effects introduced by the FFT algorithm. In the framework of the general coronagraphic model, we have thus

$$\psi_B(x,y) = \mathbf{Airy}(x,y)\,\mathbf{T}(x,y)\;, \tag{A.9}$$

where

$$\mathbf{Airy}(x,y) = 2A_0\frac{\mathrm{J}_1(t)}{t}\;. \tag{A.10}$$

Here, A_0 is a normalization factor and $t = 2\pi D\sqrt{x^2+y^2}/N$. In the case of an off-axis star, a lateral translation (x_0, y_0) has to be applied to the complex matrix describing the Airy amplitude distribution.

At the Lyot stop plane, the wavefront is given by

$$\psi_C(u,v) = \mathrm{FFT}\left[\psi_B(x,y)\right]\,\mathbf{L_S}(u,v)\;, \tag{A.11}$$

where the stop function is that of an aperture of diameter D_L. The corresponding matrix is defined by

$$\mathbf{L_S}(u,v) = \begin{cases} 1 & \text{if } 0 < \sqrt{u^2+v^2} < D_L/2 \\ 0 & \text{if } \sqrt{u^2+v^2} > D_L/2 \end{cases}\;. \tag{A.12}$$

The Lyot stop diameter D_L was set to 0.8 times that of the exit pupil. Since the FFT algorithm applies a unitary scaling factor between the (x,y) coordinates of the input matrix and the (u,v) coordinates of the output matrix, the diameter of the exit pupil is equal to that of the telescope aperture. For this reason, we used $D_L = 80$ pixels.

The field at the image plane of the OVC is

$$\psi_D(x',y') = \mathrm{FFT}^{-1}\left[\psi_C(u,v)\right]\;, \tag{A.13}$$

where FFT^{-1} denotes the inverse FFT algorithm. Thus, the image produced at the last plane of the coronagraph can be calculated as

$$\mathbf{I}(x',y') = \left|\psi_D(x',y')\right|^2\;. \tag{A.14}$$

To obtain the coronagraphic images shown in Fig. 5.6, we simply summed the image matrices of the star with unity intensity and the companion with a 10^{-8} intensity peak. This beacause the two sources are assumed to be incoherent.

A.4 Approximate relations for Gaussian optical vortices

Consider a monochromatic Gaussian beam which an intensity distribution

$$I_{\mathrm{G}}(r) \propto \exp\left(-\frac{r^2}{w_0^2}\right) . \tag{A.15}$$

Here, the parameter w_0 roughly represents the width of the beam, as the FWHM of the Gaussian is $2\sqrt{\ln 2}\, w_0$.

The amplitude distribution of an vortex beam generated at the first diffraction order of an $\ell = 1$ FH can be expressed, in paraxial conditions, as a coherent superposition of L-G modes with topological charges $\ell = 1$ and $\ell = 0$ [61]. In a plane (ρ, β) perpendicular to the direction z' of the first diffraction order the amplitude distribution is then

$$u_{\mathrm{out}}(\rho,\beta) = \frac{1}{\sqrt{1+\gamma^2}} \left[u_{00}(\rho,\beta) + \gamma\, u_{10}(\rho,\beta)\right] , \tag{A.16}$$

where γ is a weighting parameter. The topological charge of the output vortex beam is

$$\ell_{\mathrm{out}} = \sum_{\ell} \sum_{p} \ell \left|C_{\ell p}\right|^2 , \tag{A.17}$$

where

$$C_{\ell p} = \int_0^{2\pi} \int_0^{\infty} u_{\mathrm{out}}\, u^*_{\ell p}\, \rho \, \mathrm{d}\rho \, \mathrm{d}\beta , \tag{A.18}$$

and can assume any value in the interval $0 \leq \ell_{\mathrm{out}} \leq 1$. We see that γ is strictly related to ℓ_{out} by the relation

$$\gamma = \sqrt{\frac{\ell_{\mathrm{out}}}{(1-\ell_{\mathrm{out}})}} . \tag{A.19}$$

The value of ℓ_{out}, in turn, depends on the off-axis displacement r of the input beam on the FH plane [98]:

$$\ell_{\mathrm{out}} = \ell_0\, \mathrm{e}^{-r^2/w_0^2} , \tag{A.20}$$

were, in this example, $\ell_0 = 1$.

By substituting in Eq. A.16 the expressions of the L-G modes defined in Eq. 1.7 we can analytically derive an approximate expression of the intensity distribution of the first order OV:

$$I_{\mathrm{out}}(\rho,\beta) \propto \exp\left(-\frac{2\rho^2}{w^2}\right) \left(1 + \frac{2\sqrt{2}\gamma}{w}\rho \cos\beta + \frac{2\gamma^2}{w^2}\rho^2\right) , \tag{A.21}$$

where $w = w_0\sqrt{2\left(1+z'^2/k^2w_0^4\right)}$. The angular coordinate of the phase singularity (the light minimum) must be $\beta_0 = \pi$ and its radial coordinate ρ_0 is found by imposing the condition $I_{\text{out}}(\rho,\pi) = 0$. The condition is fulfilled when

$$\rho = \rho_0 = \frac{w}{\sqrt{2}\gamma}\,, \tag{A.22}$$

which means that the radial position of the phase singularity increases as γ decreases. In other words, the central dark region migrates progressively away from the diffraction axis z', causing the pattern of the OV to lose the axial symmetry. As a result, the two opposite intensity peaks located along the direction $\beta = \pi$ present different values. The ratio between them can be evaluated as:

$$R = \exp\left(-\frac{\sqrt{1+4\gamma^2}}{4\gamma^2}\right)\left(\frac{\sqrt{1+4\gamma^2}-1}{\sqrt{1+4\gamma^2}+1}\right)^2 . \tag{A.23}$$

Publications

Part of the results reported in this Thesis, together with the figures with captions not containing bibliographic references, have been published in or submitted to international journals and/or presented at international conferences:

- F. TAMBURINI, G. UMBRIACO, **G. ANZOLIN**, C. BARBIERI AND A. BIANCHINI. FrogEye, the quantum coronagraphic mask. The photon orbital angular momentum and its applications to astronomy. *Mem. Soc. Astr. It. Suppl.* **9**, 484 (2006)

- F. TAMBURINI, **G. ANZOLIN**, G. UMBRIACO, A. BIANCHINI AND C. BARBIERI. Overcoming the Rayleigh criterion limit with optical vortices. *Phys. Rev. Lett.* **97**, 163903 (2006)

- **G. ANZOLIN**, F. TAMBURINI, A. BIANCHINI, G. UMBRIACO AND C. BARBIERI. Optical vortices with starlight. *Astron. Astrophys.* **488**, 1159 (2008)

- **G. ANZOLIN**, F. TAMBURINI, A. BIANCHINI AND C. BARBIERI. A new method to measure off-axis displacements based on the analysis of the intensity distribution of a vortex beam. Submitted to *Phys. Rev. A* (2009)

- C. BARBIERI, F. TAMBURINI, **G. ANZOLIN**, A. BIANCHINI, E. MARI, A. SPONSELLI, G. UMBRIACO, M. PRASCIOLU, F. ROMANATO AND P. VILLORESI. Light's orbital angular momentum and optical vortices for astronomical coronagraphy from ground and space telescopes. To appear in *Proceedings of the Elba 2008 conference: Future ground based solar system research* (2009)

Bibliography

[1] J. F. Nye and M. V. Berry, *Proc. R. Soc. London A* **336**, 165 (1974).

[2] D. Hull and D. J. Bacon, *Introduction to Dislocations. 4th Edition*, Butterworth-Heinemann, 2001.

[3] J. F. Nye, *Proc. R. Soc. London A* **378**, 219 (1981).

[4] I. V. Basistiy, M. S. Soskin, and M. V. Vasnetsov, *Opt. Commun.* **119**, 604 (1995).

[5] P. Coullet, L. Gil, and F. Rocca, *Opt. Commun.* **73**, 403 (1989).

[6] M. S. Soskin, V. N. Gorshkov, M. V. Vasnetsov, J. T. Malos, and N. R. Heckenberg, *Phys. Rev. A* **56**, 4064 (1997).

[7] M. V. Vasnetsov, I. G. Marienko, and M. S. Soskin, *JETP Lett.* **71**, 130 (2000).

[8] I. D. Maleev and G. A. Swartzlander, *J. Opt. Soc. Am. B* **20**, 1169 (2003).

[9] I. V. Basistiy, V. Y. Bazhenov, M. S. Soskin, and M. V. Vasnetsov, *Opt. Commun.* **103**, 422 (1993).

[10] L. Allen, M. W. Beijersbergen, R. J. C. Spreeuw, and J. P. Woerdman, *Phys. Rev. A* **45**, 8185 (1992).

[11] M. J. Padgett and L. Allen, *Opt. Commun.* **121**, 36 (1995).

[12] M. Abramowitz and I. A. Stegun, *Handbook of mathematical functions with formulas, graphs, and mathematical tables*, Dover Books on Advanced Mathematics, New York, 1964.

[13] S. M. BARNETT and L. ALLEN, *Opt. Commun.* **110**, 670 (1994).

[14] J. D. JACKSON, *Classical Electrodynamics. 3rd Edition,* John Wiley & Sons Inc., New York, 1998.

[15] L. ALLEN and M. J. PADGETT, *Opt. Commun.* **184**, 67 (2000).

[16] A. Y. BEKSHAEV, M. S. SOSKIN, and M. V. VASNETSOV, *Ukr. J. Phys. (English translation: arXiv:0801.2309)* **2**, 73 (2005).

[17] A. MAIR, A. VAZIRI, G. WEIHS, and A. ZEILINGER, *Nature* **412**, 313 (2001).

[18] I. BIALYNICKI-BIRULA and Z. BIALYNICKA-BIRULA, *Opt. Commun.* **264**, 342 (2006).

[19] G. F. CALVO, A. PICÓN, and E. BAGAN, *Phys. Rev. A* **73**, 013805 (2006).

[20] E. MAJORANA, *Nuovo Cimento* **9**, 335 (1932).

[21] F. TAMBURINI and D. VICINO, *Phys. Rev. A* **78**, 052116 (2008).

[22] M. V. BERRY, *J. Phys. A* **11**, 27 (1978).

[23] T. ACKEMANN, E. KRIEGE, and W. LANGE, *Opt. Commun.* **115**, 339 (1995).

[24] G. A. SWARTZLANDER, JR. and C. T. LAW, *Phys. Rev. Lett.* **69**, 2503 (1992).

[25] F. T. ARECCHI, G. GIACOMELLI, P. L. RAMAZZA, and S. RESIDORI, *Phys. Rev. Lett.* **67**, 3749 (1991).

[26] L. V. KREMINSKAYA, M. S. SOSKIN, and A. I. KHIZHNYAK, *Opt. Commun.* **145**, 377 (1998).

[27] N. B. BARANOVA, B. Y. ZEL'DOVICH, A. V. MAMAEV, N. F. PILIPETSKIĬ, and V. V. SHKUKOV, *J. Exp. Theor. Phys. Lett.* **33**, 195 (1981).

[28] K. STALIUNAS, A. BERZANSKIS, and V. JARUTIS, *Opt. Commun.* **120**, 23 (1995).

[29] K. O'HOLLERAN, M. J. PADGETT, and M. R. DENNIS, *Opt. Expr.* **14**, 3039 (2006).

[30] C. Tamm and C. O. Weiss, *J. Opt. Soc. Am. B* **7**, 1034 (1990).

[31] M. Brambilla, F. Battipede, L. A. Lugiato, V. Penna, F. Prati, C. Tamm, and C. O. Weiss, *Phys. Rev. A* **43**, 5090 (1991).

[32] G. Indebetouw and D. R. Korwan, *J. Mod. Opt.* **41**, 941 (1994).

[33] G. L. Lippi, T. Ackemann, L. M. Hoffer, A. Gahl, and W. Lange, *Phys. Rev. A* **48**, 4043 (1993).

[34] N. R. Heckenberg, M. Vaupel, J. T. Malos, and C. O. Weiss, *Phys. Rev. A* **54**, 2369 (1996).

[35] M. Lax, W. H. Louisell, and W. B. McKnight, *Phys. Rev. A* **11**, 1365 (1975).

[36] F. Pampaloni and J. Enderlein, *arXiv:physics/0410021* (2004).

[37] A. G. White, C. P. Smith, N. R. Heckenberg, H. Rubinsztein-Dunlop, R. McDuff, C. O. Weiss, and C. Tamm, *J. Mod. Opt.* **38**, 2531 (1991).

[38] G. Nienhuis and L. Allen, *Phys. Rev. A* **48**, 656 (1993).

[39] J. Durnin, *J. Opt. Soc. Am. A* **4**, 651 (1987).

[40] F. Gori, G. Guattari, and C. Padovani, *Opt. Commun.* **64**, 491 (1987).

[41] M. W. Beijersbergen, L. Allen, H. E. L. O. van der Veen, and J. P. Woerdman, *Opt. Commun.* **96**, 123 (1993).

[42] S. A. Kennedy, M. J. Szabo, H. Teslow, J. Z. Porterfield, and E. R. Abraham, *Phys. Rev. A* **66**, 043801 (2002).

[43] D. Gabor, *Nature* **161**, 777 (1948).

[44] E. N. Leith and J. Upatnieks, *J. Opt. Soc. Am.* **52**, 1123 (1962).

[45] H. R. Brown and A. W. Lohmann, *IBM J. Res. Develop.* **13**, 160 (1969).

[46] V. Y. Bazhenov, M. V. Vasnetsov, and M. S. Soskin, *J. Exp. Theor. Phys. Lett.* **52**, 429 (1990).

[47] N. R. HECKENBERG, R. MCDUFF, C. P. SMITH, and A. G. WHITE, *Opt. Lett.* **17**, 221 (1992).

[48] R. HECKENBERG, N. R. MCDUFF, C. P. SMITH, H. RUBINSZTEIN-DUNLOP, and M. J. WEGENER, *Opt. Quantum Electron.* **24**, S951 (1992).

[49] J. ARLT, K. DHOLAKIA, L. ALLEN, and M. J. PADGETT, *J. Mod. Opt.* **45**, 1231 (1998).

[50] E. HECHT, *Optics. 4th Edition*, Addison-Wesley Publishing Company, Reading, MA, 2002.

[51] G. F. BRAND, *Am. J. Phys.* **67**, 55 (1999).

[52] A. Y. BEKSHAEV and A. I. KARAMOCH, *Opt. Commun.* **281**, 1366 (2008).

[53] Z. S. SACKS, D. ROZAS, and G. A. SWARTZLANDER, JR., *J. Opt. Soc. Am. B* **15**, 2226 (1998).

[54] M. W. BEIJERSBERGEN, R. P. C. COERWINKEL, M. KRISTENSEN, and J. P. WOERDMAN, *Opt. Commun.* **112**, 321 (1994).

[55] S. S. R. OEMRAWSINGH, J. A. W. VAN HOUWELINGEN, E. R. ELIEL, J. P. WOERDMAN, E. J. K. VERSTEGEN, J. G. KLOOSTERBOER, and G. W. 'T HOOFT, *Appl. Opt.* **43**, 688 (2004).

[56] G. A. TURNBULL, D. A. ROBERTSON, G. M. SMITH, L. ALLEN, and M. J. PADGETT, *Opt. Commun.* **127**, 183 (1996).

[57] A. G. PEELE, P. J. MCMAHON, D. PATERSON, C. Q. TRAN, A. P. MANCUSO, K. A. NUGENT, J. P. HAYES, E. HARVEY, B. LAI, and I. MCNULTY, *Opt. Lett.* **27**, 1752 (2002).

[58] M. BORN and E. WOLF, *Principles of optics. Electromagnetic theory of propagation, interference and diffraction of light. 6th corrected edition*, Pergamon Press, Oxford, UK, 1980.

[59] D. ROZAS, C. T. LAW, and G. A. SWARTZLANDER, JR., *J. Opt. Soc. Am. B* **14**, 3054 (1997).

[60] G. A. SWARTZLANDER, JR., *Opt. Lett.* **26**, 497 (2001).

[61] A. VAZIRI, G. WEIHS, and A. ZEILINGER, *J. Opt. B* **4**, 47 (2002).

[62] G. MOLINA-TERRIZA, J. P. TORRES, and L. TORNER, *Nature Phys.* **3**, 305 (2007).

[63] H. HE, M. E. J. FRIESE, N. R. HECKENBERG, and H. RUBINSZTEIN-DUNLOP, *Phys. Rev. Lett.* **75**, 826 (1995).

[64] M. E. J. FRIESE, J. ENGER, H. RUBINSZTEIN-DUNLOP, and N. R. HECKENBERG, *Phys. Rev. A* **54**, 1593 (1996).

[65] K. T. GAHAGAN and G. A. SWARTZLANDER, JR., *Opt. Lett.* **21**, 827 (1996).

[66] D. G. GRIER, *Nature* **424**, 810 (2003).

[67] G. GIBSON, J. COURTIAL, M. J. PADGETT, M. VASNETSOV, V. PAS'KO, S. M. BARNETT, and S. FRANKE-ARNOLD, *Opt. Commun.* **12**, 5448 (2004).

[68] L. TORNER, J. P. TORRES, and S. CARRASCO, *Opt. Commun.* **13**, 873 (2005).

[69] G. MOLINA-TERRIZA, L. REBANE, J. P. TORRES, L. TORNER, and S. CARRASCO, *J. Europ. Opt. Soc.* **2** (2007).

[70] J. COURTIAL, K. DHOLAKIA, L. ALLEN, and M. J. PADGETT, *Opt. Commun.* **144**, 210 (1997).

[71] L. MANDEL and E. WOLF, *Optical coherence and quantum optics*, Cambridge University Press, Cambridge, 1995.

[72] F. GORI, M. SANTARSIERO, R. BORGHI, and S. VICALVI, *J. Mod. Opt.* **45**, 539 (1998).

[73] S. A. PONOMARENKO, *J. Opt. Soc. Am. A* **18**, 150 (2001).

[74] G. GBUR and T. D. VISSER, *Opt. Commun.* **222**, 117 (2003).

[75] D. M. PALACIOS, I. D. MALEEV, A. S. MARATHAY, and G. A. SWARTZLANDER, JR., *Phys. Rev. Lett.* **92**, 143905 (2004).

[76] D. DRAVINS, C. BARBIERI, R. A. E. FOSBURY, G. NALETTO, R. NILSSON, T. OCCHIPINTI, F. TAMBURINI, H. UTHAS, and L. ZAMPIERI, QuantEYE: The Quantum Optics Instrument for OWL, in *Instrumentation for Extremely Large Telescopes*, edited by T. HERBST, 2005.

[77] C. BARBIERI, D. DRAVINS, T. OCCHIPINTI, F. TAMBURINI, G. NALETTO, V. D. DEPPO, S. FORNASIER, M. D'ONOFRIO, R. A. E. FOSBURY, R. NILSSON, and H. UTHAS, *J. Mod. Opt.* **54**, 191 (2007).

[78] M. HARWIT, *Astrophys. J.* **597**, 1266 (2003).

[79] G. C. G. BERKHOUT and M. W. BEIJERSBERGEN, *Phys. Rev. Lett.* **101**, 100801 (2008).

[80] N. M. ELIAS II, *Astron. Astrophys.* **492**, 883 (2008).

[81] C. PATERSON, *Phys. Rev. Lett.* **94**, 153901 (2005).

[82] B. THIDÉ, H. THEN, J. SJÖHOLM, K. PALMER, J. BERGMAN, T. D. CAROZZI, Y. N. ISTOMIN, N. H. IBRAGIMOV, and R. KHAMITOVA, *Phys. Rev. Lett.* **99**, 087701 (2007).

[83] J. T. MENDONÇA, B. THIDÉ, J. E. S. BERGMAN, S. M. MOHAMMADI, B. ELIASSON, W. BAAN, and H. THEN, *arXiv:0804.3221* (2008).

[84] J. T. MENDONÇA and B. THIDÉ, *Europhys. Lett.* **84**, 41001 (2008).

[85] STRUTT, J. W. (LORD RAYLEIGH), *Philos. Magazine* **10**, 116 (1880).

[86] A. DANJON and A. COUDER, *Lunettes et Teléscopes*, Éditions de la Revue d'Optique Théorique et Instrumentale, Paris, 1935.

[87] K. G. PUSCHMANN and F. KNEER, *Astron. Astrophys.* **436**, 373 (2005).

[88] N. I. ZHELUDEV, *Nature Mater.* **7**, 420 (2008).

[89] Z. JACOB, L. V. ALEKSEYEV, and E. NARIMANOV, *Opt. Expr.* **14**, 8247 (2006).

[90] X. ZHANG and Z. LIU, *Nature Mater.* **7**, 435 (2008).

[91] A. Ranfagni, D. Mugnai, and R. Ruggeri, *J. Appl. Phys.* **95**, 2217 (2004).

[92] Y. Ben-Aryeh, *Phys. Lett. A* **328**, 306 (2004).

[93] D. Palacios, *An Optical Vortex Coherence Filter,* PhD thesis, Worchester Polytechnic Institute, 2004.

[94] G. Lenz, *Opt. Commun.* **123**, 423 (1996).

[95] L. E. Helseth, *Opt. Commun.* **229**, 85 (2004).

[96] M. V. Vasnetsov, V. A. Pas'ko, and M. S. Soskin, *New J. Phys.* **7**, 46 (2005).

[97] R. Zambrini and S. M. Barnett, *Phys. Rev. Lett.* **96**, 113901 (2006).

[98] S. S. R. Oemrawsingh, E. R. Eliel, G. Nienhuis, and J. P. Woerdman, *J. Opt. Soc. Am. A* **21**, 2089 (2004).

[99] D. Mawet, P. Riaud, O. Absil, and J. Surdej, *Astrophys. J.* **633**, 1191 (2005).

[100] C. Jenkins, *Mon. Not. R. Astron. Soc.* **384**, 515 (2008).

[101] I. R. King, *Pubbl. Astron. Soc. Pacific* **83**, 199 (1971).

[102] L. C. Andrews, *Field Guide to Atmospheric Optics,* SPIE Press, Bellingham, Washington, USA, 2004.

[103] N. M. Law, S. T. Hodgkin, and C. D. Mackay, *Mon. Not. R. Astron. Soc.* **368**, 1917 (2006).

[104] N. M. Law, C. D. Mackay, and J. E. Baldwin, *Astron. Astrophys.* **446**, 739 (2006).

[105] D. L. Fried, *J. Opt. Soc. Am.* **68**, 1651 (1978).

[106] V. Shvedov, W. Krolikowski, A. Volyar, D. N. Neshev, A. S. Desyatnikov, and Y. S. Kivshar, *Opt. Expr.* **13**, 7393 (2005).

[107] J. Leach and M. Padgett, *New J. Phys.* **5**, 154 (2003).

[108] H. A. McAlister, W. I. Hartkopf, J. R. Sowell, E. G. Dombrowski, and O. G. Franz, *Astron. J.* **97**, 510 (1989).

[109] J. L. Halbwachs, *Astron. Astrophys. Suppl.* **44**, 47 (1981).

[110] M. V. Berry, *J. Opt. A* **6**, 259 (2004).

[111] M. V. Vasnetsov, J. P. Torres, D. V. Petrov, and L. Torner, *Opt. Lett.* **28**, 2285 (2003).

[112] A. Y. Bekshaev and A. I. Karamoch, *Opt. Commun.* **281**, 3597 (2008).

[113] J. E. Curtis and D. G. Grier, *Phys. Rev. Lett.* **90**, 133901 (2003).

[114] I. V. Basistiy, V. A. Pas'ko, V. V. Slyusar, M. S. Soskin, and M. V. Vasnetsov, *J. Opt. A* **6**, 166 (2004).

[115] W. Wang, T. Yokozeki, R. Ishijima, M. Takeda, and S. G. Hanson, *Opt. Expr.* **14**, 10195 (2006).

[116] A. Jesacher, A. Schwaighofer, S. Fürhapter, C. Maurer, S. Bernet, and M. Ritsch-Marte, *Opt. Expr.* **15**, 5801 (2007).

[117] Y.-D. Liu, C. Gao, X. Qi, and H. Weber, *Opt. Expr.* **16**, 7091 (2008).

[118] T. Watanabe, M. Fujii, Y. Watanabe, N. Toyama, and Y. Iketaki, *Rev. Sci. Instr.* **75**, 5131 (2004).

[119] K. Sueda, G. Miyaji, N. Miyanaga, and M. Nakatsuka, *Opt. Expr.* **12**, 3548 (2004).

[120] S. B. Howell, *Handbook of CCD astronomy. 2nd Edition*, Cambridge observing handbooks for research astronomers, Vol. 5. Cambridge University Press, Cambridge, UK, 2006.

[121] B. Lyot, *Mon. Not. R. Astron. Soc.* **99**, 580 (1939).

[122] A. Quirrenbach, *arXiv:astro-ph/0502254* (2005).

[123] G. ROUSSET, F. LACOMBE, P. PUGET, N. N. HUBIN, E. GENDRON, T. FUSCO, R. ARSENAULT, J. CHARTON, P. FEAUTRIER, P. GIGAN, P. Y. KERN, A.-M. LAGRANGE, P.-Y. MADEC, D. MOUILLET, D. RABAUD, P. RABOU, E. STADLER, and G. ZINS, NAOS, the first AO system of the VLT: on-sky performance, in *SPIE Conference Series*, edited by P. L. WIZINOWICH and D. BONACCINI, volume 4839, p. 140, 2003.

[124] R. NEUHÄUSER, E. W. GUENTHER, G. WUCHTERL, M. MUGRAUER, A. BEDALOV, and P. H. HAUSCHILDT, *Astron. Astrophys.* **435**, L13 (2005).

[125] G. CHAUVIN, A.-M. LAGRANGE, C. DUMAS, B. ZUCKERMAN, D. MOUILLET, I. SONG, J.-L. BEUZIT, and P. LOWRANCE, *Astron. Astrophys.* **425**, L29 (2004).

[126] Y. ITOH, M. HAYASHI, M. TAMURA, T. TSUJI, Y. OASA, M. FUKAGAWA, S. S. HAYASHI, T. NAOI, M. ISHII, S. MAYAMA, J.-I. MORINO, T. YAMASHITA, T.-S. PYO, T. NISHIKAWA, T. USUDA, K. MURAKAWA, H. SUTO, S. OYA, N. TAKATO, H. ANDO, S. M. MIYAMA, N. KOBAYASHI, and N. KAIFU, *Astrophys. J.* **620**, 984 (2005).

[127] K. L. LUHMAN, J. C. WILSON, W. BRANDNER, M. F. SKRUTSKIE, M. J. NELSON, J. D. SMITH, D. E. PETERSON, M. C. CUSHING, and E. YOUNG, *Astrophys. J.* **649**, 894 (2006).

[128] D. LAFRENIÈRE, R. JAYAWARDHANA, and M. H. VAN KERKWIJK, *Astrophys. J.* **689**, L153 (2008).

[129] C. MAROIS, B. MACINTOSH, T. BARMAN, B. ZUCKERMAN, I. SONG, J. PATIENCE, D. LAFRENIERE, and R. DOYON, *Science* **322**, 1348 (2008).

[130] O. GUYON, E. A. PLUZHNIK, M. J. KUCHNER, B. COLLINS, and S. T. RIDGWAY, *Astrophys. J. Suppl. Series* **167**, 81 (2006).

[131] A. FERRARI, R. SOUMMER, and C. AIME, *C. R. Physique* **8**, 277 (2007).

[132] R. SOUMMER, *Astrophys. J.* **618**, L161 (2005).

[133] F. RODDIER and C. RODDIER, *Pubbl. Astron. Soc. Pacific* **109**, 815 (1997).

[134] D. ROUAN, P. RIAUD, A. BOCCALETTI, Y. CLÉNET, and A. LABEYRIE, *Pubbl. Astron. Soc. Pacific* **112**, 1479 (2000).

[135] L. ABE, F. VAKILI, and A. BOCCALETTI, *Astron. Astrophys.* **374**, 1161 (2001).

[136] G. FOO, D. M. PALACIOS, and G. A. SWARTZLANDER, JR., *Opt. Lett.* **30**, 3308 (2005).

[137] D. M. PALACIOS and G. A. SWARTZLANDER, JR., The high-contrast performance of an optical vortex coronagraph, in *SPIE Conference Series*, volume 6288, p. 62880B, 2006.

[138] D. M. PALACIOS and S. L. HUNYADI, *Opt. Lett.* **31**, 2981 (2006).

[139] G. A. SWARTZLANDER, JR., *Opt. Lett.* **31**, 2042 (2006).

[140] C.-S. GUO, D.-M. XUE, Y.-J. HAN, and J. DING, *Opt. Commun.* **268**, 235 (2006).

[141] B. JACK, M. J. PADGETT, and S. FRANKE-ARNOLD, *New J. Phys.* **10**, 103013 (2008).

[142] J. H. LEE, G. FOO, E. G. JOHNSON, and G. A. SWARTZLANDER, JR., *Phys. Rev. Lett.* **97**, 053901 (2006).

[143] G. A. SWARTZLANDER, JR., E. L. FORD, R. S. ABDUL-MALIK, L. M. CLOSE, M. A. PETERS, D. M. PALACIOS, and D. W. WILSON, *Opt. Expr.* **16**, 10200 (2008).

[144] A. VAZIRI, *Experimente mit Singulären Quantenzuständen Höherdimensional Verschränkter Photonen*, PhD thesis, Institut für Experimentalphysik der Universität Wien, 2003.